NORTHWESTERN UNIVERSITY

Nanoscale Experimental Methods Applied to Atomically-Thin Resonators and Single-Cell Analysis

A DISSERTATION

SUBMITTED TO THE GRADUATE SCHOOL
IN PARTIAL FULFILLMENT OF THE REQUIREMENTS

for the degree

DOCTOR OF PHILOSOPHY

Field of Theoretical and Applied Mechanics

By

Samba Shiva Prasad Nathamgari

EVANSTON, ILLINOIS

June 2019

Abstract

Nanoscale Experimental Methods Applied to Atomically-Thin Resonators and Single-Cell Analysis

Samba Shiva Prasad Nathamgari

Nanoelectromechanical (NEMS) systems fabricated using atomically-thin materials have low mass and high stiffness and are thus ideal candidates for force and mass sensing applications. Transition metal dichalcogenides (TMDCs) offer certain unique properties in their few-layered form – such as piezoelectricity and a direct band gap in some case – and are an interesting alternative to graphene based NEMS. Among the demonstrated methods for displacement transduction in NEMS, cavity-interferometry provides exquisite displacement sensitivity. Typically, interferometric measurements are complemented with Raman spectroscopy to characterize the number of layers in 2D materials, and the measurements necessitate high vacuum conditions to eliminate viscous damping. In this thesis, we report an experimental setup that facilitates both Raman spectroscopy and interferometric measurements on atomically-thin materials. Specifically, we report measurements on few-layered Tungsten Disulfide (WS_2) resonators in high vacuum (less than

10^{-5} Torr) conditions. The lowest resolvable force in NEMS is limited by ambient thermal noise, and as a result, the resonators (which form the sensing element) are either operated at cryogenic temperatures or coupled to a high-finesse optical or microwave cavity to reach sub aN $Hz^{-1/2}$ sensitivity. In the present thesis, we show that operating a monolayer WS_2 nanoresonator in the strongly nonlinear regime can lead to comparable force sensitivities at room temperature. Cavity-interferometry was used to transduce the nonlinear response of the nanoresonator, which was characterized by multiple pairs of 1:1 internal resonance. Some of the modes exhibited exotic line-shapes due to the appearance of Hopf bifurcations, where the bifurcation frequency varied linearly with the driving force and forms the basis of the advanced sensing modality. The modality is less sensitive to the measurement bandwidth, limited only by the intrinsic frequency fluctuations, and therefore, advantageous in the detection of weak incoherent forces.

Localized electroporation has evolved as an effective technology for the delivery of foreign molecules into cells while preserving their viability. Consequently, this technique has potential applications in sampling the contents of live cells and the temporal assessment of cellular states at the single-cell level. Although there have been numerous experimental reports on localized electroporation-based delivery, a lack of a mechanistic understanding of the process hinders its implementation in sampling. In the present thesis, we develop a multiphysics model that predicts the transport of molecules into and out of the cell during localized electroporation. Based on the model predictions, we optimize experimental parameters such as buffer conditions, electric field strength, cell confluency, and density of nanochannels in the substrate for successful delivery and sampling via localized electroporation. We also identify that cell membrane tension plays a crucial role in enhancing both

the amount and the uniformity of molecular transport, particularly for macromolecules. We qualitatively validate the model predictions on a localized electroporation platform by delivering large molecules (bovine serum albumin and mCherry-encoding plasmid) and by sampling an exogeneous protein (tdTomato) in an engineered cell line. The insights from the model developed here form an important advancement towards the goal of single-cell sampling using localized electroporation.

Acknowledgements

None knoweth whence creation has arisen, And whether he has or has not produced it, He who surveys it in the highest heaven, He only knows or haply he may know not

Nasadiya Sukta, Rig Veda

The current thesis, although credited to a single author, has been possible due to generous support from many people and institutions. My attempt here is to provide a chronological account of the people and factors instrumental in accomplishing the present work. The present thesis is a humble and dim reflection of the undying spirit of భారత్ (Bharat, present day India), where the pursuit of knowledge is regarded as the highest goal possible for mankind. I am eternally indebted to my parents Shri Rajagopal Nathamgari and Shrimati Mehera Nathamgari for their innumerable sacrifices. I am especially thankful to my alma mater, the Indian Institute of Technology (Guwahati) for the high-quality of baccalaureate education, and in particular, to faculty members Dr. Natesan Srinivasan, Dr. Arbind Kumar Singh for their excellent mentorship during my formative years.

At Northwestern, I am thankful to my advisor, Prof. Horacio Dante Espinosa for providing me with great academic freedom without which, an inter-disciplinary thesis such as the present one would not have been possible. Having been involved in proposal writing for a good part of my graduate education, I have come to be more appreciative of his efforts towards securing great resources for our lab that facilitate the high quality

of research. I am also thankful to my committee members Professors Oluwaseyi Balogun, Sridhar Krishnaswamy and Cheng Sun for their willingness to help me at all times. Prof. Lincoln James Lauhon provided valuable comments on two manuscripts that form the core of Chapters 2, 3. The current work was funded mainly by the National Science Foundation, the Army Research Office and the National Institutes of Health.

My initiation into academic research in the Micro and Nano Mechanics Lab at Northwestern was a pleasant experience, largely due to the excellent guidance of two people - Dr. Allison Beese and Dr. Wonmo Kang. I am also thankful to other wonderful post-docs in the lab for training me on certain critical experimental steps - Dr. Juan Pablo Giraldo-Vela for primary cell culture, Dr. Changjin Huang for immunostaining and Dr. Ruiguo Yang for electroportion protocols. Special thanks are due to Dr. Chian-Yu Peng and Tammy Lretta McGuire from the Kessler Lab for providing primary cells at all times of need, and to Siyan Dong for his tireless efforts in fabricating samples for the 2D materials project.

I have had the pleasure of working with several bright colleagues in our lab - Siyan Dong, Zhaowen Lin, Prithvijit Mukherjee, Hoang T. Nguyen, Nibir Pathak (Baba), Cesar Patino (Stubby), Alireza Zaheri, Xu Zhang - and I will miss discussing both research and trifles with them. I wish the new lab members Dr. Meisam Asgari, Dr. Lior Medina and Nicolas Alderete the very best. ME Staff members Pat Dyess, Sinta Kulanda, Rick Marzec and Vanessa Smith deserve a special mention for their assistance with adhering to TGS requirements, purchase orders and IT support.

I have made some great friends in the lab - Drs Rajaprakash Ramachandramoorthy, Michael R. Roenbeck and Rafael Soler-Crespo, who made the PhD experience all the

more enjoyable. Lastly, none of this would have been possible without the unconditional support of my wife Abhigna Pebbati.

Sincerely,

సాంబ శివ (పసాద్ నాధంగారి

Samba Shiva Prasad, Nathamgari

Table of Contents

List of Tables

List of Figures

CHAPTER 1

Introduction

O Rāma, even a young boy's words are to be accepted if they are words of wisdom; else, reject it like straw even if uttered by Brāhma the creator

Yoga Vāsiṣtha

1.1. Nanoelectromechanical Systems using 2D Materials

Due to their small footprint, nanoelectromechanical systems (NEMS) have been employed in the detection of ultra-low quantities of mass, force and charge [1]. NEMS fabricated using 2D materials - such as graphene, monolayer molybdenum disulfide (MoS_2) or black phosphorus - constitute the thinnest possible NEMS and possess several advantages over their micro-machined Si counterparts. Despite their small thickness, they possess a remarkably broad dynamic range (50-100 dB, depending on the material and thickness, [2]) and resonance frequencies in the RF region. Furthermore, the frequencies are widely tunable using capacitive or optical means [3]. The atomic scale thickness in these resonators is conducive towards investigating nonlinear mode-coupling [4, 5].

Since its isolation in 2004 by Nobel laureates Geim and Novoselov [6], graphene has been intensively studied for its outstanding optical, electrical, and mechanical properties [7, 8]. However, a major caveat with graphene is the absence of an electronic bandgap for transistor applications [9]. Monolayer transition metal dichalcogenides (TMDCs) which have the general formula MX_2 (where M = Mo or W, X = S, Se or Te), offer certain

unique advantages over graphene such as a sizeable bandgap and intrinsic piezoelectricity [9, 10]. Molecular dynamics calculations predict higher Q-factors in TMDCs due to reduced phonon-phonon scattering losses [11] and hence, they are better suited to NEMS applications. A common method of fabricating 2D NEMS is to exfoliate a bulk-TMDC crystal using the scotch-tape method onto a Si substrate with pre-patterned holes or trenches. Because the exfoliation process results in flakes of different thicknesses, a prior characterization step is required before measuring the resonance spectra. Raman spectroscopy is a high-throughput, non-contact method to characterize the layer number in some few-layered TMDC flakes and to distinguish monolayers in most TMDCs (see Table 2.2). However, Raman characterization in ambient conditions may lead to sample degradation, which is particularly problematic for the selenides and tellurides in TMDC family. To address this issue, an experimental setup for combined Raman spectroscopy and cavity interferometry in high-vacuum has been developed in this thesis (see Chapter 2). Most device applications involving 2D NEMS make use of their behavior in the linear regime; in Chapter 3, a force sensor that utilizes the strongly nonlinear behavior in monolayer tungsten disulfide (WS_2) is demonstrated. The results show that a force sensitivity in the atto-Newton range should be achievable at room temperature in 2D NEMS that operate in the nonlinear regime.

1.2. Single-Cell Heterogeneity and Stem-Cell Technology

Cell heterogeneity can arise from the random nature of gene, protein and metabolite expression or the variation in cell cycles [12–14]. Such heterogeneous behavior is eclipsed in traditional bulk experiments and warrants analysis at the single-cell level. Single-cell

analysis could be useful or even necessary in some cases, for instance, in the isolation of rare cancer cells. The averaged behavior from an ensemble could be misleading. To illustrate, using an integrated microfluidic bioprocessing chip for gene expression analysis, it was shown that siRNA knockdown of GAPDH in Jurkat cells led to two distinct groups. One had a complete knockdown (0%) of the gene while another showed only a partial knockdown (50%). A bulk experiment on 50 cells yielded an average value of 21% knockdown, a value which is close to neither of the two cell groups [15]. As a second example, TNF-α, which is a biomarker for immune cell activation, can be secreted by many stimulated cell types. However, in a given population, only 10% would produce significant quantities of the protein [16]. Cell heterogeneity is also prevalent in stem-cell assays. Floating spheroid clusters of stem-cells tend to produce lineage restricted progenitors in the sphere's interior [17]. Analysis at the single-cell level could yield potential insights into the signaling pathways for self-renewal and differentiation in these assays. The main target in cancer therapy might be cancer stem-cells which form a small fraction of the population but could be the main drivers for tumor re-growth after treatment. Finally, network models of disease onset and progression are arising from the use of a systems biology approach, for which directed proteomic analysis at the single-cell level is a prerequisite [18].

The ability to reprogram human somatic cells into induced pluripotent stem-cells (iPSCs) through the expression of certain transcription factors holds great promise in revolutionizing both basic research and clinical practice [19–21]. iPSCs offer hitherto unavailable, patient-specific cells which can serve as *in vitro* platforms for disease modeling and pathway discovery, drug screening, toxicity studies and cell therapy. The technology

to derive different cell types *in vitro* and monitor their response to potential drugs is unprecedented and paves the way for personalized prescription in medicine. In a study by the Tufts Center for the Study of Drug Development(CSDD), the cost towards the development of a new prescription drug is estimated at $2.5 billion and typically takes more than 10 years. The study also concluded that another $312 million is spent on post-approval development for a total life-cycle cost of $2.9 billion. In addition, a drug that works well for some could potentially produce adverse effects in a side population. For instance, Vioxx, a non-steroidal anti-inflammatory drug (NSAID) that reduces pain, inflammation and swelling was a boon to people suffering from arthritis. However, it also increased the risk of heart attack in others and had to be withdrawn by Merck in 2004 (http://www.drugs.com/vioxx.html). iPSC based in-vitro test platforms can speed up and dramatically reduce the costs associated with drug development. Furthermore, patient specific iPSCs can be used as test beds for early diagnosis of dementias like Alzheimer's. In the United States, Alzheimer's disease is the sixth leading cause of death. The estimated cost of treatment towards Alzheimer's and other dementias in 2015 is $226 billion and is projected to rise to $1.1 trillion in 2050 (http://www.alz.org/facts/.). Early stage detection and stem-cell-therapy could pave the way towards effective treatment of such disorders. However, in order to realize these potential applications, a comprehensive understanding of the molecular basis of pluripotency, cellular reprogramming and differentiation is lacking [20].

Enabled by advances in microfluidics and next generation sequencing techniques, single-cell "omics" research is redefining metrics for cell state and behavior. These advances have led to a better understanding of tumor heterogeneity, the identification of

rare cells and stem-cell lineages. However, with the exception of secreted proteins and surface markers, single-cell analysis (SCA) invariably requires cell lysis, which provides only a snapshot of the cell's activity. Localized electroporation – the process of transient permeabilization of the plasma membrane through voltage pulses – allows the retrieval of a fraction of the cytosol without killing the cell, while retaining subsequent cell viability. The extracted proteins, mRNA and enzymes can be assayed using methods such as western-blotting, RT-PCR and mass spectrometry. Thus, it has the potential to transform single-cell analysis by providing a window into the behavior of the *same cell* over a period of time. However, two challenges remain before localized electroporation can be applied to single-cell analysis. The first challenge is technological in nature and is related to the fact that the volumes sampled in localized electroporation are very small (less than 1%). This requires the development of high precision microfluidic systems coupled to ultra-sensitive assays that can handle, transport and detect sub-cellular amounts of analytes in picoliter volumes, without incurring substantial losses. The second challenge is the lack of a mechanistic understanding of the process of localized electroporation and molecular transport out of the cell during sampling. The current thesis aims to address the second challenge in Chapter 4.

The thesis is organized as follows: In Chapter 2, an experimental setup for combined Raman spectroscopy and cavity interferometry measurements is discussed in detail. As proof of concept, measurements on WS_2 resonators of varying thicknesses are presented. In Chapter 3, a force sensor that is based on a monolayer WS_2 nanoresonator in the strongly nonlinear regime is discussed. The force sensing modality is in stark contrast to existing approaches that cool the resonator to cryogenic temperatures to minimize thermal forces.

Lastly, in Chapter 4, a multi-physics model for localized electroporation is developed and qualitatively validated with experiments. The predictions from the model point towards potential regimes that may be advantageous towards reaching the goal of *nondestructive*, single-cell analysis.

CHAPTER 2

Transition Metal Dichalcogenide Resonators: Cavity Interferometry Setup

That which cannot be expressed by speech, but by which speech is expressed-That alone know as Brahman, and not that which people here worship

Kena Upanishad

2.1. Background

Owing to their unique electromechanical, chemical and optical properties, two dimensional (2D) materials have generated substantial research activity during the last decade. Starting with graphene in 2004, the field has been witnessing a steady rise in the variety of 2D materials as well as their applications. The absence of certain desirable properties in graphene – such as plasticity [22], piezoelectricity [10] or a tunable electronic bandgap [23] – has motivated the search for other, more exotic 2D materials [24, 25]. Group VI transition metal dichalcogenides (TMDCs), with the general formula MX_2 (where M = Mo, W and X = S, Se, Te), are one such category of materials that has received a lot of attention recently. Atomically-thin TMDCs exhibit electromechanical properties that are strikingly different when contrasted with their bulk counterparts. Some TMDCs (for e.g. MoS_2) transition from an indirect to a direct band-gap semiconductor as the thickness is reduced to a monolayer [23]. This has allowed the realization of photodetectors with

ultrahigh responsivity [26], excitonic lasers [27, 28], among other demonstrations. Additionally, the ability to tune the band-gap (up to 60 meV, [29, 30]) using mechanical strain opens up applications in photovoltaics [31]. Lastly, the absence of inversion symmetry in monolayer TMDCs leads to an in-plane piezoelectric coefficient that is comparable to commonly used bulk piezo-crystals like quartz and wurtzite [32, 33]. In addition to device applications, TMDCs have served as a platform for exploring several interesting phenomena including the valley Hall effect [34, 35], second harmonic generation [36, 37] and structural phase transitions induced by electrostatic doping [38].

By virtue of their high elastic stiffness and low mass, nanoelectromechanical systems (NEMS) fabricated using 2D materials – such as graphene [39], graphene oxide (GO) [40] and TMDCs [41, 42] have fundamental resonance frequencies in 1-200 MHz range. Thus, they are promising candidates for force/mass sensing and RF-signal processing applications. When compared to micro-machined Si based and other one-dimensional (1D: nanowire, carbon nanotube) NEMS, resonators made of 2D materials provide unique advantages, such as a broad dynamic range [43, 44] and retained mechanical anisotropy as the thickness is reduced. For instance, the mechanical anisotropy in black phosphorus is one order of magnitude larger than that in Si. The anisotropy, as manifested in the resonant mode-shapes, can be utilized to resolve the crystal orientation in black phosphorus resonators [45, 46]. Lastly, 2D NEMS have served as avenues to explore an array of interesting nonlinear phenomena such as phonon-cavity strong coupling [3–5], cavity side band cooling, parametric self-oscillations [47] and quintic non-linearity [48]. Within the domain of 2D resonators, TMDC based NEMS offer several advantages over graphene counterparts. First, the resonance frequency in monolayer TMDC resonators can be tuned using

the piezoelectric effect instead of modulating the electrostatic back-gate voltage. Second, molecular dynamics (MD) calculations predict TMDC resonators to have better Q-factors than graphene [11, 49]. Lastly, the dominant dissipation mechanism in undoped TMDC resonators is typically clamping losses that are independent of temperature and can be improved with optimized fabrication, rather than electrostatic interactions with the substrate, which is the case with graphene [50].

A common method of fabricating 2D resonators is to exfoliate a bulk-TMDC crystal using the scotch-tape method onto a Si substrate with pre-patterned holes or trenches. Because the exfoliation process results in flakes of different thicknesses, a prior characterization step is required before measuring the resonance spectra. Raman spectroscopy is a high-throughput, non-contact method to characterize the layer number in few-layered TMDC flakes [51]. Additionally, resonant Raman spectroscopy has been used to investigate the electronic band-structure and phonon dispersion properties in TMDC crystals. Although several methods (optical, electrical, piezo/magneto-resistive) exist for NEMS actuation and motion transduction [52], cavity-interferometry has emerged as a popular, non-contact tool for detecting mechanical resonances in nanoresonators. Cavity-interferometry utilizes the underlying substrate as the reference mirror and the resonator as the moving mirror, obviating the need for an external reference arm such as that used in Michelson interferometry. Because the displacements involved are small (< 1 nm), the sample needs be in vacuum to eliminate any viscous damping effects. Here, we report a custom-built experimental setup that can simultaneously perform both Raman spectroscopy and cavity-interferometry measurements on TMDC nano-resonators in high vacuum (< 50 μTorr).

The current chapter is organized as follows: in section 2.2, the experimental methods for the fabrication, Raman-AFM characterization and cavity interferometric measurements of TMDC resonators are described. Section 2.3 presents both driven and undriven measurements on atomically-thin WS_2 resonators. Specifically, the thickness dependent behavior in these resonators and the noise floor in the experimental setup are discussed. The potential utility of the presented experimental setup in other experimental studies is discussed in section 2.4

2.2. Experimental Methods

2.2.1. Fabrication Protocol

Microfabrication techniques were employed here to fabricate the target substrate with patterned cavities (called the device chip hereafter, see Figure 2.1b) onto which exfoliated TMDC flakes were subsequently transferred. Figure 2.1 outlines the different steps in the fabrication protocol of TMDC resonators. A Si/SiO_2 (300 nm) wafer was spin-coated with a 100 nm thick positive e-beam resist (poly methyl methacrylate, PMMA C4, 1000 rpm for 45 sec) and the interdigitated electrodes were patterned with an electron beam (Raith 150, 450 μC/cm2 dose at 30 kV). The exposed PMMA was developed in a mixture of MIBK: IPA 1:3 for 30 sec, followed by a gold deposition step (100 nm thick with 0.5 nm Cr and 5 nm Ti as adhesion layers) using e-beam evaporation. A standard lift-off process was then performed in anisole at 75°C to remove PMMA so that only the desired Au electrode patterns were left on the Si/SiO2 wafer (Figure 2.1b). To further increase and control the cavity depth, reactive ion etching (Samco RIE 10NR) was used to selectively

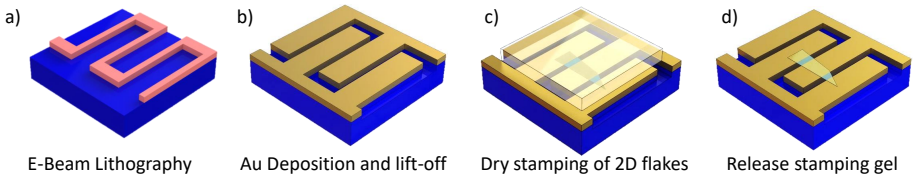

Figure 2.1. Fabrication steps involved in making WS_2 resonators. (a) – (b) E-beam lithography, Au evaporation deposition, lift-off and reactive ion SiO_2 etch are performed sequentially to create the device chip. (c) Then, a dry stamping step is carried out where few-layered WS_2 flakes are attached to the bottom of the gel-film. (d) After the intermediate gel-film is removed, suspended WS_2 flakes are left on the electrodes due to van der Waal's adhesion with the gold surface

etch away approximately 200 nm of SiO2 resulting in a final cavity depth of 300 nm. Few-layered TMDC flakes were mechanically exfoliated using the scotch-tape method that has been widely reported [53]. The exfoliated TMDC flakes were first transferred to a piece of gel-film that served as an intermediate carrier between the scotch tape and device chip to obtain better yield and less polymeric residue during the transfer process [54]. The gel-film was gently contacted with the device chip and moderate pressure was applied, then slowly detached from the device chip leaving the TMDC flakes adhered to the electrodes.

2.2.2. Characterization Techniques

(1) Raman Spectroscopy: Raman spectroscopic measurements were used in conjunction with other characterization methods (AFM, see below) to identify the number of layers in the exfoliated samples. A He-Ne red-laser (632.8 nm wavelength, avg. power < 450 μW) was focused to a spot size of less than 2 μm using a 50X long working distance (LWD) objective (NA 0.55). The reflected and scattered light were collected by the same objective and passed through a Rayleigh filter

(efficient to < 100 cm^{-1}) followed by a motorized Czerny-Turner spectrograph (1800 grooves/mm) that was coupled to a Peltier cooled EMCCD (Andor Newton). The spectral resolution of the system is < 1 cm^{-1} and the peak centroids were identified by fitting the spectra to a multi-peak Lorentzian line shape.

(2) Atomic Force Microscopy: An AFM cantilever probe (42 N/m stiffness and 320 kHz fundamental resonance frequency) was used in tapping mode on a Park XE-120 system to generate a topographical map of the TMDC flake. Line scans from multiple areas of the flake were averaged and the mean value is reported as the thickness.

(3) Scanning Electron Microscopy: Successful fabrication of device chips and the subsequent transfer of TMDC flakes was verified using a FEI Nova 600 SEM that was operated at 10kV acceleration voltage.

2.2.3. *In vacuo* Cavity Interferometry Setup

Figure 2.2 shows the different components in our experimental setup which are described next. A custom designed chamber was used to achieve vacuum level of < 50 μTorr in 2 hours using a turbo-molecular pump (HiCube 80 Eco). The vacuum level was measured using a pirani/cold-cathode gauge (Pfeiffer MPT 200). The sample was mounted on a vacuum compatible, XYZ piezo-actuator stack (Attocube ECS 3030) with nanometer spatial resolution. A multi-pin electrical feedthrough on the vacuum chamber allowed the application of the driving voltage to the PZT disk underneath the sample. The probe laser (He-Ne, 632.8 nm wavelength) was focused onto the sample to a spot size of less

than 2 μm using a 50X long working distance (LWD) objective (N.A. 0.55). An anti-reflection coated viewport was used to minimize back-reflections and ghosting. The laser power was measured outside the vacuum chamber and was kept to < 450 μW to minimize sample heating. The nanoresonator and the Si substrate underneath form an optical cavity whose reflectance is modulated by the motion of the resonator and is measured on a fast photodiode. An RF function generator (Agilent 33250a) was used to drive the PZT disk; the photocurrent generated on the photodiode was first amplified using a trans-impedance amplifier and then fed to the RF-input of a lock-in amplifier (SR844). A custom-written Python routine was used to communicate with the lock-in amplifier and the function generator using the GPIB and RS-232 serial interface, respectively. A spectrum analyzer (Rigol 815-TG) was used to measure the undriven thermomechanical resonances.

2.2.4. Optimizing Cavity Responsivity

The cavity depth is a crucial factor in determining the responsivity of the interferometer, where the responsivity (R) is defined as the change in reflectance per unit motion of the resonator, i.e. $\frac{dR}{dz}$, where I_r is the intensity of the reflected light. A thin film interference model can be used to determine the cavity's responsivity (see Figure 2.3). For a given intensity of incident light I_0, the intensity of the reflected light I_r from the optical cavity can be estimated using the following equation [55]

$$\frac{I_r}{I_0} = \left| \frac{r_1 e^{i(\phi_1+\phi_2)} + r_2 e^{-i(\phi_1-\phi_2)} + r_3 e^{-i(\phi_1+\phi_2)} + r_1 r_2 r_3 e^{-i(\phi_1-\phi_2)}}{e^{i(\phi_1+\phi_2)} + r_1 r_2 e^{-i(\phi_1-\phi_2)} + r_1 r_3 e^{-i(\phi_1+\phi_2)} + r_2 r_3 e^{-i(\phi_1-\phi_2)}} \right|^2 \tag{2.1}$$

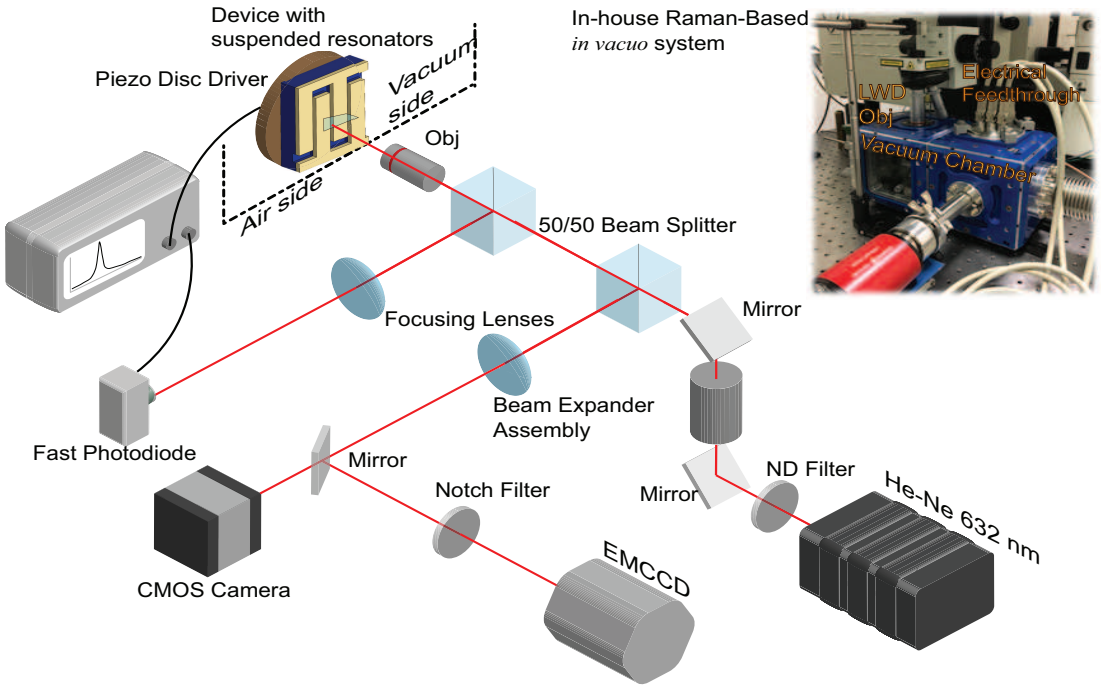

Figure 2.2. Schematic showing the *in vacuo* optical setup for Raman spectroscopy and cavity-interferometry. The device chip is attached to a piezo-disc and mounted inside the vacuum chamber. Electrical and optical signals are coupled into and out of the chamber through electrical feedthroughs and an anti-reflective view-port, respectively. Free-space optical components are configured to enable simultaneous interferometry, Raman spectroscopy and optical microscopy

In equation 2.1, r_1, r_2 and r_3 are reflection coefficients at the vacuum-resonator, resonator-vacuum and vacuum-substrate interface; and are given by the following relations (n_v, n_r, n_{Si} are the refractive index of vacuum, resonator and Si respectively).

$$
\begin{aligned}
r_1 &= \frac{n_v - n_r}{n_v + n_r} \\
r_2 &= \frac{n_r - n_v}{n_r + n_v} \\
r_3 &= \frac{n_v - n_{Si}}{n_v + n_{Si}}
\end{aligned}
$$

The phase shifts ϕ_1, ϕ_2 are given by $\phi_1 = \frac{2\pi n_r d_r}{\lambda}$ and $\phi_2 = \frac{2\pi n_v d_v}{\lambda}$, where d_r, d_v are the resonator thickness and the cavity depth, respectively, while λ is the wavelength of the probe laser (632.8 nm). In Figure 2.3, the reflectance of the optical cavity is calculated for a monolayer (black, solid line), 10 layer (red line with circular marker) and 30 layer WS_2 resonator (blue, dashed line), using $n_{Si} = 3.881 - 0.0019i$, $n_r = 5.6104 - 0.7293i$ and $n_v = 1$. The slope of the curve at $d_v = 300$ nm determines the responsivity of the cavity. Several conclusions can be drawn from this analysis: the chosen cavity depth yields good responsivity values for resonator thicknesses ranging from a monolayer to 30 layers; the responsivity increases with increasing thickness; and finally, for some cavity depth values (the minima in the curves, near 360 nm), the responsivity can be close to zero and should be avoided.

2.2.5. Raman Spectroscopy and AFM Characterization

Here, we highlight the main features in the Raman spectrum of WS_2 that are utilized to infer the number of layers and point the reader to refs. [51, 56, 57] for a more in-depth discussion of the different phonon modes in TMDCs. The Raman spectrum of WS_2 is characterized by two first order modes at the Brillouin zone center, i.e. an in-plane E^1_{2g} mode and an out of plane A^1_g mode. In the E^1_{2g} mode, the tungsten (W) atom and the pair of sulfur (S) atoms vibrate away from each other; whereas in the A^1_g mode, the S atoms move out of plane relative to W (see Figure 2.4b, 2.5b). As the thickness of WS_2 is reduced, changes in interlayer interactions produce a well characterized softening (red-shift) of the A^1_g mode and smaller (≈ 1 cm^{-1}) non-monotonic shifts in the E^1_{2g} mode. Thus, the spacing between the two phonon modes serves as a useful metric for identifying the layer number,

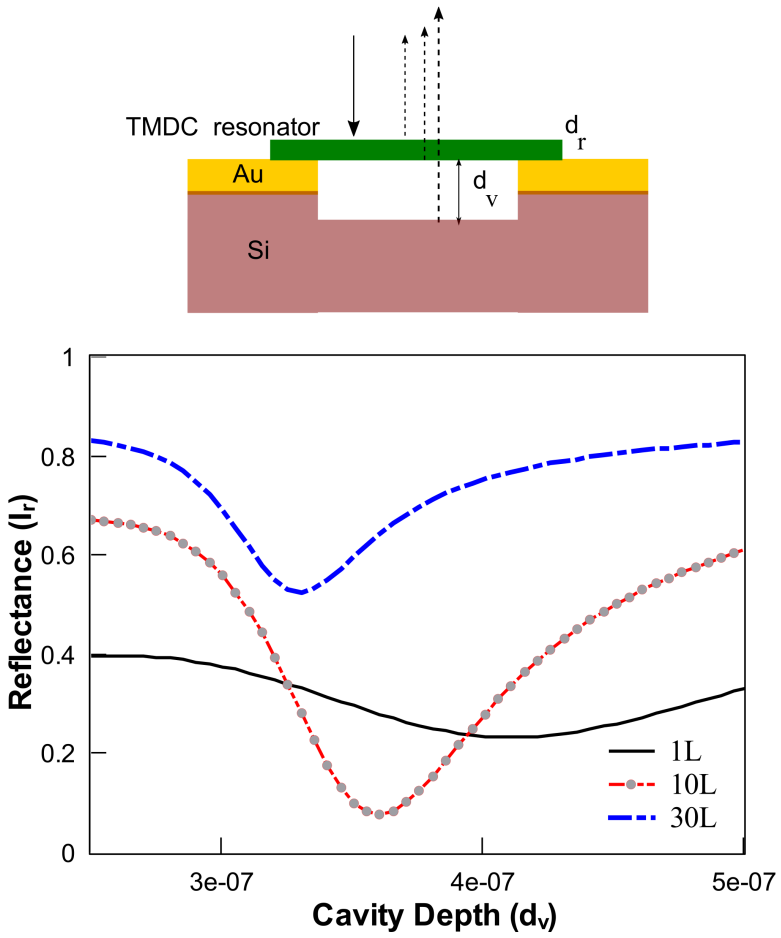

Figure 2.3. Schematic showing the thin film interference model used to calculate the responsivity of the interferometer. Solid arrows indicate incident light and dashed arrows indicate the reflected light. A cavity depth (d_v) of 300 nm is chosen to maximize the responsivity. d_r denotes the resonator thickness

and a difference of 66 cm^{-1} between the two modes is indicative of a monolayer [56]. We note that the absolute positions of each of these modes depend differently on the presence of strain, dopants or impurities [58] induced during the fabrication step. As such, a one-time calibration of the spacing between the phonon modes as a function of the flake's thickness using AFM is necessary. Also, Raman spectroscopy is most useful in discerning

the thickness of few-layered flakes (<10) and the frequency spacing quickly saturates for flakes that are much thicker than 10 layers.

The resonator flakes are imaged with an AFM in tapping mode using scan areas that are large enough to cover both the suspended region as well as that in contact with the electrodes. The uniformity in surface topography across the entire scan region indicates that the flake thickness is consistent across the suspended and adhered areas; so, the height measurements taken on the supported regions are used to characterize the thickness of the resonator. The three resonators reported in this manuscript have thickness values of 125 nm (Figure 2.4a), 12 nm (Figure 2.5a) and 7 nm (see Supporting Information A, Figure A.1) respectively, as confirmed through AFM. Their corresponding frequency separation values between the phonon modes (A_g^1, E_{2g}^1) are 72.5 cm^{-1}, 70.2 cm^{-1} and 69.8 cm^{-1}.

2.3. Measurements on Atomically-Thin Tungsten Disulfide Resonators

2.3.1. Thermomechanical Resonances and Noise Floor in the Setup

We first discuss the measurement of thermomechanical resonances in WS_2 resonators. The thermal fluctuations in the position of the resonator modulate the depth of the optical cavity, and consequently the intensity of light reflected from the cavity. The light collection efficiency in our experimental setup is high enough to resolve the Brownian motion in the resonators without the need for external actuation. Figure 2.4a shows an optical micrograph of a WS_2 resonator that is 125 nm thick (186 layers), as confirmed by AFM topography scan (Figure 2.4a) and Raman spectroscopy (Figure 2.4b). Figure 2.4c presents the thermomechanical resonance spectrum of the fundamental mode of the resonator. By fitting the resonance data to a Lorentzian line-shape, we obtain $\frac{\omega_0}{2\pi} =$

63.524 ± 0.002 MHz and a Q-factor of 749. For a spring-dash pot system with a quality factor Q, effective mass Me and resonance frequency ω_0, the displacement power spectral density (PSD) of the system, as a function of the frequency (ω), is given by

$$S_x = \frac{4k_bT\omega_0}{QM_e}\left[\frac{1}{(\omega_0^2-\omega^2)^2+(\omega\omega_0/Q)^2}\right] \tag{2.2}$$

In equation 2.2, k_b is the Boltzmann constant, T, M_e are the temperature (in Kelvin) and effective mass of the resonance. On resonance, the displacement PSD reduces to $S_x = \frac{4k_bTQ}{M_e\omega_0^3}$. Assuming $T = 300$ K and using $M_e = 0.8M$, where M is the mass of the resonator (≈ 16.88 pg), $\sqrt{S_x} \approx 0.014$ pm Hz$^{-1/2}$. The displacement PSD is transduced to a voltage PSD by the photodiode and backend electronics in the setup, and is given by

$$S_V = \Phi^2\left|\frac{4k_bT\omega_0}{QM_e}\left[\frac{1}{(\omega_0^2-\omega^2)^2+(\omega\omega_0/Q)^2}\right]\right| + S_N \tag{2.3}$$

In equation 2.3, Φ (units of μV/pm) and S_N are the responsivity and noise floor of the photodiode-amplifier combination, respectively. The noise floor of our detection system is $S_N \approx 1.4$ μV Hz$^{-1/2}$, which when converted to displacement units yields a displacement sensitivity of 12 fm Hz$^{-1/2}$ and a responsivity of $\Phi \approx 117$ μV/pm for the WS_2 resonator in Figure 2.4. The displacement resolution in our setup is limited by the noise in the transimpedance amplifier. Figure 2.4d shows the driven response of the resonator using a drive voltage of 0 dBm ($V_{rms} = 0.224V_{p-p}$) to the PZT disk; the dashed line is Lorentzian curve fit to the obtained data.

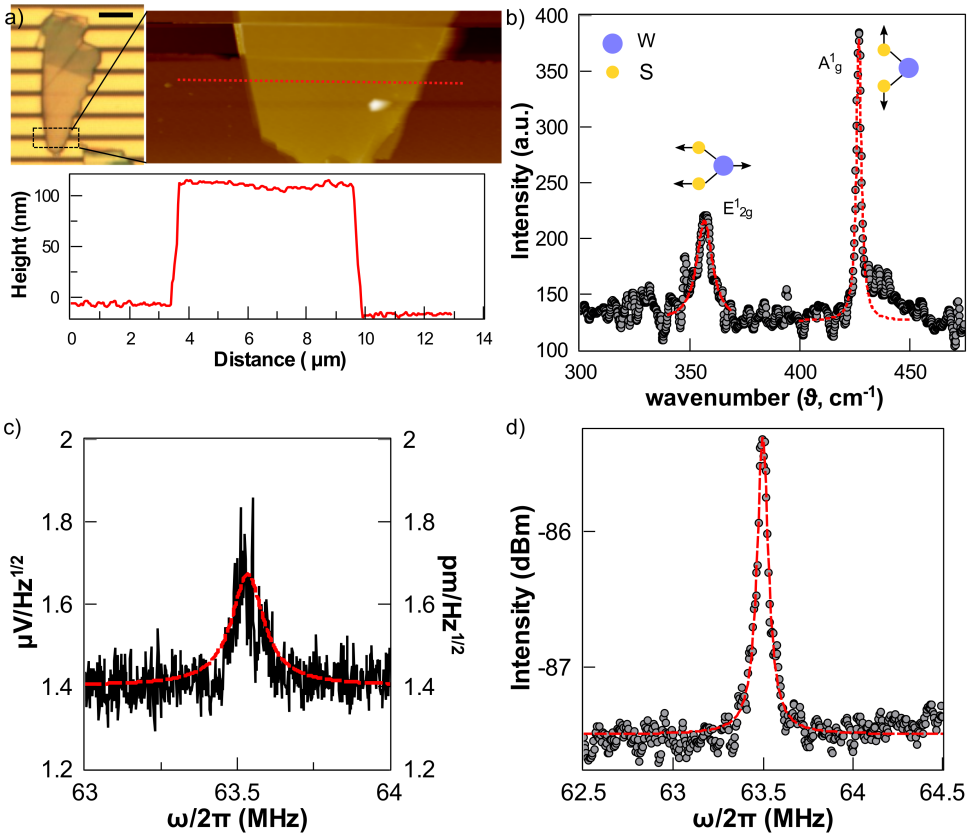

Figure 2.4. (a) Optical micrograph (left, scale bar: 20 μm) and tapping mode AFM scan (right) to determine the thickness of the resonator (dashed box). The resonator is approximately 125 nm thick. (b) Raman spectrum showing the in-plane E^1_{2g} and out of plane A^1_g modes with a separation of >70 cm^{-1} indicating >10 layers. Red, dashed lines are a Lorentzian fit to the measured data, denoted by grey circles. (c) Thermomechanical resonance spectrum of the resonator with a fundamental frequency of 63.524 MHz and a Q-factor of 749. Black line indicates the measured displacement and the red, dashed line is a Lorentzian fit. (d) Driven oscillations of the resonator with a driving amplitude of 224 mV to the PZT disc; the dashed line is a Lorentzian fit to the raw data (grey circles)

2.3.2. Thickness Dependent Dynamical Behavior of 2D Resonators

The resonance frequency of a thin-plate under tension can be expressed as $f = \sqrt{f_\sigma^2 + f_E^2}$.

Here, the term f_σ is the contribution to the resonance frequency from a membrane model

assuming negligible bending stiffness D, ($D = \frac{E_Y h^3}{12(1-\nu^2)}$ where E_Y is the elastic modulus, h is the resonator thickness and ν is the Poisson's ratio), while f_E is the contribution obtained from the elasticity solution by neglecting any prestress. Depending on the relative contributions from the two terms, the resonator could be in (1) the plate regime, where the bending rigidity dominates; (2) the membrane regime, where the behavior is governed predominantly by the prestress; or (3) a mixed-regime where both contributions are comparable and need to be accounted for. The expressions for f_σ and f_E depend on the resonator geometry and the boundary conditions. For a resonator with a rectangular geometry, the general expression for f_E is given by

$$f_E^2 = \frac{\pi^2 D}{4a^4\rho}\left[G_x^4 + G_y^4 + 2(a/b)^2\left\{\nu H_x H_y + (1-\nu)J_x J_y\right\}\right] \tag{2.4}$$

In equation, the factors G_i, H_i and J_i ($i = x, y$) depend on the boundary conditions: a, b are the length and width of the resonator, respectively; ρ is the areal mass density; and ν is the Poisson's ratio. The expression has been derived using the Rayleigh-Ritz method in ref. [59]. For free-boundaries along the y direction and the fundamental mode, $G_y = H_y = J_y = 0$, and the equation simplifies to $f_E^2 = \frac{\pi^2 D}{4a^4\rho} G_x^4$. Further $G_x = 1.0$ for the fundamental mode and simply supported edges along the x direction. $f_\sigma = (n/2L)\sqrt{T/\rho}$ for a 1-D string under tension, where n is mode number and T is the prestress. For the resonator shown in Figure 2.5, assuming an isotropic elastic modulus of $E_Y = 270$ GPa (which is valid for strains less than 0.01, [60]), $\nu = 0.25$ and $\rho = 7500h$ kg m$^-$2, $f_E \approx 70.24$ MHz, which is close to the observed resonance frequency of 63.52 MHz and indicates that the resonator is in the plate regime.

Figure 2.5a shows an optical micrograph and AFM topography data of a WS_2 resonator that is 12 nm thick. Raman spectroscopy on the same resonator (Figure 2.5b) yields a spacing of 70.24 ± 0.07 cm^{-1} between the in-plane E^1_{2g} mode and the out of plane of A^1_g mode. Figure 2.6a shows the resonance spectra of the sample actuated with a driving voltage of +30 dBm ($V_{rms} \approx 7$V) applied to the PZT disc. The first five modes of resonance have been indicated in Figure 2.6a using vertical dotted lines. The displacement of the PZT disc is non-uniform and particularly pronounced in the 1-5 MHz span, which results in the large, non-uniform background for Modes 1-3 [47]. The two closely spaced resonance modes near 17 MHz are both attributed to Mode 4. Figure 2.6b-d show the measured data (grey circles) for the first three modes and a Lorentzian line-shape fit (red, solid line) to each. Table 1 summarizes the peak-locations and the full width at half-maximum (FWHM) values for the first five modes. The smaller fundamental frequency, as compared to the 125 nm thick resonator, is consistent with the smaller bending rigidity as the thickness is reduced to 12 nm.

Figure 2.7 presents experimental data on a few-layered WS_2 resonator. AFM topography scan reveals the resonator thickness to be 7 nm (see Supporting Information Figure A.2), i.e. a total of 9 layers. Fitting the Raman spectroscopy data in Figure 2.7a to a Lorentzian line-shape for each of the in-plane (E^1_{2g}) and the out of plane (A^1_g) modes yields a spacing of 69.8 cm^{-1} between them, which can serve as calibration for identifying resonators with similar thickness. Figure 2.7b presents the fundamental mode of the WS_2 resonator with a peak centroid $\omega/2\pi = 9.1 \pm 0.1$ MHz and full width at half maximum $\Delta\omega/2\pi = 0.36$ MHz. The contribution from the bending stiffness to the fundamental mode's frequency can be estimated as $f_E^2 = \frac{\pi^2 D}{4a^4\rho} G_x^4$, which yields $f_E \approx 3.93$ MHz. The

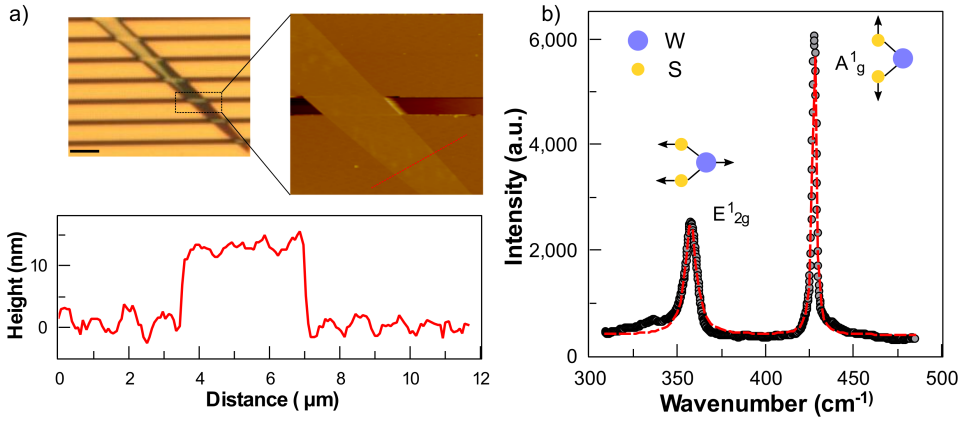

Figure 2.5. (a) Optical micrograph (left, scale bar: 20 μm) and tapping mode AFM topography image (right) to determine the thickness of the resonator (dashed box). The resonator is approximately 12 nm thick. (b) Raman spectroscopy showing the in-plane E^1_{2g} and out of plane A^1_g modes with a separation 70.24$\pm$0.07cm^{-1}. (Red, dashed lines indicate a Lorentzian fit to the measured data)

estimated value accounts for only 20% of the observed value. This suggests that the resonator is in the mixed regime where contributions from both the prestress and bending stiffness are important. Using $f_\sigma = (1/2L)\sqrt{T/\rho}$, the average pre-stress in the resonator can be estimated as $T \approx 56.5$ mN/m, which is typical in suspended 2D materials (refs. [12], [22] and [48]).

Table 2.1. Resonance frequencies and FWHM values for the first five modes of the 12 nm thick WS_2 resonator

Mode #	$\omega/2\pi$(MHz)	$\Delta\omega/2\pi$(MHz)
1	1.94 $\pm$ 0.02	0.3 $\pm$ 0.1
2	3.03 $\pm$ 0.04	0.3 $\pm$ 0.1
3	4.94 $\pm$ 0.01	2.2 $\pm$ 0.8
4	16.28 $\pm$ 0.08 18.02 $\pm$ 0.07	0.9 $\pm$ 0.4 2.5 $\pm$ 0.8
5	27.23 $\pm$ 0.02	3.1 $\pm$ 0.4

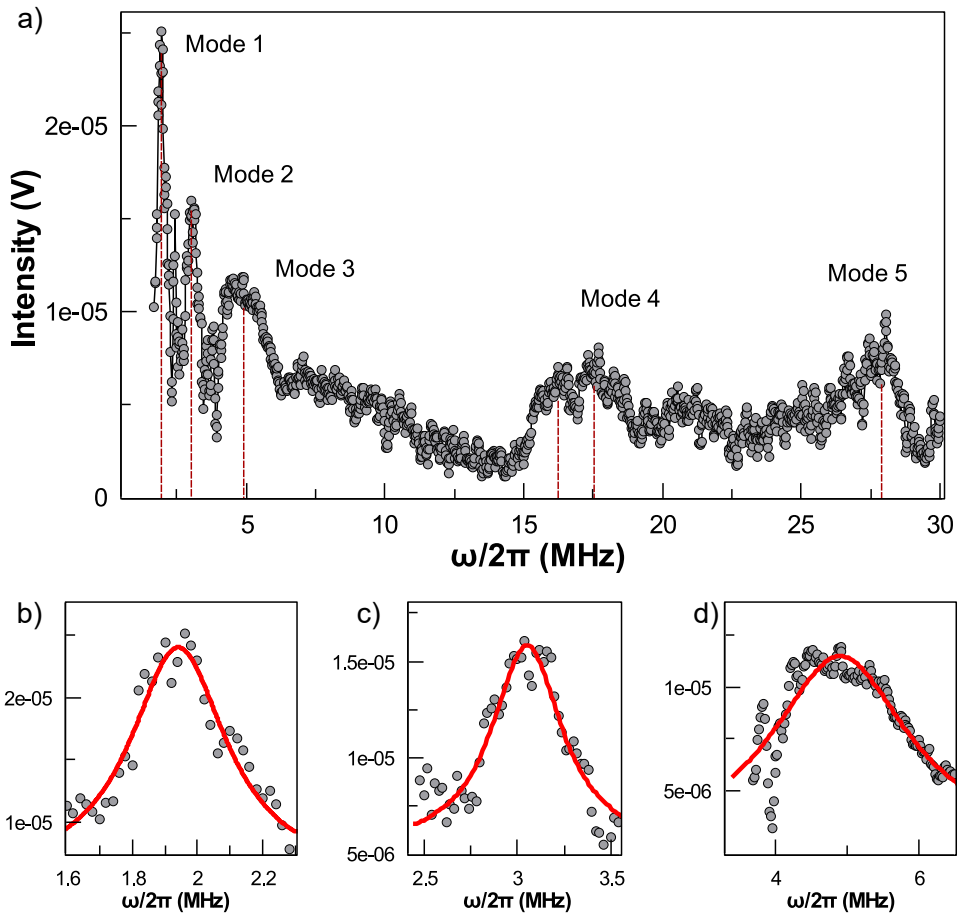

Figure 2.6. (a) Voltage vs frequency plot showing the first five resonance modes of the 12 nm thick WS_2 resonator. A drive voltage of +30 dBm was applied to the PZT disc. A Lorentzian line-shape (red, solid line) was fit to the measured data corresponding to modes 1, 2 and 3 in (b), (c) and (d) respectively. The center frequency and FWHM of each mode are listed in Table 2.1

2.4. Summary and Future Work

In this chapter, a custom-built *in vacuo* experimental setup is described for making combined Raman spectroscopy and cavity-interferometry measurements on TMDC resonators that were fabricated using mechanical exfoliation and dry transfer onto microfabricated device chips. As a proof of concept, we investigated the mechanical resonances

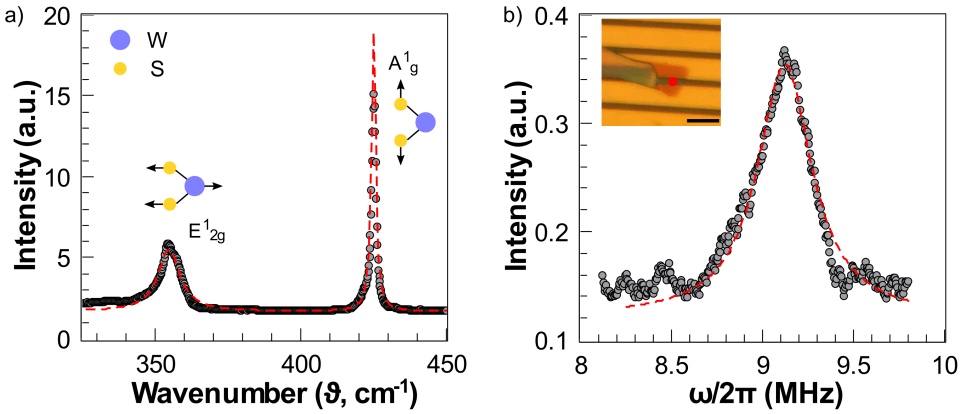

Figure 2.7. (a) Raman spectroscopy characterization of a few-layeredWS_2 resonator. The spacing between the in-plane E^1_{2g} and out of plane A^1_g modes is 69.8 cm^{-1}. AFM characterization reveals the thickness to be 7 nm (9 layers). (b) The fundamental resonance mode under driven oscillations ($2V_{rms}$ to the PZT disc) is shown where the red, dashed line is a Lorentzian fit to the measured data (grey circles). Inset shows an optical micrograph with scale bar=10 μm, the red dot indicates the region on the resonator where the measurements were taken

in multilayered WS_2 resonators shown to be in the plate-regime and a few-layered WS_2 resonator that was in the mixed-regime. One of the advantages of combining the two experimental techniques is the prevention of sample degradation, which can be particularly problematic for the selenides ($MoSe_2$, WSe_2) and tellurides ($MoTe_2$, WTe_2) in TMDC family. The combination allows us to not only encapsulate the exfoliated samples in an inert, high-vacuum environment but also to identify few-layered flakes (using Raman spectroscopy) in a high throughput manner for subsequent resonator measurements. Because of the sensitivity and the abundant data available on Raman characterization of 1-5 layered TMDC flakes (see Table 2.2), the reported experimental setup is best utilized when dealing with monolayers or few-layers, although their controlled, large-scale fabrication is presently a challenge. Raman spectroscopy can also serve as a non-destructive,

local probe of motion and stress in nano-mechanical systems [61]. The softening of the in-plane phonon mode at different driving frequencies can be used as an indicator of both the resonance frequency as well as the local strain, although the bandwidth of our EM-CCD detector (1 MHz) precludes us from implementing this functionality in our setup [61]. The device chips serve as a versatile platform for the investigation of resonators fabricated using other 2D materials and for implementing other actuation and detection modalities. For instance, although we have utilized piezo-actuation for driving the resonators in this study (primarily for its simplicity), the inter-digitated electrodes on the device chips can be exploited to implement capacitative actuation and all electrical methods of detection, such as mixed-down and frequency modulation (FM) techniques. Lastly, the optical cavity formed by the resonator and underlying substrate can be utilized to study opto-mechanical phenomena such as intermodal strong coupling, photo-thermal sideband cooling, and parametric self-oscillations.

2.5. Acknowledgments

I am thankful to Siyan Dong for leading the fabrication and AFM characterization efforts. I am grateful to Prof. Lincoln James Lauhon for providing valuable comments on a manuscript (Exp Mech (2018). https://doi.org/10.1007/s11340-018-00452-5) that was based on this chapter. The work was generously funded by the Army Research Office (ARO) through Grant No. W911NF1510068. Support is acknowledged from the Center for Nanoscale Materials (CNM, Argonne National Lab), an Office of Science user facility, supported by the U.S. Department of Energy, Office of Science, Office of Basic

Table 2.2. Summary of important features in the Raman spectra of different few-layered TMDCs that can be utilized to infer the layer number. nL denotes a TMDC flake with "n" layers

TMDC	Features in Raman Spectra utilized to distinguish few-layered to monolayer flakes
MoS_2	The spacing between the E^1_{2g} and A^1_g modes is 18, 22.4, 23.3 and 24.3 cm^{-1} for 1L, 2L, 3L and 4L respectively (ref. [51])
WS_2	The spacing between the E^1_{2g} and A^1_g modes is 65.5, 68.3 and 69.2cm^{-1} for 1L, 2L and 3L and 3L respectively (ref. [62])
$MoSe_2$	The A^1_g mode softens with decreasing thickness; starting from 242.5 cm^{-1} for 5L, the mode redshifts to 240.5 cm^{-1} for 1L (ref. [63]). For 3L to 5L, the mode splits into two peaks, which can serve as an additional confirmation of the layer number
WSe_2	The E^1_{2g} and A^1_g modes coincide for 1L; the separation increases from 1.5 cm^{-1} for 2L to 3 cm^{-1} for bulk. Alternatively, the intensity ratio of A^1_g and E^1_{2g} modes can be used to infer the number of layers (refs. [63, 64]), where the ratio increases with increasing thickness (2.5 for 2L and 8 for bulk)
$MoTe_2$	The B^1_{2g} mode, which is inactive in bulk form, is active in few-layered flakes but not in 1L $MoTe_2$ (refs. [65, 66]). The intensity ratio of B^1_{2g} and E^1_{2g} modes can be used to distinguish 2L-5L flakes (see ref. [65]). For 1L, the absence of B^1_{2g} phonon mode and a high intensity of A^1_g mode (under 633 nm excitation, compared to bulk) confirms monolayer thickness (ref. [66])

Energy Sciences, under Contract No. DE-AC02-06CH11357. This work also utilized Northwestern University Micro/Nano Fabrication Facility (NUFAB), which is partially supported by Soft and Hybrid Nanotechnology Experimental (SHyNE) Resource (NSF ECCS-1542205), the Materials Research Science and Engineering Center (NSF DMR-1720139), the State of Illinois, and Northwestern University.

CHAPTER 3

Transition Metal Dichalcogenide Resonators in the Strongly Nonlinear Regime

From the early great Upanishads, the recognition Athman = Brahman upheld in (the personal self equals the omnipresent, all-comprehending eternal self) was in Indian thought considered, far from being blasphemous, to represent the quintessence of deepest insight into the happenings of the world.

What is Life, by Erwin Schrodinger

3.1. Background

The dynamical behavior of a continuous system is characterized by infinite degrees of freedom, each with a linearized natural frequency ω_i, where $i = 1, 2, \ldots \infty$. If some of the frequencies are commensurate or nearly commensurate, i.e. if there exist integers k_i (not all of them zero), satisfying $k_{11} + k_{22} + \cdots + k_{pp} \approx 0$, the system is said to be in a state of internal or autoparametric resonance (IR) [67–69]. The existence of IR in nonlinear oscillators can lead to complex behaviors - such as exotic line-shapes under forced oscillations, amplitude saturation due to strong inter-modal coupling and energy dependent dissipation rates - that have no analogue in linear oscillators [70–73].

Nanoelectromechanical systems (NEMS) can be driven into the nonlinear regime even at modest actuation forces due to their small thickness (bending rigidity), and therefore, have been the subject of research during the past decade [74, 75]. A common source

of nonlinearity in NEMS is the displacement induced correction to pre-stress that may result in inter-modal coupling. Inter-modal coupling in clamped-clamped resonators has been creatively used in pump-probe experiments to a) detect modes where the shift in the resonant frequency of the probe mode serves as an indirect signature of the resonance behavior of the pump mode [76, 77], and b) to increase the dynamic range of a probe mode by driving the pump mode into the nonlinear regime. The nonlinear behavior in a hardening Duffing oscillator has been used to engineer a 1:3 IR that allowed for frequency stabilization and coherent energy transfer between the coupled modes [70, 72]. Mode-coupling has also been demonstrated in other one-dimensional structures such as nanowires [78] and nanotubes [79] and more recently in NEMS fabricated using two dimensional (2D) materials such as graphene and few-layered molybdenum disulfide (MoS_2) [3–5, 73, 80, 81].

The organization of the chapter is as follows: in section 3.2, the thermal motion and weakly nonlinear behavior of the nanoresonator are measured. Section 3.3, presents data related to the multiple pairs of 1:1 internal resonance that appear under a strong driving force. Bifurcation analysis on a subset of the modes is presented in section 3.4 to explain the exotic line-shape observed in experiments. Applications that would benefit from the nonlinear behavior of 2D NEMS are discussed in section 3.5 and natural extensions of the present work are mentioned in section 3.6.

3.2. Thermomechanical Resonance and Weakly Nonlinear Behavior

The monolayer WS_2 nanoresonator (Figure 3.1a) was fabricated using a combination of mechanical exfoliation onto an SiO_2 wafer, potassium hydroxide (KOH) assisted poly

methyl methacrylate (PMMA) transfer of optically identified monolayer flakes onto a pristine Si/SiO_2 wafer and e-beam lithography/lift-off techniques (see Supporting Information B.1 for more details). The resonator was sandwiched between Au electrodes at the top and exposed negative e-beam resist (hydrogen silsesquioxane, HSQ) at the bottom. The cavity depth was determined by the thickness of the spin-coated HSQ, and a value of 375 nm was chosen as it predicted good responsivity values for monolayer WS_2 based on a thin film interference model (see Supporting Information B.2). Raman spectroscopy was employed to identify the thickness of few-layered TMDC samples. Specifically, the Raman spectrum of WS_2 was characterized by the in-plane E^1_{2g} and out of plane A^1_g phonon modes. It is known that the A^1_g mode undergoes softening as the thickness of WS_2 is reduced and hence, the spacing between the two phonon modes is indicative of the number of layers. Raman spectroscopy measurement (Figure 3.1b, also see Supporting Information B.3) revealed a spacing of 66 cm^{-1} between the two phonon modes, confirming that the nanoresonator is one layer thick [62]. Figure 3.1c presents a schematic of the experimental setup [82], where a He-Ne laser (632.8 nm, average power < 450 μW) is used as a probe beam and is focused on the nanoresonator, to a spot size of less than 2 μm, using a long working distance objective (NA = 0.55). The chip-carrier containing the sample is mounted on a lead zirconate titanate (PZT) disc ($d_{33} = 330$ pm/V) that actuates the different resonance modes of the nanoresonator; and the chip-carrier/PZT disc assembly is housed inside a custom-built vacuum chamber (vacuum level $< 10^{-5}$ Torr) with electrical feedthroughs and optical viewports. The underlain Si substrate and the nanoresonator form an optical-cavity whose reflectance, modulated by the latter's motion, is measured on a fast photodiode. An RF signal generator provides the driving signal to the PZT disc

whereas a lock-in amplifier measures the photodiode voltage. A spectrum analyzer was used in the thermo-mechanical resonance measurements.

Figure 3.1d shows the undriven resonance spectrum acquired at room temperature, with a resolution bandwidth of 100 Hz, using different laser powers. The measured data were fit to a Lorentzian line-shape composed of two resonance peaks as it improved the fitting. Also, modal analysis (see Supporting Information B.4) revealed that the first and second modes have closely spaced frequencies and are characterized by mode-shapes whose maximum out of plane displacement occurs near the center of either free-edge. For the case where the probe power was 180 μW, curve-fitting yielded frequency centroids 1.0429, 1.0443 MHz and Q-factors of 617 ($\pm$500), 2472 ($\pm$750) for the two modes. The lower Q-factor of mode 1 is due to poor signal to noise ratio (SNR) at this probe power. Increasing the probe power to 450 μW resulted in a reduction of the second mode Q-factor to 1200 ($\pm$110), along with a blue-shift of the frequency centroids (1.0462, 1.0477 MHz). The lowering of Q-factor with increasing probe power reported here (Figure 3.1e) is consistent with previous measurements on WSe_2 monolayer resonators, where it was shown that the Q-factor decreases due to heating from the probe laser and photo-thermal back-action from the optical cavity [83]. Photo-thermal back-action is an optomechanical effect that results in a time-delayed force on the resonator, and effectively modifies its damping [84]. Depending on the sign of the photo-thermal force gradient (∇F), the motion of the resonator is either amplified ($\nabla F<0$) or quenched ($\nabla F>0$) [84]. In our measurements, the peak signal intensity varies linearly with the probe power (Figure 3.1e); consequently, we rule out any photo-thermal back-action effects and attribute the decrease in Q-factor to sample heating. We also note that the Q-factor reported here (at room temperature) is

approximately one order of magnitude higher than previous reports on monolayer TMDC resonators with similar sample dimensions [2, 83, 85]. In order to fully understand the source of this improvement, further measurement of Q-factors at different temperatures is needed to account for both intrinsic and extrinsic damping sources. The higher Q-factor may partly be due to the robust clamping scheme and the absence of electrostatic damping that is otherwise prevalent in measurements that employ capacitive actuation [86].

The resonance frequencies of the sample were estimated using modal analysis with finite elements (see Supporting Information B.4) without including any prestress. The Young's modulus of the material ($E_Y = 270$ GPa) was assumed to be isotropic, which is a valid assumption for strains less than 0.01 as shown previously [87]. We employed a thin-shell thickness of 0.34 nm that facilitates the use of continuum theory for describing the behavior of 2D WS_2 resonators, while ensuring that the bending rigidity value is consistent with first principle calculations [88, 89] (see Table B.1 for a complete list of parameters used in the modal analysis). The resonance frequency of the fundamental mode without prestress was estimated to be 0.47 MHz; which is smaller than the observed value of 1.0462 MHz. The WS_2 nanoresonator reported here is in the mixed regime (also see Section 2.3.2), as is evident from $f_\sigma < f_E$, necessitating the inclusion of prestress. We repeated the modal analysis by incorporating a uniform prestress (σ_0) in the plate along the direction perpendicular to the clamped edges. The predicted and measured values for the resonance frequency of mode 1 coincided for $\sigma_0 \approx 45$ μN/m. For perspective, this value is three orders of magnitude smaller than previous reports on MoS_2 drum-head resonators [90, 91] and comparable to H-shaped graphene resonators [92]. The smaller

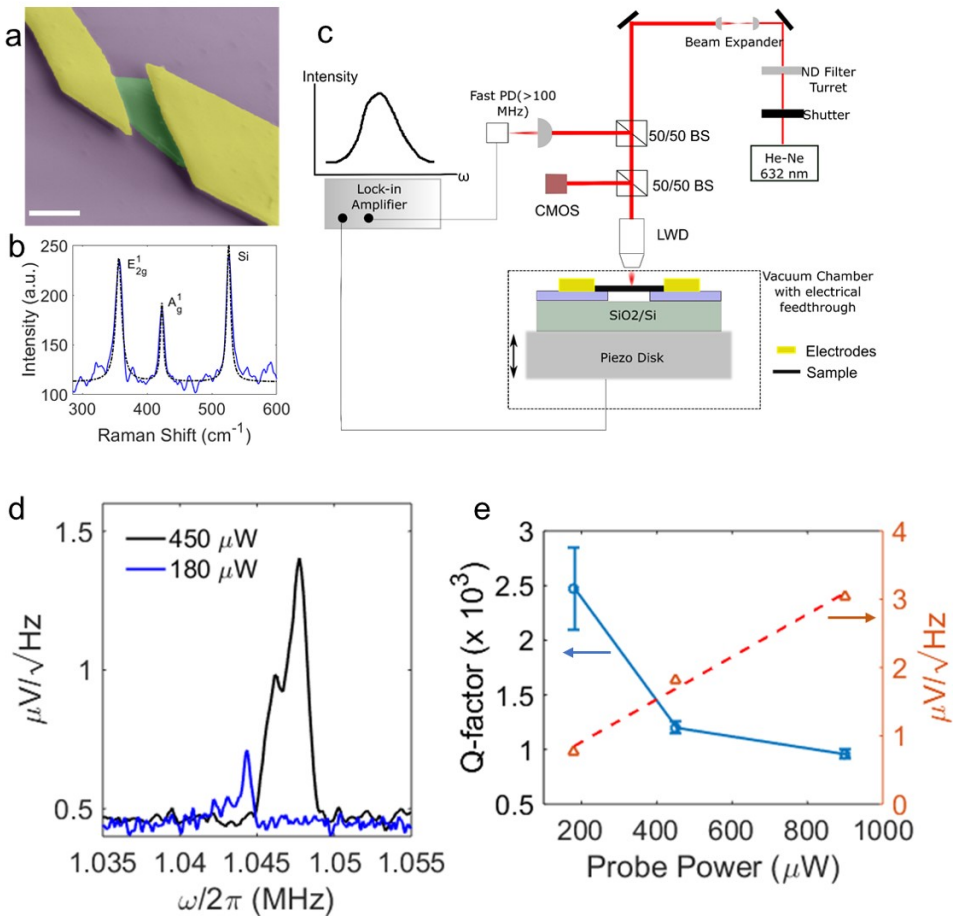

Figure 3.1. Sample fabrication, Raman spectroscopic characterization, cavity-interferometry setup and measurement of thermo-mechanical resonance spectra. a) A pseudo-colored SEM image of the monolayer WS_2 nanoresonator that is clamped on two edges using gold electrodes (scale bar: 10 μm). b) Raman spectroscopy data (blue, solid line) is fit to a multi-peak, Lorentzian line-shape (black, dashed line) to identify the peak locations of different phonon modes. c) A schematic of the experimental setup. A He-Ne laser is used as the probe beam and a piezo disk is used to actuate the nanoresonator. The sample is housed in high vacuum conditions ($<10^{-5}$ Torr). Different abbreviations- BS: Beam Splitter, PD: Photodiode, ND: Neutral Density, LWD: Long Working Distance. d) The thermo-mechanical resonance spectra of modes 1, 2 at different probe powers. e) The Q-factor is lowered with increasing probe power (left axis). The peak-signal intensity is plotted for different probe powers and fit to a straight line (right axis). Data shown are for mode 2.

value of prestress may partially be attributed to the wet-processes in the fabrication workflow as opposed to a purely dry-transfer protocol [82, 92]. From the modal analysis for $\sigma_0 \approx 45$ μN/m, the predicted frequencies for modes 2 and higher do not line up with the observed values (see Figure B.5b in Supplementary Information). A brief comment is made on the possible reason for this discrepancy. Previous reports on few-layered graphene resonators have shown the possibility of unconventional 'edge-modes' that arise due to an out of plane deformation profile and/or imperfections in the sample [93–95]. Further, because the estimated critical buckling load (N_{xx}) is comparable to the prestress $N_{xx} = \sigma_0/2.5 = 16.74$ μN/m (see Supporting Information B.4), the nanoresonator is susceptible to rippling under a non-homogeneous stress profile. *A priori* knowledge of both the sample topography and the mode-shapes is needed to fully analyze the origin of this discrepancy. The laser spot-size in the experimental setup is comparable to the sample dimension and consequently, we cannot measure the mode-shapes with high spatial resolution.

The driven resonance spectrum of the nanoresonator was measured by sweeping the actuation frequency applied to the PZT disc and recording the voltage on a photodiode with a lock-in amplifier. Unless otherwise specified, the probe power was kept constant at 450 μW in these measurements. The first four resonance modes are shown in Figures 3.2a-b at low actuation drives of 0.75 and $1.5V_{p-p}$. The higher order modes (greater than mode 4) had poor SNR at these low actuation drives but were detectable at $2V_{p-p}$ and larger driving voltages. Spurious resonances that arise from the motion of the PZT disc were eliminated by measuring the out of plane motion of the adjacent gold electrodes (see Supporting Information B.5). Resonances that overlapped in both measurements were

categorized as spurious and are not shown. With increasing driving force, mode 1 exhibited the amplitude-frequency effect – i.e., the resonance frequency was strongly dependent on the vibration amplitude (Figure 2.3c). However, the resonance frequency of mode 2 remained stable after initial stiffening (Figure 2.3d). Further, the resonance linewidth increased monotonically with the driving force for both modes, which is indicative of nonlinear damping. Nonlinear damping has previously been reported in low-dimensional NEMS such as carbon nanotubes as well as graphene resonators, although its physical origin is currently unclear [96]. The weakly nonlinear behavior of mode 1 in Figure 2.3c can be understood within the framework of a Duffing resonator, viz.,

$$\frac{d^2x}{dt^2} + (\gamma + \eta x^2)\frac{dx}{dt} + \omega_0^2 x + \alpha x^3 + \beta x^4 + \delta x^5 = \frac{F}{m_e}\cos\omega t \tag{3.1}$$

In equation 3.1 m_e is the effective mass, γ is the linear damping coefficient and ω_0 is the resonance frequency; α, β, δ are the cubic, quartic and quintic order nonlinear coefficients, whereas η is the nonlinear damping parameter. In Figure 3.2c, mode 1 undergoes hardening at intermediate drive voltages followed by softening at higher drives. The quartic and quintic order nonlinear terms are included to account for this mixed type of nonlinear behavior [5, 97]. The measured data were fit to the Duffing model (given in equation 3.1) for mode 1 and to a Lorentzian line-shape for mode 2 to extract the effective linewidth at different actuation voltages (see Supporting Information B.6).

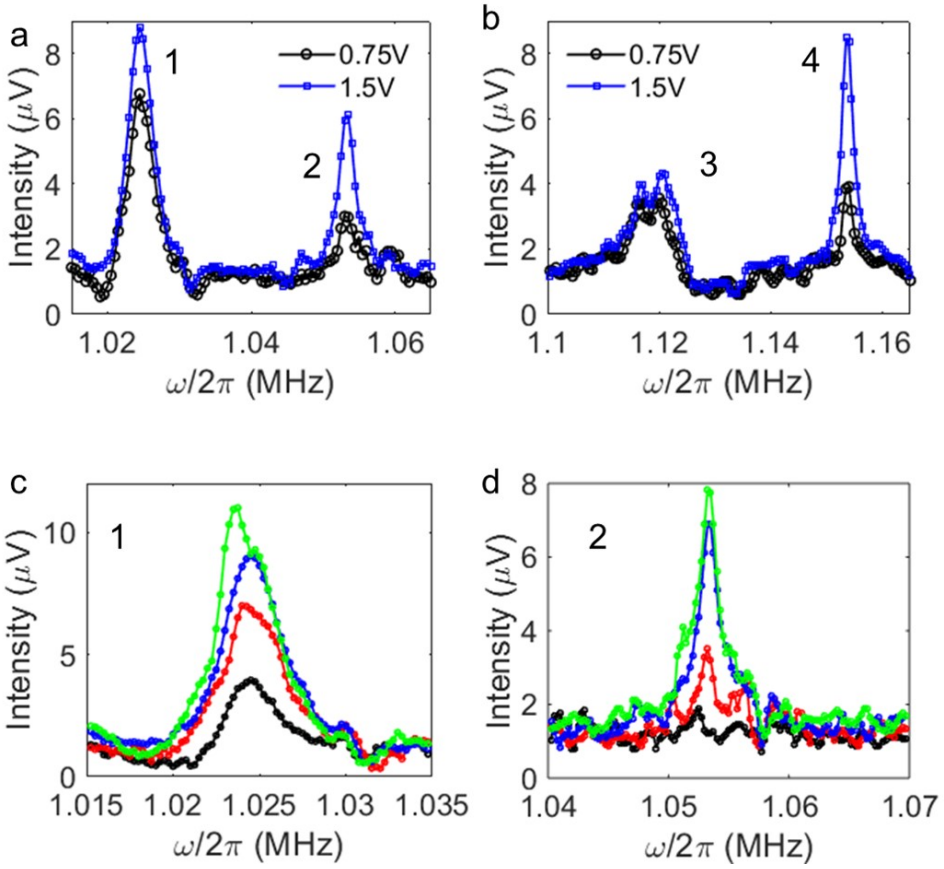

Figure 3.2. Weakly nonlinear behavior in modes 1, 2. The driven resonance spectra at low driving voltages is shown for a) modes 1, 2 and b) modes 3, 4. c) Mode 1 displays a mixed-type Duffing response and nonlinear damping with increasing actuation voltages. d) The effective damping in mode 2 increases with the driving force. In c, d the driving voltages used from bottom to top are 0.5, 0.75, 1.5 and $2.0V_{p-p}$.

3.3. 1:1 Internal Resonance

We investigated mode-coupling due to geometric nonlinearity in modes 1 and 2 by driving them at even higher harmonic forces. When the driving voltage was increased to $3V_{p-p}$, we observed a sudden drop in the peak amplitude of mode 1 along with the appearance of a sideband for mode 2 (Figure 3.3a). This redistribution of energy between

the two modes at a high actuation amplitude suggests that they are coupled. Further, the emergence of a bimodal line-shape for mode 2, which is also referred to as mode-splitting [80] or an M-shaped resonance curve [71] in the literature, with increasing actuation amplitude is a telltale signature of 1:1 internal resonance between the two nearly commensurate modes [68]. At even higher driving voltages, mode 1 becomes bimodal and develops a sideband at a lower frequency (Figure 3.3b, indicated with an arrow). The behavior of mode pairs 3, 4 (Figure 3.3c) and 5, 6 (Figure 3.3d) was qualitatively similar under high driving forces. For instance, we observed a sudden dip in the peak amplitude of modes 3, 4 along with an increase in their bandwidth (see Figure 3.3c) as the driving voltage was increased to $3V_{p-p}$. Mode 6 was bimodal even under low driving forces; as the voltage was increased to $3V_{p-p}$, a drop in the peak amplitude of the higher frequency branch was accompanied by the appearance of a sideband in the lower frequency branch.

The resonant behavior of modes 7, 8 as a function of the actuation amplitude is presented in Figure 3.4. Modes 7, 8 exhibited a bimodal line-shape even at a low driving voltage of $2V_{p-p}$ (Figure 3.4a). Unlike modes 2 and 6 where the two peaks in the bimodal response were well resolved, the line-shape for mode 7 is reminiscent of 1:1 IR in taut strings. In the latter, the overshoot is a consequence of amplitude-modulated motion due to Hopf bifurcation [98]. The phase response for mode 7 is shown in Figure 3.4b. A total phase shift of π in the frequency span between 1.33 and 1.35 MHz ascertains that the line-shape is not due to a super-position of two close-by modes but originates from a single mode. Upon progressively increasing the driving voltage to $6V_{p-p}$, the line-shapes for mode 7 remained similar but with better SNR (Figure 3.4c); whereas for mode 8, the lower frequency portion exhibited softening. Forward and backward swept traces were also

obtained (Figure 3.4d) for modes 7, 8 at $6V_{p-p}$. In addition to the expected hysteresis (for instance, in the softening portion of mode 8), we noticed that the peak amplitude of mode 7 was smaller during the backward sweep.

The frequency response curves presented in Figures 3.3,3.4 are a consequence of 1:1 IR and can be understood using a generalized reduced order model that consists of two Duffing oscillators with nearly commensurate frequencies and weakly non-linear coupling terms, given by the following pair of ordinary differential equations (ODEs), namely

$$\ddot{x} + \omega_1^2 x = \epsilon \left[-\mu_1 \dot{x} + k_1 x^3 + a_1 x^2 y + b_1 x y^2 + c_1 y^3 + d_1 y + F \cos \omega t \right] \tag{3.2}$$

$$\ddot{y} + \omega_2^2 y = \epsilon \left[-\mu_2 \dot{x} + k_2 x^3 + a_2 x^2 y + b_2 x y^2 + c_2 y^3 + d_2 y \right] \tag{3.3}$$

In equations 3.2-3.3, x and y refer to the modal degrees of freedom, ϵ is a small parameter. The forcing term (F) is present in only one of the oscillators as it corresponds directly to the experimental situation; however, because of the nature of 1:1 IR, the other mode is automatically excited through the coupling terms. This contrasts with pump-probe experiments, where an additional excitation source (the pump signal) is applied to one of the modes while its effect on the probe mode is measured. The RO model was derived starting from the Foppl-von Karman plate theory, which accounts for geometric nonlinearity (see ref. [67, 68]). Using modal expansion composed of only two modes, followed by a Galerkin procedure, it can be shown that the governing partial differential equations reduce to the nonlinear ODEs given in equations 3.2-3.3 (refs. [67, 68]). The coefficients in the ODEs are related to the mode-shapes and their derivatives; and in those cases where the mode-shapes are known accurately (e.g., circular or square resonator with

all boundaries clamped), the experimental observations can be quantitatively explained using the RO model [5, 76, 100]. Similar models have been studied previously, with slight variations, for the case of 1:1 IR [101] and 1:3 IR [102]. Depending on the nonlinear terms that are retained, the RO model can lead to a diverse set of frequency-response curves such as those shown in Figure 3.3 [102].

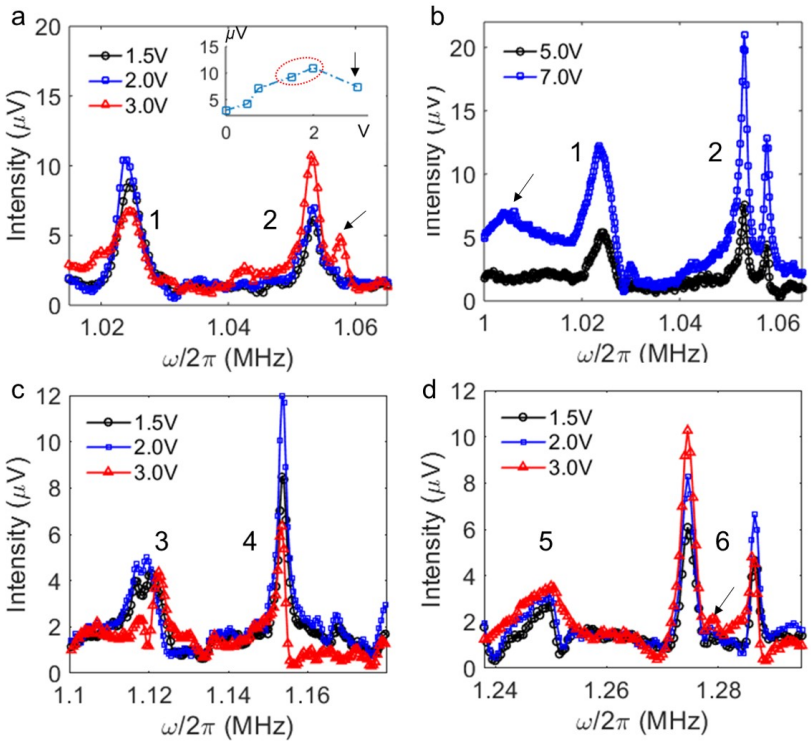

Figure 3.3. Nonlinear behavior at high drive forces is mediated by 1:1 IR. a-b) The evolution of nonlinearity in modes 1, 2 is presented for increasing driving voltages. At $3V_{p-p}$, there is a redistribution of energy between modes 1, 2. The bimodal response of mode 2 suggests 1:1 IR. At a higher driving voltage of $7V_{p-p}$, mode 1 develops a sideband at a lower frequency. Inset in a) plots the peak intensity (μV) vs the driving voltage (V) for mode 1. The linear behavior at low voltages is transformed into amplitude saturation at intermediate voltages (red, dashed ellipse), followed by a drop in the intensity at a driving voltage of $3V_{p-p}$ (arrow). c) Mode pairs 3, 4 and d) 5, 6 showed similar behavior with increasing excitation force. Sidebands that appear with increasing drive forces are shown with arrows

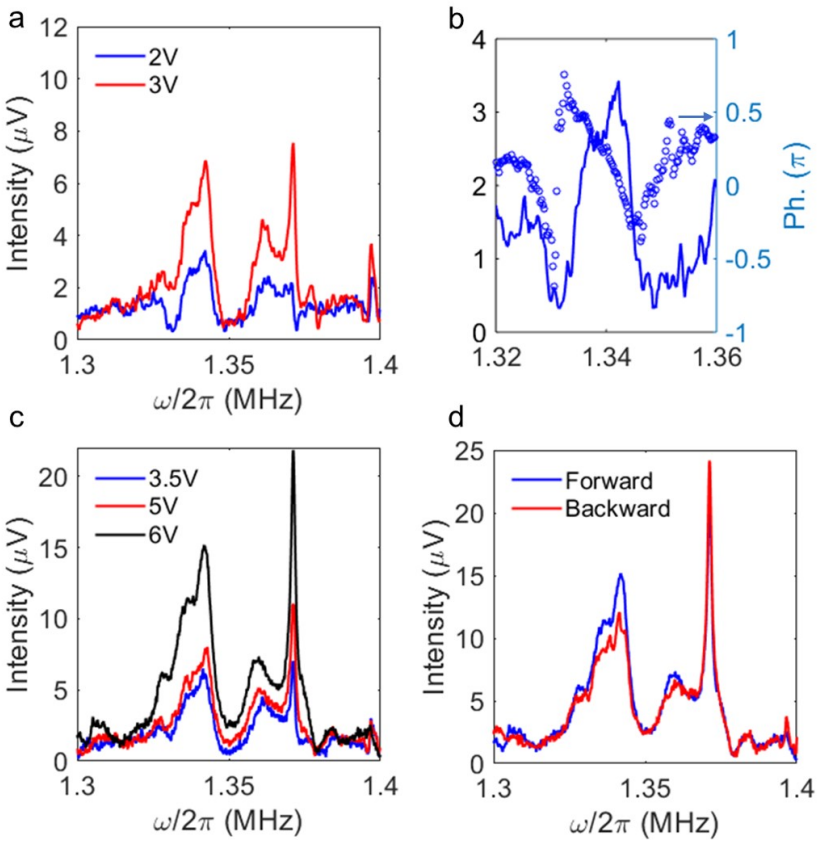

Figure 3.4. Nonlinear behavior of modes 7, 8. a) Resonance spectra obtained under moderate forces – the modes 7 ($\omega_c/2\pi \approx 1.34$ MHz) and 8 ($\omega_c/2\pi \approx 1.37$ MHz) exhibit a non-Lorentzian line-shape due to 1:1 IR. b) The line-shape arises from a single mode as confirmed by a total phase change of π (data shown for the case of $2V_{p-p}$). c) Resonance spectra of modes 7, 8 at higher actuation amplitudes. d) Forward and backward sweeps show amplitude modulations of unequal amplitude in mode 7 and softening-type hysteresis in mode 8.

3.4. Bifurcation Analysis

We performed bifurcation analysis (using MatCont, ref. [103]) on a simplified version of the RO model (given below) to explain the unconventional line-shape of mode 7.

$$\ddot{x} + \omega_1^2 x = \epsilon\left[-\mu_1\dot{x} - k_1x^3 - \Lambda xy^2 + F\cos\omega t\right] \tag{3.4}$$

$$\ddot{y} + \omega_2^2 y = \epsilon\left[-\mu_2\dot{x} - k_2y^3 - \Lambda x^2y\right] \tag{3.5}$$

The nonlinear coupling terms were restricted to x^2y^2 in the Hamiltonian, and the coupling strength Λ was used as a fitting parameter. Mode specific parameters such as the linearized frequency ω_i and cubic nonlinearity term k_i were estimated using data obtained with low driving forces and the linear damping parameters were assumed to be equal, i.e., $\mu_1 = \mu_2 = \mu$. The book-keeping parameter was taken as $\epsilon \approx Q^{-1}$. For simplicity, nonlinear damping terms were not included in the analysis. The different values used in the bifurcation analysis are listed in Table B.2 in Supplementary Information B.7. The method of scales was employed (see refs. [67, 68]) to reduce the second order ODEs to the following set of first order ODEs in (p_1,q_1,p_2,q_2) space, namely,

$$\begin{aligned}
p_1^{'} &= -\mu p_1 - \sigma q_1 + \frac{3k_1}{8\omega_1}(p_1^2+q_1^2)q_1 + \frac{\Lambda}{8\omega_1}\left[2(p_2^2+q_2^2)q_1 - (p_2^2-q_2^2)q_1 + 2p_1p_2q_2\right] \\
q_1^{'} &= -\mu q_1 + \sigma p_1 - \frac{3k_1}{8\omega_1}(p_1^2+q_1^2)p_1 + \frac{F}{2\omega_1} - \frac{\Lambda}{8\omega_1}\left[2(p_2^2+q_2^2)p_1 + (p_2^2-q_2^2)p_1 + 2p_2q_1q_2\right] \\
p_2^{'} &= -\mu p_2 - (\sigma-\sigma_1)q_2 + \frac{3k_2}{8\omega_2}(p_2^2+q_2^2)q_2 + \frac{\Lambda}{8\omega_2}\left[2(p_1^2+q_1^2)q_2 - (p_1^2-q_1^2)q_2 + 2p_1p_2q_1\right] \\
q_2^{'} &= -\mu q_2 + (\sigma-\sigma_1)p_2 - \frac{3k_2}{8\omega_2}(p_2^2+q_2^2)p_2 - \frac{\Lambda}{8\omega_2}\left[2(p_1^2+q_1^2)p_2 + (p_1^2-q_1^2)p_2 + 2p_1q_1q_2\right]
\end{aligned}$$

The parameters (p_1, q_1) and (p_2, q_2) are related to the slowly varying amplitudes A, B of the two oscillators by $A = \frac{1}{2}(p_1 - q_1)e^{i\phi_1}$ and $B = \frac{1}{2}(p_2 - q_2)e^{i\phi_2}$. The closeness of

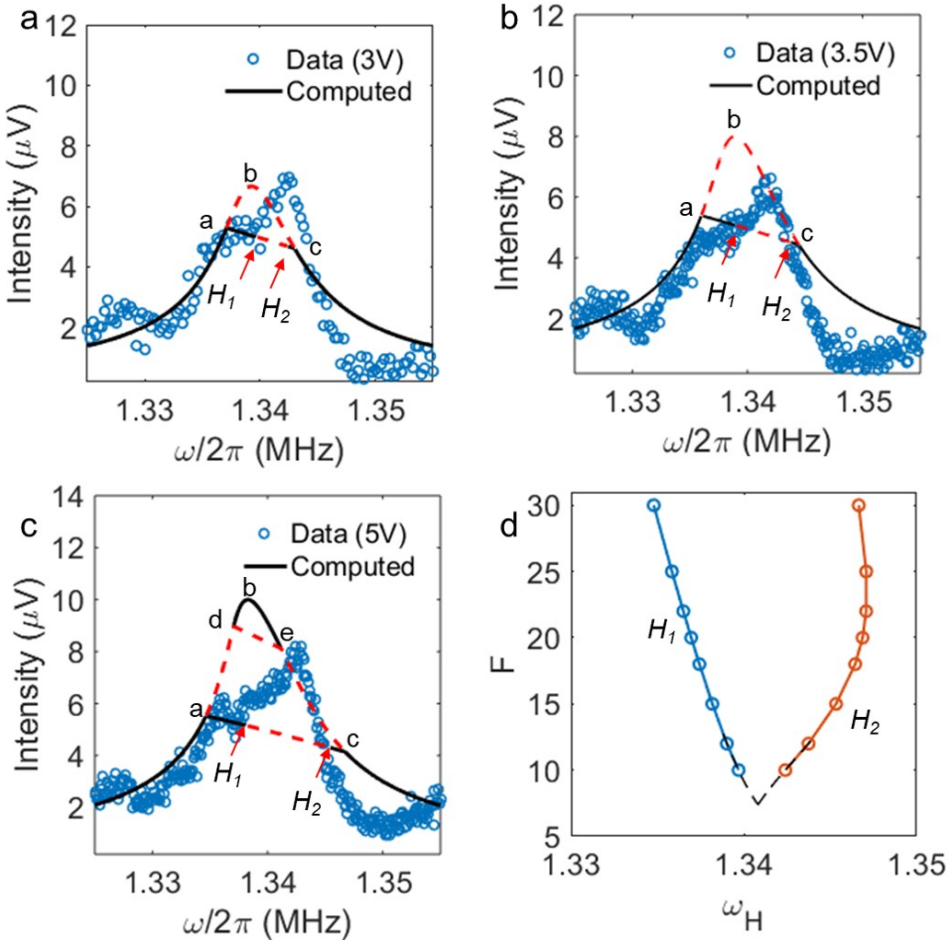

Figure 3.5. Bifurcation analysis predicts Hopf bifurcations for mode 7. a) The frequency-response curve obtained from the bifurcation analysis is overlaid on the measured data at $3V_{p-p}$. The stable regions are indicated using solid lines, unstable regions using dashed lines and Hopf bifurcation points (H_1 and H_2) using arrows. The computed frequency response curves at increasing drive forces are shown in b) and c) along with the measured data at 3.5 and $5.0V_{p-p}$. d) A bifurcation set is shown with the two Hopf points; the computed curves were extrapolated to lower values of F to identify the critical value below which the Hopf points vanished

the two frequencies is expressed using a detuning parameter σ_1, where $\omega_2 = \omega_1 + \epsilon\sigma_1$. A different detuning parameter denotes the closeness of the excitation frequency to the primary resonance frequency ω_1 by $\omega = \omega_1 + \epsilon\sigma$.

Figure 3.5a shows the computed frequency response diagram for mode 7 along with the measured data for $3V_{p-p}$. The unstable regions in the diagram are shown using dashed lines, whereas the stable regions are shown using solid lines. Points a and c refer to branch points on the diagram, from which additional fixed points could emerge. H_1 and H_2 refer to Hopf bifurcation points along the new branch curve connecting points a, c. The computed frequency response curve differs from the Lorentzian line-shape in two aspects: 1) it loses stability along the portion of the curve that connects points a, b and c; and 2) Hopf bifurcations occur along the new branch curve. To see how the experimentally observed line-shape can be explained using the computed diagram, consider a forward sweep. The oscillator moves along the stable branch until it arrives at point a, where there is a bifurcation which causes it to traverse the new branch curve until it reaches the first Hopf point H_1. According to the Hopf-bifurcation theorem, the motion now is no longer periodic but amplitude-modulated, which in experiments causes an overshoot from the predicted diagram until it reaches point H_2 [68]. The oscillator then follows the stable branch after traversing the second Hopf-bifurcation point H_2. Frequency response curves were also computed for increasing forces, as shown in Figures 3.5b, c along with the measured data, showing good agreement between the two. The distance between the Hopf bifurcation points increases with the driving force, indicating that amplitude-modulated motion occurs over a wider frequency range. Figure 3.5d shows a bifurcation set for the coupled system, where at a sufficiently low driving force, both Hopf bifurcation points are predicted to disappear.

MatCont automatically computes the first Lyapunov coefficient for Hopf bifurcation points which can be used to classify them as either sub or super-critical. Because the

first Lyapunov coefficient is positive for H_1, it is a sub-critical Hopf bifurcation and may lead to an unstable limit cycle and eventual chaotic motion. However, because the first Lyapunov coefficient is negative for point H_2, it is a super-critical Hopf bifurcation, and is characterized by a stable, limit cycle. This prediction is reflected in the difference between the forward and backward swept data that are shown in Figure 3.4d. The forward swept trace first passes through the sub-critical Hopf bifurcation and consequently, the peak amplitude is higher when compared to the backward swept trace (which passes through the super-critical Hopf bifurcation first).

3.5. Applications

The location of the sub-critical Hopf bifurcation point H_1 varies linearly with the force magnitude F and therefore, it could serve as a simple scheme for the detection of weak forces. The super-critical Hopf bifurcation point H_2 has a linear dependence for intermediate force values and plateaus subsequently. As per the bifurcation diagram in Figure 3.5d, the limit of detection corresponds to the value of the driving force where the Hopf bifurcations disappear. As discussed in Supplementary Information B.7, the actuation force on the nanoresonator results from inertial coupling with the motion of the PZT disc and is given by $F = Tm_r\omega^2 d_0$, where m_r is the mass of the nanoresonator, T is the transmission coefficient and d_0 is the peak amplitude of the disc. Assuming ideal transmissivity (i.e. $T = 1$), and the following parameter values: linearized frequency $\omega_0/2\pi \approx 1.34$ MHz, $m_r = 10$ fg, peak amplitude $d_0 = d_{33}V_{lim}$, where $d_{33} = 330$ pm/V is the piezoelectric coefficient of the PZT disc and $V_{lim} = 1.5$V is the driving voltage at which the Hopf bifurcation points disappear, the lowest detectable force can be estimated

as $F_{min} \approx 350$ fN. The sensitivity in the current implementation is limited by the fact that the force of interest is also responsible for driving the resonator into the nonlinear regime, and consequently the bifurcation points disappear at low force magnitudes. Thus, the limit of detection could be further improved by ensuring that the resonator is in the nonlinear regime even without the force of interest – for e.g. by employing parametric amplification [104, 105]. In parametric amplification, the response of an oscillator can be amplified by applying a pump signal at twice the linear resonant frequency, $\omega_p \approx 2\omega_0$, namely

$$\frac{d^2x}{dt^2} + (\gamma + \eta x^2)\frac{dx}{dt} + \omega_0^2 x(1 - \lambda \cos \omega_p t) = \frac{F}{m_e} \cos \omega t \tag{3.6}$$

In equation 3.6, λ denotes the amplitude of the parametric drive. When the drive amplitude is increased beyond a certain critical value λ_c, the resonator enters the regime of self-oscillations, even in the absence of a driving force. Such regime can be realized in TMDC resonators using capacitive actuation of the back gate (see ref. [106]). Further, under parametric amplification, TMDC resonators enter the nonlinear regime at relatively small RF voltages (-20 dBm). To quantify the improvement in sensitivity with parametric amplification, we consider a force as resolvable if the effected change in the bifurcation frequency is greater than intrinsic fluctuations (δf) in the frequency [105], i.e. $\kappa F_{min} \geq \delta f$, where κ is the slope of the bifurcation frequency vs force curve (units of Hz/N). By assuming an extremely conservative value of $\delta f = 50$ Hz (for an integration time of 1 s, ref. [2]), and extracting $\kappa \approx 10^{17}$ Hz/N from the bifurcation diagram for Hopf bifurcation point H_2, we estimate $F_{min} = 500$ aN. Taken together, the estimates indicate

that force sensitivity in the nonlinear regime can be significantly improved with parametric amplification. We would like to emphasize that this improvement in force sensitivity with a parametric drive is possible only in the nonlinear regime; in the linear regime of operation, a parametric drive would equally amplify both the resonator displacement as well as the thermal noise force, resulting in no net improvement [104].

3.6. Summary and Future Work

The force sensitivity of a nano-mechanical resonator is limited by the thermal force noise $S_f = 4k_bTm_e\gamma B$, where k_b is the Boltzmann constant, B is the measurement bandwidth, T, m_e, γ are the temperature, effective mass and linewidth of the resonance. Because of their low mass and narrow linewidth, by employing low dimensional materials – such as nanowires, nanotubes and two dimensional (2D) materials – at cryogenic temperatures is an attractive strategy towards the design of resonators with high force sensitivity. However, realizing the thermal force limit in these systems is challenging as it requires a transduction scheme that can efficiently convert small displacements into a measurable signal [92]. Consequently, their performance is often limited by noise in the transduction scheme [107, 108]. In this chapter, an alternative but unexplored approach to force sensing has been demonstrated, where the key idea is to operate the resonator in the nonlinear regime and utilize the sensitivity of bifurcation points to an external force. Such an approach to force sensing is advantageous due to multiple reasons. Firstly, the method relaxes the requirement of a narrow measurement bandwidth as nonlinear responses offer a higher signal to noise ratio and are relatively simpler to measure. Secondly, theoretical estimates suggest that a force sensitivity in the attoNewton range can be achieved at

room temperature [105]. Lastly, the shorter integration times may enable the detection of weak, incoherent forces and force jumps.

The qualitative implications from the results presented here on the nonlinear behavior of 2D WS_2 are rather general and in line with prior experimental and numerical studies. In macroscale plates, the strongly nonlinear behavior transitions from weakly nonlinear to eventual chaos via energy exchanges between internally resonant modes. The exact nature of internal resonance (i.e., 1:1 or 1:2 etc.) depends on the energy of vibration and imperfections in the plate [109]. The wide frequency tunability (>10, using optical or electrostatic means) in 2D nanoresonators should allow three mode alignment and the engineering of more complex internal resonance phenomena (e.g., 1:1:2 or 1:1:3), which are interesting from a fundamental viewpoint. We also note that the force sensitivity of nonlinear- 2D nanoresonators can be further enhanced by increasing the sensitivity of the bifurcation points to the applied force (κ). A first step in this direction would be a systematic analysis of different kinds of internal resonance in well-defined geometries (square or circular, with all boundaries clamped) and the bifurcation points therein. Because the mode shapes agree with theory in these regular geometries, a major advantage is that the coefficients in the RO model can be determined exactly. An order of magnitude improvement in κ would lead to a force sensitivity that is comparable with the best room temperature force sensors (see Figure 3.6).

A hitherto unexplored application of nonlinear mode-coupling in 2D nanoresonators is the synchronization of the coupled modes [71]. The major advantages of using 2D materials, vis-à-vis micro-machined Si-based resonators are a) the coupled oscillators can be realized in the same resonator (the coupled modes shown in Figure 3.3, for instance),

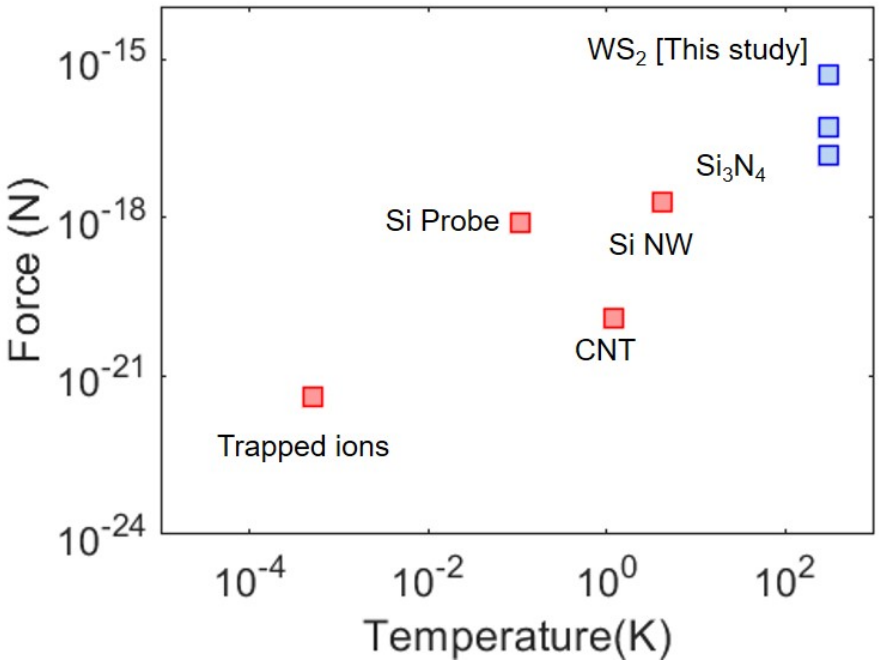

Figure 3.6. Comparison of force sensitivities in commonly employed nanomechanical resonators as a function of temperature and material. Trapped ions ([110]), Carbon Nanotube (CNT, [111]), Si Probe ([112]), Si Nanowire (NW, [113]), Si_3N_4 ([114]), Theory ([105]).

avoiding the need for complex fabrication, b) the widely tunable resonant frequencies and geometric nonlinearity can be exploited to increase the synchronization range, and c) the high-frequencies involved facilitate signal processing applications in the RF region. Further, synchronization would in turn reduce the phase noise and improve the frequency stability in 2D nanoresonators [115].

TMDCs are characterized by reduced phonon-phonon scattering [11, 83, 86] , negligible spectral broadening [116] and thus, are better suited to resonator studies than graphene and other commonly employed 2D materials. The results presented here provide a path

forward towards the utilization of nonlinearity for force and mass sensing as well as the synchronization of internally resonant modes in TMDC nanoresonators.

3.7. Acknowledgments

I'd like to thank Siyan Dong for his painstaking efforts in fabricating the sample and to Dr. Lior Medina for developing the governing equations of a plate with geometric nonlinearity. The work was generously funded by the Army Research Office (ARO) through Grant No. W911NF1510068. I am extremely grateful to Dr. Sridhar Krishnaswamy and Dr. Oluwaseyi Balogun from Northwestern University for valuable discussions. Support is acknowledged from the Center for Nanoscale Materials (CNM, Argonne National Lab), an Office of Science user facility, supported by the U.S. Department of Energy, Office of Science, Office of Basic Energy Sciences, under Contract No. DE-AC02-06CH11357. This work also utilized Northwestern University Micro/Nano Fabrication Facility (NUFAB), which is partially supported by Soft and Hybrid Nanotechnology Experimental (SHyNE) Resource (NSF ECCS-1542205), the Materials Research Science and Engineering Center (NSF DMR-1720139), the State of Illinois, and Northwestern University.

CHAPTER 4

Localized Electroporation for Single-Cell Analysis

I am all pervasive. I am without any attributes, and without any form. I have neither attachment to the world, nor to liberation. I have no wishes for anything because I am everything, everywhere, every time, always in equilibrium. I am indeed, That eternal knowing and bliss, Shiva, love and pure consciousness.

Nirvāna Shatkam by Ādi Shankara

4.1. Background

The ability to monitor internal cellular biomarkers at different time points and measure their changes over time is key to understanding the fundamental mechanisms governing dynamic cellular processes such as differentiation, maturation and ageing [117, 118]. Temporal measurement of intracellular contents at the single-cell level can provide insights into the involved regulatory pathways and help understand the pathophysiology of disorders such as Alzheimer's and Parkinson's as well as the efficacy of drugs and their possible toxic effects [119, 120].

Current high-throughput single-cell technologies for genomic, transcriptomic and proteomic analysis combine microfluidic platforms such as droplets, valves and nanowells with high sensitivity assays such as single-cell western blot, protein barcodes, antibody spots and RNA sequencing [121–127]. These methods rely exclusively on cell lysis, and thus provide only a single snapshot of cellular activity in time. Using these lysis based

methods, pseudo-time histories can be constructed with information obtained from parallel cultures [128]. The caveat to this approach is that cellular heterogeneity can mask the true temporal variations in biomarker levels. A commonly used technique of temporal investigation of the same cells involves the use of molecular probes (nanostars, molecular beacons and fluorescent biosensors) to tag molecules of interest in live cells [129–133]. However, the number of intracellular targets that can be studied simultaneously and the possibility of cellular perturbation caused by these intracellular labels limit the utility of these methods. Another approach for temporal analyses, which is limited to a sub-set of cellular proteins, uses microfluidic platforms to profile and record secreted proteins across a timespan [134]. Recent approaches have also used nanoprobes such as carbon nanotubes, AFM tips and nanopipettes to extract single-cell cytosolic content for subsequent assays [135–137]. These methods however, are serial and lack the throughput required for systems biology analyses.

Micro and nano-scale electroporation technologies present promising approaches towards temporal sampling from live single-cells. These techniques offer significant advantages over traditional bulk electroporation methods for the delivery of small molecules, proteins and nucleic acids of interest into cells [138, 139]. The applied electric fields in these techniques are gentle to the cells and often perturb a very small fraction of the cell membrane. Two major advantages that these localized electroporation methods offer are the preservation of cell viability and functionality and the ability to target single-cells for delivery and subsequent monitoring [140, 141]. As such, electroporation at the micro and nano-scale has been used to address the converse problem, i.e. to non-destructively sample cytosolic contents from populations of cells [142, 143]. Although proof of concept

demonstrations have shown the potential of these methods, there are major challenges that need to be overcome. One technological challenge that inhibits the realization of single-cell temporal sampling is the necessity of high precision microfluidic systems coupled to high sensitivity assays that can handle, transport and detect subcellular amounts of analytes in picoliter volumes, without incurring substantial losses. Another major hurdle is the lack of a mechanistic understanding of the process of localized electroporation and molecular transport out of the cell during sampling.

To improve our understanding of the process of localized electroporation and molecular transport, we have developed a multiphysics model incorporating the dynamics of pore formation on the cell membrane in response to a non-uniform and localized electric field; and the subsequent transport of molecules of interest into or out of the cells through these membrane pores. We have validated the model by quantifying the delivery and sampling of proteins in a small cell population using the so-called Localized Electroporation Device (LEPD) [144] – a microfluidic device developed by the Espinosa group for the culture and localized electroporation of adherent cells. The experimental trends corroborate with the model predictions and together they provide regimes of operation in the applied pulse strength and frequency, which are ideal for efficient delivery and sampling without compromising cell viability. The results also provide general guidelines regarding optimization of pulse parameters and device design applicable to localized electroporation mediated delivery and sampling. These guidelines lay down the foundations necessary to achieve the goal of single-cell temporal sampling.

4.2. A Multi-physics Model for Localized Electroporation

4.2.1. Device Architecture and Operation

The LEPD architecture allows for the long-term culture and localized electroporation of adherent cells. The cells are cultured on a polycarbonate substrate with multiple nanochannels that is sandwiched between a PDMS micro-well layer and a delivery/sampling chamber (see Figure 4.1a and Figure 4.1b). This chamber can serve the dual purpose of retaining the molecular cargo to be delivered into the cells or collecting the intracellular molecules that leak out from the cell during the process of electroporation. The extracted cytosolic content then can be retrieved for downstream analyses. The substrate material and nanochannel density can be varied according to experimental requirements. When an electric field is applied across the LEPD, the nanochannels in the substrate confine the electric field to a small fraction of the cell membrane and minimize perturbations to the cell state. Thus, this architecture can be used to transfect and culture sensitive cells (such as primary cells) while preserving a high degree of cell-viability. The Espinosa group has previously demonstrated on-chip differentiation of murine neural stem cells and transfection of postmitotic neurons on the LEPD platform [144]. In the current work, the LEPD has been extended to sampling an exogenous protein in a small population of engineered cells. All of the experimental data and computational analyses presented here were acquired using the LEPD architecture.

4.2.2. Model Description

The application of pulsed electric fields leads to the transient permeabilization of the cell membrane, allowing both influx and outflux of molecules of varying sizes [145–147].

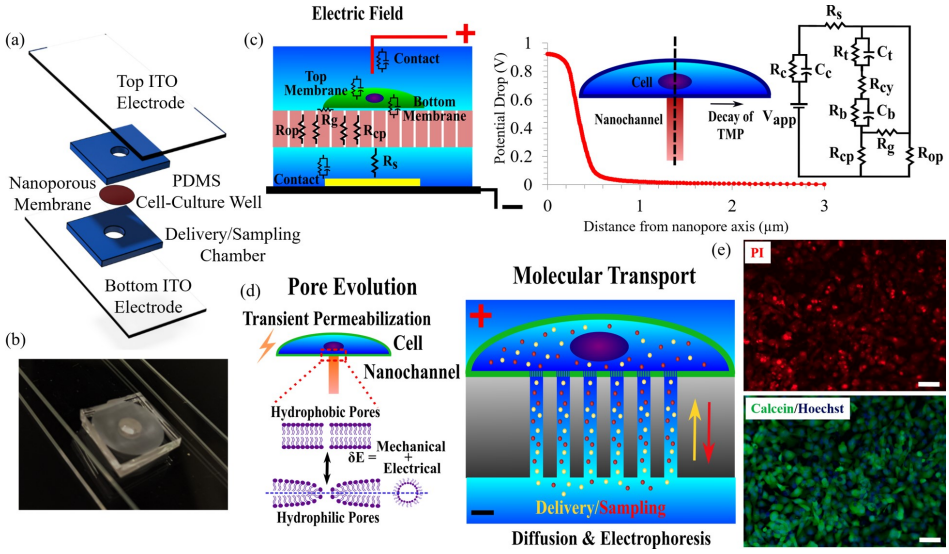

Figure 4.1. Overview of the experimental and computational framework. (a) Schematic of the Localized Electroporation Device (LEPD) showing the different constituent layers, (b) Optical image of LEPD consisting of the PDMS device sandwiched between two ITO electrodes, (c) Left – Schematic of the concept of localized electroporation and the components that can be used to describe the electric field distribution. The transmembrane potential (TMP) is obtained by solving the electric field equations. Right – Axisymmetric FEM simulation of the electric field with a single nanochannel underneath a cell shows that the transmembrane potential drop is confined to the region of the nanochannel for localized electroporation. Consequently, a lumped circuit model can be used to represent a system with many nanochannels in parallel underneath a cell, (d) Left – Schematic of the pore evolution model. Transient permeabilization of the plasma membrane leads to the formation of hydrophilic pores that allow the passage of molecules. The size distribution of pores formed in response to an elevated TMP is obtained by solving a non-linear advection-diffusion equation. Right – Schematic of the molecular transport model. The transport across the permeabilized membrane is primarily diffusive and electrophoretic, (e) Delivery of PI into HT 1080 cells on the LEPD platform under iso-osmolar conditions using a 10 V pulse. Top image shows a delivery efficiency of $>$ 95%. Bottom image shows viability of $>$95% using live dead staining, 6 hours post electroporation (Scale bars = 50 μm).

The most widely reported mechanism underlying this phenomenon assumes the formation of hydrophilic toroidal pores in the phospholipid bilayer [148, 149]. The formation, evolution and destruction of these 'electro-pores' is governed by the Smoluchowski advection-diffusion equation, which is derived using a statistical mechanics framework [150]. Assuming the molecular transport through these membrane electro-pores to be primarily diffusive and electrophoretic, this framework has been utilized to provide estimates of small molecule delivery in bulk electroporation [151]. Although this model simplifies certain chemical and mechanical aspects of the permeabilization process [152, 153], it correlates reasonably well with experimental observations of electropores [154, 155], molecular dynamics simulations [156] and molecular transport [151]. Here we extend this model to the case of localized electroporation where a spatially focused electric field is utilized to permeabilize only a small fraction of the cell membrane and deliver or extract molecules of interest. Specifically, we investigate the following mechanistic aspects of localized electroporation mediated transport: 1) The role of cell membrane tension in enhancing molecular transport; 2) The dependence of molecular transport (in both delivery and sampling) on the strength of the applied electric field; 3) The differences in delivery efficiency depending on molecular size. In the subsequent sections, we first discuss the implementation of the model followed by the results obtained.

4.2.2.1. Transmembrane Potential. Unlike bulk-electroporation where the electric field is maximum at the poles facing the electrodes and decays away from them [157, 158], the electric field in localized electroporation is focused near the nanochannels and drops rapidly outside of them. By solving the electric field distribution (e.g. using the Finite

Element Method), for the case of a cell placed on a substrate with a single nanochannel (radius = 250 nm) underneath, we found that the TMP drops rapidly (to 1/e of the maximum value within 1.5 times the radius of the nanochannel) outside the region where the cell membrane interfaces the nanochannel (see Figure 4.1c). Since the electric field is confined to the region of the nanochannel, the concept can be extended to multiple nanochannels and an equivalent electrical circuit (see Figure 4.1c) can describe the LEPD system. The equivalent circuit model provides the flexibility of incorporating complex geometries, like the LEPD where several substrate nanochannels ($\approx$ 10 to 1000) can interface with a single cell, that are otherwise computationally non-trivial to simulate using a full field model. In the equivalent circuit R_c and C_c are the contact resistance and capacitance at the electrode-buffer interface. R_s includes all the system resistances in series such as the buffer in the device and the external circuit. The top part of the cell membrane not interfacing with the nanochannels on the PC substrate is modeled by the resistive and capacitive elements R_t and C_t. The cell cytoplasm is represented by the resistance R_{cy}. R_b and C_b represent the equivalent resistance and capacitance of the bottom cell membrane fraction interfacing the substrate nanochannels. R_t and R_b are variable resistors as the conductivity (κ) of the cell membrane changes with the formation and evolution of electro-pores (see Supplementary Information C.1). Since the electric field is localized, only the bottom membrane fraction interfacing the nanochannels has been accounted for by these circuit elements. R_g is the leakage resistance between the cells and the nanochannels. R_{cp} and R_{op} represent the equivalent resistance of all the nanochannels covered by the cells and the open nanochannels respectively. A system of

three ODEs, derived using voltage and current conservation laws at each node, can be used to solve for the TMP, viz.

$$\frac{\partial V_c(t)}{\partial t} = n_1 V_{app}(t) + n_2 V_c + n_3(V_t + V_b) \tag{4.1}$$

$$\frac{\partial V_t(t)}{\partial t} = n_4 \left[V_{app}(t) - V_c\right] + n_5 V_t + n_6 V_b \tag{4.2}$$

$$\frac{\partial V_b(t)}{\partial t} = n_7 \left[V_{app}(t) - V_c\right] + n_8 V_t + n_9 V_b \tag{4.3}$$

Here, V_c is the potential drop across the contact, V_t is the TMP across the top cell membrane, V_b is the TMP across the bottom cell membrane and V_m is the applied far-field voltage. Coefficients n_1 to n_9 are functions of the circuit elements (see Supplementary Information Table C.1). The TMP values V_t and V_b are utilized in the pore evolution equation which is discussed next.

4.2.2.2. Pore Evolution. The evolution of electro-pores in bilayer membranes is governed by the Smoluchowski equation:

$$\frac{\partial n(r_p, t)}{\partial t} = D_p \frac{\partial^2 n}{\partial r_p^2} + \frac{D_p}{kT} \frac{\partial}{\partial r_p} \left(n \frac{\partial E(\sigma_e, V_m)}{\partial r_p} \right) \tag{4.4}$$

where, n is the density of electro-pores per unit membrane area between radius r_p and $r_p + dr_p$ at a particular time t. D_p is the pore diffusion coefficient in the pore radius space r_p, kT is the thermal energy and E is the energy difference between a bilayer membrane with and without a hydrophilic electro-pore (see Supplementary Information C.2). This

description accounts for all the electro-pores through a size distribution without tracking the kinetics of each individual electro-pore. The energy E is a function of the effective bilayer membrane tension σ_e and the TMP V_m, which in our system are the values V_t and V_b obtained by solving the equivalent electrical circuit. The effective membrane tension (σ_e) assumes a non-linear form, which allows for the coupling of the electro-pores. The effective membrane tension (σ_e) is a function of the surface tension (σ) of the cell membrane without pores and the pore distribution (n) (Supplementary Information C.2). The pore evolution equation is solved in a one-dimensional radius space with appropriate pore creation and destruction rates (Supplementary Information C.3) as the boundary condition at the minimum pore radius (r_{min}) and a no flux boundary condition at the maximum radius (r_{max}), which represents the largest permissible electro-pore size. The pore evolution is coupled to the electric field by the effective membrane conductivity (κ) and the dynamics of electro-pores depend on the effective membrane tension (σ_e). Briefly, the formation of electro-pores in response to the increased TMP (V_t, V_b) leads to an increase in the effective membrane conductivity (κ), since the electro-pores act as parallel ion-conducting pathways. The conductivity increase results in a drop of the cell membrane resistance represented by the circuit elements R_t and R_b. Consequently, the TMP decreases which arrests the nucleation and expansion of the electro-pores (see Figure 4.2a). The effective membrane tension (σ_e) also drops as a result of the formed electro-pores [149]. The reduction in membrane tension increases the energy required to expand the formed electro-pores, which eventually halts their growth. These interactions control the pore dynamics based on which we calculate the molecular transport across the permeabilized bottom cell membrane.

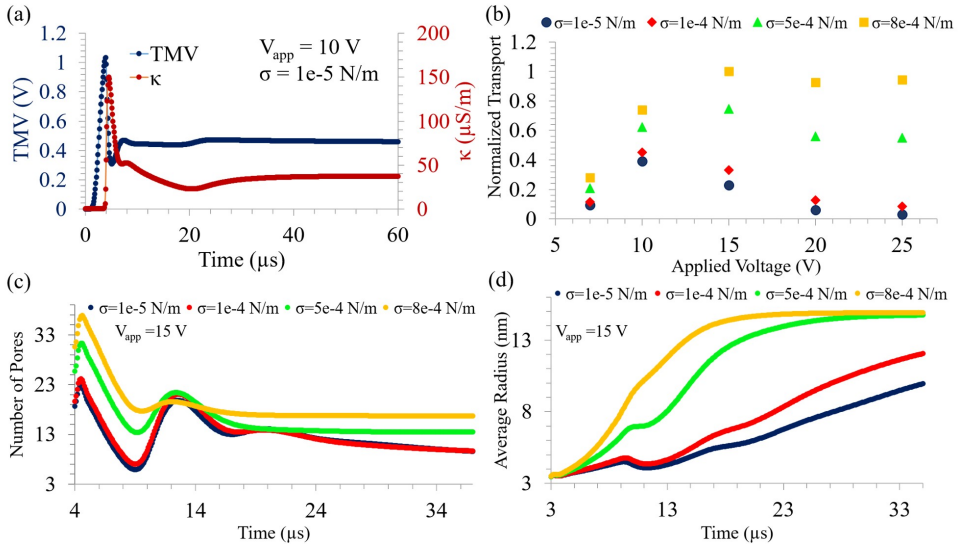

Figure 4.2. Results obtained from numerical simulations. (a) Variation of transmembrane potential (TMP) and cell membrane conductivity (κ) over time for a 10 V applied pulse. The TMP increases in response to the applied pulse which leads to the formation of electro-pores and a consequent increase of κ. This leads to a decrease in the TMP and closure of the electro-pores which decreases κ. Over time a steady value of TMP and κ is reached, (b) The normalized transport (see equation 4.6) is plotted as a function of the applied far-field voltage (V_{app}) and membrane tension (σ). The transport increases as σ is increased. At lower σ, there is an optimal intermediate V_{app} for which the transport is maximum. At higher membrane tensions the transport is more uniform over a wider range of V_{app} , (c) The number of large pores ($>$ 3 nm) formed during the pulsation period is plotted over time for different values of membrane tensions. At higher membrane tension values, the number of large pores formed is increased and they remain open for a longer period, (d) The average radius of large pores ($>$ 3 nm) is plotted over time. The average radius saturates to the largest radius (r_{max}=15 nm) in the simulations quickly for higher membrane tensions. This suggests that larger pores exist for a longer duration when the membrane tension is elevated.

4.2.2.3. Molecular Transport. The molecular flux across the permeabilized cell membrane (see Figure 2.1d) is calculated using the Nernst-Planck equation:

$$J(r_p, t) = -K_p H_p \left[D\nabla c + \frac{Dze}{kT} c \frac{V_m}{d} \right] \tag{4.5}$$

In equation 4.5, J is the flux of molecules across the membrane, K_p and H_p are the partition and hindrance factors respectively [151] (also see Supporting Information C.4), D is the diffusion coefficient of the molecule of interest, c is the local concentration of the molecule, z is the charge on the molecule, e is the elementary charge, kT is the thermal energy, V_m is the TMP and d is the thickness of the cell membrane. For our calculations, we have assumed that the concentration gradient does not change during the pulsation period. The total transported amount (Q) is calculated by integrating the flux through the electro-pores over time for the duration of the applied electric pulse, namely,

$$Q = A_n \int_0^t \int_{r_{mol}}^{r_{max}} J(r_p, t) n\pi r_p^2 dr_p dt \tag{4.6}$$

In equation 4.6, A_n is the total cell membrane area interfacing with the nanochannels and r_{mol} is the radius of the molecule of interest. For simplicity, it is assumed that only pores larger than the hydrodynamic radius of the molecule of interest permit their transport. The values of parameters used in the model are listed in the supplementary section (Supplementary Information Table C.2).

4.3. Model Predictions and Experimental Validation

4.3.1. Effect of Nanochannel Density and Cell Confluency on Electroporation Efficiency

The multiphysics model allowed us to assess the experimental conditions necessary for efficient electroporation on the LEPD platform, which were eventually utilized to validate other model predictions. Specifically, initial model results enabled us to optimize (1) the nanochannel density in the substrate and (2) the cell culture confluency. To numerically investigate the effect of nanochannel density, we fixed the nanochannel diameter at 200 nm and calculated the transport of large molecules (>3 nm) at nanochannel densities of 2×10^6, 3×10^8, and 5×10^8 cm^{-2}, which are commercially available variants. We found that at a higher nanochannel density, the transport is increased (see Supporting Information Figure C.2a). Although increasing the nanochannel density increases the substrate conductivity and reduces the local electric field strength, the area fraction of the substrate available for transport is also increased, which increases the overall transported amount. It should be noted that if the nanochannel density were increased indefinitely, then the electroporation would no longer be localized and would approach the regime of bulk electroporation. Subsequent simulations and experiments on the LEPD were carried out using membranes with 200 nm pores and 5×10^8 cm^{-2} nanochannel density.

We also identified that the cell confluency in the LEPD must be above a threshold such that the TMP is sufficient for electroporation to occur (0.2–1 V) [159]. Using the equivalent circuit model, without incorporating the pore evolution, we calculated the steady-state TMP for applied voltages of 15, 20, and 25 V and varying levels of cell

confluency. The TMP obtained from the equivalent circuit model without pore evolution coupling represents an upper bound as the creation of pores arrests the rise of the TMP. We found that the TMP exceeds the threshold value of 1 V above a confluency of 80% for the applied voltages (see Supporting Information Figure C.2b). Based on these results we maintained the cell confluency in the LEPD at 90% for all the experiments.

4.3.2. Increasing the cell membrane tension enhances molecular transport

Previously, it has been shown that higher membrane tension facilitates electropermeabilization at lower electric field strengths in both lipid bilayers and mammalian cells that were bulk electroporated [160, 161]. The fact that membrane tension plays a critical role in cell membrane permeabilization is also evident from mechano-poration literature where a mechanically induced large deformation enables the permeabilization and subsequent transfection of cells [162, 163]. Naturally, we were interested in understanding the effect of modulating membrane tension in the case of localized electroporation.

We investigated the effect of membrane tension on the molecular transport of large molecules (hydrodynamic radius $>$ 3 nm) in the LEPD system. Our analysis predicts that with an increase in the membrane tension, the transported amount for molecules larger than 3 nm in size increases for all applied voltages within a range (see Figure 4.2b). In our simulations, four different membrane tension values ranging from 10^{-5} N/m to 8 $\times 10^{-4}$ N/m were used. These values are within the range of membrane tensions reported in literature [164]. For each value of membrane tension, far-field voltages ranging from 7 V to 25 V were investigated. Below 7 V, electro-pores that enable the transport of molecules larger than 3 nm were not formed. It is important to note that the membrane

tension referred to in this section is the initial tension for a cell membrane without pores (σ). The simulation results indicate two complementary mechanisms by which an increase in the membrane tension enhances molecular transport. First, the number of large pores per cell (>3 nm) as well as the mean radius of large pores (see Figure 4.2c and Figure 4.2d) increases at higher membrane tensions. In addition, a higher membrane tension stabilizes the large pores during the electric pulse application. This is confirmed by the existence of a greater number of large pores for longer duration during the applied electric pulse (see Figure 4.2c) and the quicker expansion of the pores to the largest radii (15 nm in our model) for high membrane tensions (see Figure 4.2d). Overall, the model results predict that increasing membrane tension can increase the efficiency of molecular transport even in the case of localized electroporation. This has indeed been observed in localized electroporation systems where suction pressure [165] or high aspect ratio nano-structures have been used to efficiently transfect cells [166]. We believe that in addition to reducing the electric field leakage due to imperfect sealing, these methods induce higher tension in the cell membrane, which facilitates efficient molecular delivery according to our analysis.

4.3.3. An optimum voltage exists for maximum molecular transport

Our model also suggests that there is an optimum voltage, especially at lower values of membrane tension (σ) for which the transport of large molecules is maximized (see Figure 4.2b). In the simulations, at a low far-field voltage (7 V), a population of small pores (25 pores) expand to a large size (> 3 nm) and then collapse within 15 μs to smaller radii due to a drop in the TMP and effective membrane tension (σ_e). Only a few large pores (<5 pores) remain open over longer durations. On the other hand, at very high

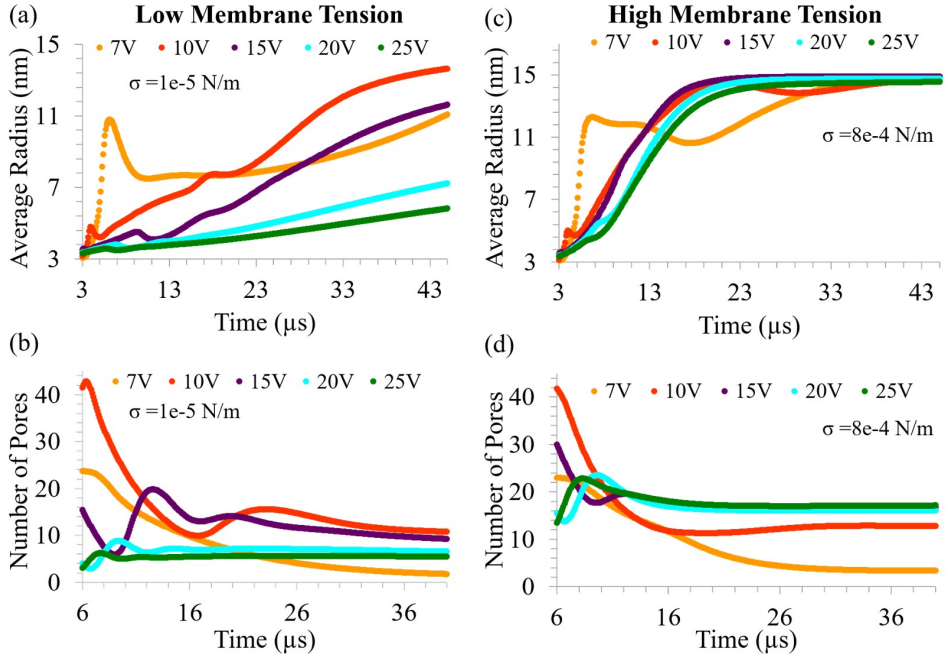

Figure 4.3. **Dependence of pore dynamics on applied voltage.** (a) The average pore radius of large pores (> 3 nm) is plotted over time for different applied voltages (V_{app}) and for a low membrane tension value (1×10^{-5} N/m). It is seen that the average radius is large and is sustained over a longer period for an intermediate voltage of 10 V. At a lower voltage (7 V) the average radius is high initially but drops thereafter. For higher voltages the average radius is lower indicating that the pores do not expand to a large size, (b) Corresponding plot of the number of large pores (> 3 nm) formed over time for low membrane tension (1×10^{-5} N/m). At an intermediate voltage of 10 V, many large pores are formed and sustained for a longer duration, (c) The average pore radius of large pores (> 3 nm) is plotted over time for different applied voltages (V_{app}) for a high membrane tension value (8×10^{-4} N/m). The trend of mean radius is uniform over a range of V_{app} (10 V-25 V), (d) Corresponding plot of the number of large pores (> 3 nm) formed over time for high membrane tension (8×10^{-4} N/m). Similar number of large pores are formed over a range of V_{app} (10 V-25 V).

far-field voltages (20-25 V), several small pores are created that do not expand to larger radii (> 3 nm), thus hindering the transport of large molecules. Less than 10 large pores are observed in these cases. Only at intermediate far-field voltages (10-15 V), sufficient

number of stable large pores (15 pores) are created, which enhances the transport of large molecules (see Figure 4.3a-b). To experimentally verify this prediction, we systematically varied the far-field electroporation voltage from 10 to 40 V and monitored the transfection efficiency of an mCherry encoding plasmid in HT-1080 cells and MDA-MB 231 cells. The pulse width and number were kept constant at 5 ms and 100, respectively. We observed the transfection efficiency to be the highest for a voltage amplitude of 30 V (see Figure 4.4a-b).The transfection efficiency using the LEPD was found to be much higher (mean of 70%) than that using standard lipofection (mean of 15%) (see Supporting Information Figure C.7).At lower voltages of 10 and 20 V, the amount of plasmid delivered was sub-optimal (see Supplementary Figure C.3), as is evident from the lower fluorescence intensity. For a voltage amplitude of 40 V, in addition to weak fluorescence intensity, the cell viability was low and the morphology appeared abnormal.

As a further validation, we investigated how the extracted amount of exogeneous tdTomato protein varied as a function of the voltage amplitude and pulse number in engineered MDA-MB 231 cells. For a voltage amplitude of 30 V, the amount of tdTomato sampled increased with the number of pulses (see Figure 4.5c). On the contrary, when the voltage amplitude was increased to 50 V, the sampling amount was comparable to the 30V, 100 pulses case and independent of the pulse number. The plasmid transfection and tdTomato sampling data taken together highlight the existence of a critical voltage for optimal molecular influx and outflux. We also investigated cell viability on days 1, 2 and 3 post electroporation using live-dead staining. While the cells that were electroporated with a voltage amplitude of 30 V showed healthy morphology, normal cell proliferation and high viability (>99%, see Figure 4.5), most cells electroporated using 50 V had

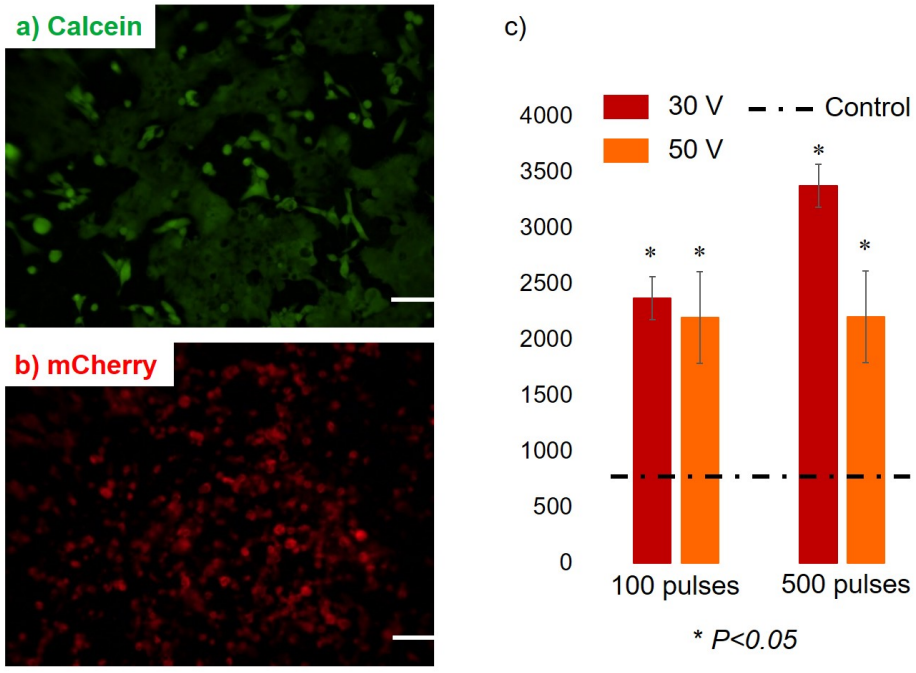

Figure 4.4. **Transfection of mCherry plasmid and tdTomato sampling in MDA-MB 231 cells.** a) Calcein AM stained MDA-MB 231 cells 24 hours post electroporation showing high cell-viability. b) Fluorescence image of mCherry plasmid expression in the cells, 24 hours post electroporation. The optimum voltage amplitude of 30 V was used in these experiments. Scale bars = 50 μm. c) Relative Fluorescence Intensity (y axis) of the sampled tdTomato under various electroporation parameters. Media control is shown as a dotted line. The reported error bars are standard deviation (SD) values from $n = 3$ experiments in each case

detached from the substrate on day 1 itself. (see Supplementary Information Figure C.5). The cells that remained on the substrate showed an unhealthy morphology with blebbing and a spotty tdTomato expression. Similar trends have been observed in the case of bulk electroporation. Experimental demonstrations using bulk electroporation systems have shown that very strong pulses are not conducive to large molecule delivery [167]. Subsequent numerical calculations in the context of bulk electroporation have predicted that beyond a certain critical voltage the pores created are small in size [149].

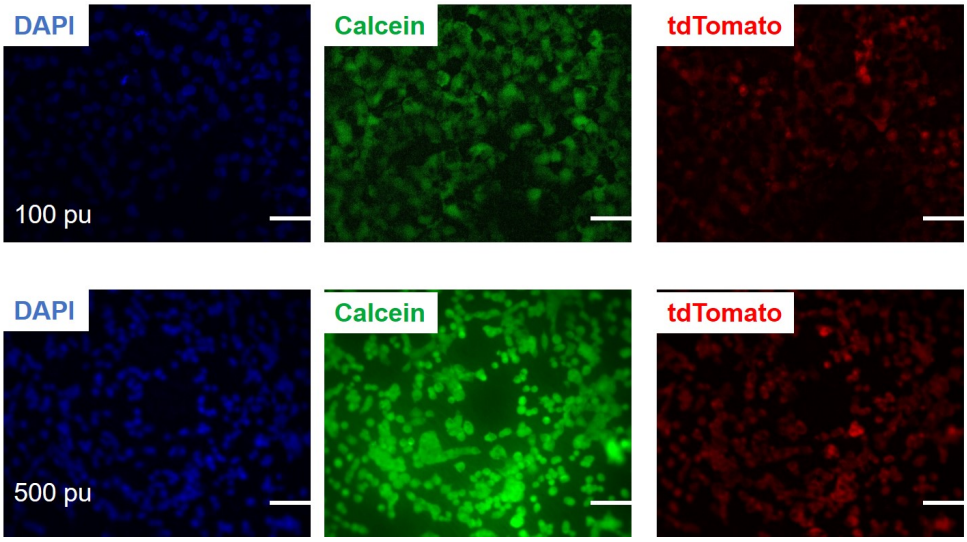

Figure 4.5. **Viability Analysis.** Day 3 viability of cells electroporated with a voltage amplitude of 30 V and 100 pulses (top row), 500 pulses (bottom row). Scale bars = 50 μm.

4.3.4. Molecular transport is uniform over a broader voltage range for higher cell membrane tension

Interestingly, the model predicts that at higher membrane tensions (σ) the molecular transport is uniform over a wider range of applied voltages (see Figure 4.2b). This is a direct result of the fact that at higher membrane tensions the average pore radius and the number of large pores (>3 nm) formed have smaller variability across the applied voltage range (see Figure 4.3c, d). To validate this prediction, we delivered Alexa Fluor 488 conjugated BSA (molecular weight = 66.5 kDa, radius $\approx$ 3nm) into tdTomato expressing MDA-MB 231 cells under both hypo-osmolar (90 mOsmol/kg) and iso-osmolar (280 mOsmol/kg) buffer conditions. Hypo-osmolar conditions increase the membrane tension by inducing osmotic swelling of the cells [160]. The applied voltage was maintained at

30 V for both cases. We found that under hypo-osmolar conditions the fluorescence intensity of delivered BSA was higher and more uniform as compared to the iso-osmolar case (see Figure 4.6a). By plotting the fluorescence signal from 30 cells that were randomly chosen across three biological replicates, we found the mean signal to be higher and the variability across cells to be lower when the hypo-osmolar buffer was used (see Figure 4.2b). It is worth mentioning that without an accurate measurement of membrane tension it is not possible to directly correlate our experimental results to the model predictions. However, the most pertinent inferences from the model are recapitulated in the experiments. In addition, we observed that cells expressing higher tdTomato fluorescence intensity had lower BSA content and vice versa (see Figure 4.2a). This suggests that the process of delivery and sampling from the cytosolic milieu are directly related. Indeed, effectively permeabilized cells on the nanochannel LEPD substrate uptake BSA through the electro-pores but also lose their cytosolic tdTomato to the surrounding media in the process.

It is important to note that although the applied far-field voltage across the LEPD is fixed for a particular experiment, factors such as device architecture, cell shape or size and spatial variation in the applied electric field can lead to variability in the transmembrane potential across individual cells. At a higher membrane tension, the molecular transport is less sensitive to the strength of the applied electric field, as a result of which the variability induced by local fluctuations in the transmembrane potential is alleviated. This conclusion is relevant in the context of delivery and sampling via electroporation. This lack of uniformity and efficiency is a major source of technical noise for both bulk and micro/nano electroporation platforms [139], which hinders translation to practical

applications such as the study of biological heterogeneity at the single-cell level. However, by optimizing device design and increasing the membrane tension, this variability can be minimized, allowing for improved accuracy and reliability.

4.3.5. Small molecule transport is less sensitive to cell membrane tension

We have seen from the model predictions that the delivery or sampling of large molecules may be sub-optimal at lower membrane tensions unless optimal voltage parameters are applied. Increasing the membrane tension increases the amount and uniformity of transport. However, the transport of small molecules ($<r_{min}$) is less sensitive to the membrane tension and efficient transport can be achieved even at lower membrane tensions. The transport of small molecules increases linearly with the applied voltage and shows less variation with membrane tension as compared to large molecule transport (see Supplementary Figure C.2). This was confirmed by our ability to efficiently deliver Propidium Iodide (PI) (hydrodynamic radius = 0.6 nm) into HT 1080 cells without increasing the cell membrane tension, at different applied voltages (see Figure 4.1e and Supplementary Figure C.3). Insensitivity to membrane tension and linear increase with applied voltage has also been reported for the delivery of small molecules in the case of bulk electroporation caling single-cell genomics from phenomenology to mechanism [168]. Another factor contributing to the efficient delivery of small molecules is the presence of pores (<1.5 nm) that are open even after the pulsation period as seen in the model and experimentally verified by Co^{2+} quenching of Calcein AM (see Supplementary Figure C.5).

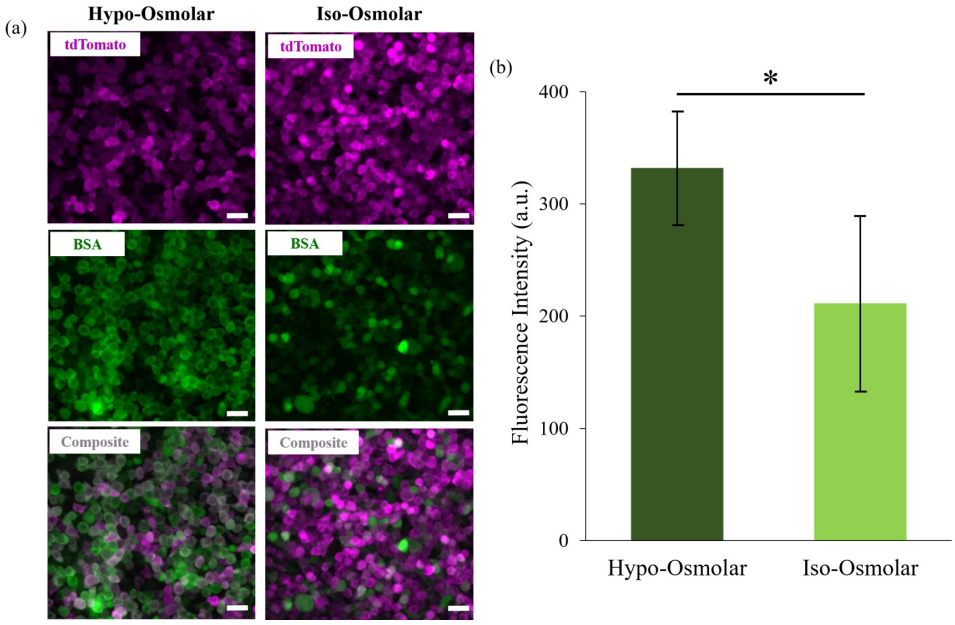

Figure 4.6. **Delivery of BSA into tdTomato expressing MDA-MB 231 cells on the LEPD.** (a) Comparison of BSA delivery under hypo-osmolar and iso-osmolar conditions. Top fluorescence micrographs (magenta channel) show tdTomato expression in the cells after electroporation. Middle fluorescence micrographs (green channel) show the efficiency of BSA delivery under hypo-osmolar and iso-osmolar conditions. Bottom images are a composite of the magenta and green channels showing that tdTomato and BSA expressions are inversely related. This indicates that tdTomato has been sampled from cells in which BSA has been efficiently delivered (All scale bars = 50 μm), (b) The fluorescence intensity of BSA is plotted (in arbitrary units) for cells electroporated under hypo-osmolar and iso-osmolar conditions. Error bars indicate the standard deviation (SD). Increased delivery efficiency is observed for the hypo-osmolar case ($n = 30$ from 3 experiments, *P<0.05).

4.4. Summary and Future Work

In the current chapter, a multiphysics model of localized electroporation and molecular transport is presented to explain the delivery and sampling of molecules in live cells. The model has been applied to optimize the nanochannel density and the cell confluency on the LEPD platform for efficient electroporation. Further, the role of cell membrane

tension and the applied electric field strength in determining the molecular transport was investigated. The model predicts that higher membrane tension increases the amount and uniformity of molecular transport for large molecules over a broad range of applied far-field voltages. While an intermediate voltage is optimal for the transport of large molecules (>3 nm hydrodynamic radius), the transport of small molecules is less sensitive to membrane tension and increases linearly with applied voltage. The model predictions were experimentally validated by delivering small molecules such as PI and Co^{2+} as well as a larger protein (BSA) and plasmid (mCherry) into cells using the LEPD system. Finally, the sampling of a large cytosolic protein (tdTomato) was demonstrated in an engineered cell line using optimal parameters for the LEPD without compromising cell-viability. Overall, our simulation and experimental results suggest that localized electroporation in the LEPD is a promising method of nondestructive temporal sampling of cells. The present model predicts qualitative trends and will be further improved by fitting the several model constants to experimental results using statistical techniques such as the Gaussian Process [169]. Experimentally adjustable parameters such as the nanochannel diameter, electric pulse duration, and frequency that have not been investigated in this work will also be further studied. Using optimal experimental parameters obtained from the fully developed model, localized electroporation can be used for nondestructive, temporal single-cell sampling, which can provide several advantages over existing techniques. Current single-cell profiling techniques enable us to comprehensively identify the molecular state of individual cells. However, these methods are destructive and are unable to track gene expression in the same cells over time. To overcome this issue, temporal dynamics is inferred computationally from the single time point data. Due to the inherent

asynchrony and heterogeneity of a cell population, single-cell data inevitably consist of a large distribution of molecular states. From these data sets, it is possible to construct mathematical models that build time trajectories of cell fate. These models assume maximum parsimony, and as such, the cellular states observed are connected by a trajectory involving minimal transcriptional changes ([170]). However, the dynamics of cell state may be non-hierarchical or stochastic and the maximum parsimony principle may not always hold [170]. This effectively means that a single starting point can lead to multiple branching trajectories or multiple trajectories can lead to the same distribution of states, making it possible to describe a molecular state through several regulatory mechanisms [171]. To distinguish between alternative dynamic pathways and provide additional constraints that enable the identification of the true underlying mechanisms, anchor points or known cell states in the differential pathways are essential (54). Emerging methods partially address this issue by combining high-throughput single-cell sequencing methods with Cas9- or barcode-based genetic perturbations to track cell lineage during organism development [172, 173]. However, to understand the decision-making pathways involved in single-cell processes such as cell differentiation and maturation, tracking the same cell in time is necessary. Temporal sampling of single cells can provide critical information necessary to determine the anchor points involved in these pathways. By combining a high-throughput microfluidics platform for localized electroporation, state-of-the-art ultrasensitive assays and insights gained from the developed model to optimize experimental conditions, nondestructive sampling and analysis of single cells can be realized in the future.

4.5. Materials and Methods

4.5.1. Device Fabrication and Assembly

The device was fabricated using standard soft lithography technique. Briefly, polydimethylsiloxane (PDMS) prepolymer (Sylgard 184, Dow Corning) was mixed in 10:1 (w/w) ratio (base, curing agent), poured on a flat polystyrene dish and cured in an oven at 80^{o}C for 4 hours. The volume of the poured mixture was adjusted to obtain 2 mm thick PDMS slabs. The slabs were cut into 2 cm $\times$ 2 cm squares using a razor blade. Holes of the desired diameter were punched in the PDMS slabs using biopsy punches (Accuderm) to form the cell-culture well and delivery/sampling chamber of the device (see Figure 4.1a). A thin layer of uncured PDMS was prepared by spin-coating the mixture at 1500 rpm for 2 minutes on a silicon wafer. The top cell-culture wells and the bottom delivery/sampling chambers were stamped onto the wafer to ink their surfaces with the uncured PDMS. A 13 mm PC filter membrane (5×10^8 cm^{-2} porosity, AR Brown) was sandwiched between the two layers and cured in the oven at 80^{o}C for 2 hours to obtain the assembled devices (see Figure 4.1b). The devices were sterilized by incubating in 70% ethanol for 15 minutes, rinsing thoroughly with DI water and drying. This was followed by UV exposure for 1 hour. All subsequent steps were carried out in a laminar flow hood to maintain sterility. The top surface of the PC membrane was coated with Fibronectin (Sigma-Aldrich) by incubating in a 1:50 (v/v) solution (0.1% Fibronectin, 1$\times$PBS (Gibco)) to promote cell adhesion. The bottom PC surface and the delivery/sampling chamber were then passivated by dipping the device in a 0.2% (w/v) solution of Pluronic F-127 (Sigma-Aldrich)

in 1×PBS. The device was then washed 3 times with 1×PBS to remove any unattached residues before seeding cells.

4.5.2. Multiphysics Modeling

Numerical simulations were performed in COMSOL Multiphysics 5.2a. A lumped circuit model (see Chapter Figure 4.1c) including passive electronic components was used to solve for the transient electric field. The governing coupled ordinary differential equations (ODEs) for the electric field were solved using the Global ODEs and the differential algebraic equations (DAEs) module, available in COMSOL, to obtain the transmembrane potential (TMP). The formation and evolution of pores on the plasma membrane in response to the applied TMP is governed by the Einstein-Smoluchowski equation [174]. A tension coupled non-linear form of this equation, [175] which accounts for the tension mediated interaction between pores, was solved using the General Form partial differential equation (PDE) module to obtain the distribution of electro-pores at every time point. The electric field and the pore evolution equations were coupled through the effective electrical conductivity (κ) of the cell membrane. The electro-diffusive transport of molecules [151] across the cell membrane during electroporation was estimated using the Nernst-Planck equation (see 4.3). For the Finite Element Analysis, quadratic Lagrange shape functions were used for spatial discretization. The discretized non-linear equation was solved using the Newton-Raphson method at every time step. Temporal integration was performed using the implicit generalized-α scheme.

4.5.3. Cell Culture

HT 1080 and MDA-MB 231 cell lines were obtained from the Mrksich Lab at Northwestern University. CHO and tdTomato expressing MDA-MB 231 cell lines were obtained from Recombinant Protein Production Core (rPPC) and Developmental Therapeutics Core (CDT) facilities at Northwestern University. HT 1080, MDA-MB 231 cells were cultured in DMEM (Gibco) supplemented with 10% FBS (Gibco) and 1% Penicillin-Streptomycin (Gibco). CHO cells were cultured in DMEM/F-12 (Gibco) supplemented with 10% FBS and 1% Penicillin-Streptomycin. The cultures were passaged every 3-5 days upon reaching 80-90% confluency using 0.25% Trypsin (Gibco). The cells were plated on the device by dispensing 30 μl of cell suspension at a desired density and allowed to adhere. The devices were placed within a 6-well plate (USA Scientific) with the appropriate medium depending on the cell type, inside the incubator (at 37ºC with 5% CO_2) for a day before performing the electroporation experiments. All experiments were performed on cultures that were passaged less than 10 times.

4.5.4. Electrical Setup and general protocol for electroporation

A function generator (Agilent) connected to a voltage amplifier (OPA445, Texas Instruments) was used to apply the electroporation pulses (10-50 V, 1-5 ms square pulses, 100-500 pulses, 1-20 Hz). The voltage traces were verified on an oscilloscope (LeCroy). Two ITO coated glass slides (top and bottom, see Figure 4.1a) served as the positive and ground electrodes for pulse application. The molecular cargo for delivery was loaded in the bottom chamber of the LEPD. Conversely, the extracted molecules in sampling experiments were collected from the same chamber and transferred to a 96-well plate.

4.5.5. Delivery of proteins and small molecules

MDA-MB 231 cells (10,000) plated in the LEPD on the previous day were first washed three times to remove debris before loading 1xPBS in the cell culture chamber. Propidium Iodide (Life Technologies, diluted to a concentration of 20 μg/ml in 1×PBS) was loaded into the bottom chamber. The device was placed between the two ITO coated glass slides (Nanocs) and three pulses of 0.5 ms duration and 15 V amplitude were typically applied in these experiments. After waiting for 15 mins to allow for molecular diffusion, the LEPD was washed 3 times with 1×PBS to remove residues before imaging on a fluorescence microscope.

BSA delivery was performed using a 2.5 mg/ml solution of BSA with Alexa Fluor 488 conjugate (Invitrogen) in 1×Iso-osmolar or 1×Hypo-osmolar buffer. ForCO_2+ quenching of Calcein-AM, CHO cells ($\approx$ 10,000) plated on the LEPD the previous day were first stained with Calcein-AM (Life Technologies, diluted to 1 μg/ml in 1×PBS) and incubated for 15 minutes. The cells were washed thrice before loading with 1×PBS. The bottom chamber was also loaded with 1×PBS and electroporation pulses (15 V, 0.5 ms, 1-3 pulses) were applied. 500 mM $CoCl_2$ was introduced approximately 60 s post-electroporation to visualize the loss of green fluorescence. The quenched fluorescence was later recovered by injecting 1 mM EDTA solution 3 minutes post electroporation [176].

4.5.6. Delivery of Plasmids

A 4-kb plasmid encoding the fluorescent protein mCherry (gift from Dr. Vincent Lemaitre, iNfinitesimal LLC) was used at a concentration of 20 ng/μl in 1×Hypo-osmolar buffer. Approximately 10,000 MDA-MB 231 or HT 1080 cells were plated on a device and allowed

to adhere for 24 hours before electroporation. The electroporated cells were then washed thrice with 1×PBS and incubated for a day (at 37ºC and 5%CO_2) before imaging on a fluorescent microscope. An electroporation train of 100 voltage pulses, each of 5 ms duration, was applied at a repetition frequency of 20 Hz. The voltage amplitude was varied from 10 to 40 V to optimize the efficiency of transfection.

4.5.7. Lipofectamine Transfection

MDA-MB 231 cells were transfected using Lipofectamine 3000 (Thermo Fisher Scientific) following the manufacturer's protocol. Briefly, MDA-MB 231 cells were plated on a 96-well plate at 70% confluency. For each well 100 ng of the mCherry plasmid (0.5 μg/μl) mixed with 5 μl serum free DMEM and 0.2 μl P3000 reagent was used. Two doses (0.15 μl and 0.3 μl) of lipofectamine 3000 reagent were mixed with 5 μl serum-free DMEM for each condition. The DNA solution and lipofectamine reagent were mixed in 1:1 ratio and incubated in room temperature for 15 minutes. The DNA-lipid complex was administered to the well with cells growing in 100 μl of culture media. The transfection efficiency was analyzed after 48 hours using fluorescence microscopy.

4.5.8. tdTomato Sampling

tdTomato expressing MDA-MB 231 cells were plated at a density of 10,000 cells per device and incubated for 24 hours. Both the top and bottom chambers in the device were loaded with 1xHypo-osmolar buffer before applying electroporation pulses. In different experiments, the pulse amplitude and duration were kept constant at 30 V or 50 V and 5 ms respectively, while the number of pulses was varied from 100 to 500. The sampled

tdTomato molecules were allowed to diffuse to the bottom chamber for 30 minutes before transferring them to a 96-well plate using a micropipette. A well plate reader (Synergy H1m) was used with the following settings to measure the fluorescence level from the extracted protein – excitation/emission at 553/582 nm, gain: 150 and integration time 1 sec.

4.5.9. Fluorescence Microscopy and Image Analysis

Fluorescence images were acquired on a Nikon Eclipse Ti-U Microscope equipped with an Andor Zyla 5.5 sCMOS camera. Image acquisition was controlled using Micro-Manager software. The acquired images were analyzed using FIJI, an open source image-processing package.

4.6. Acknowledgments

This work was supported by the National Cancer Institute of the National Institutes of Health (NIH) under Award Number U54CA199091 and by NIH SBIR R44 GM110893-02. The content is solely the responsibility of the authors and does not necessarily represent the official views of the National Institutes of Health. I am thankful to Prithvijit Mukherjee for developing the multi-physics model and for his experiments on BSA and PI delivery.

Bibliography

[1] K. L. Ekinci and M. L. Roukes. Nanoelectromechanical systems. *Review of Scientific Instruments*, 76(6):061101, 2005.

[2] J. Lee, Z. Wang, K. He, R. Yang, J. Shan, and P. X. Feng. Electrically tunable single- and few-layer MoS_2 nanoelectromechanical systems with broad dynamic range. *Science Advances*, 4(3):eaao6653, 2018.

[3] C. H. Liu, I. S. Kim, and L. J. Lauhon. Optical control of mechanical mode-coupling within a MoS_2 resonator in the strong-coupling regime. *Nano Letters*, 15(10):6727–6731, 2015.

[4] J. P. Mathew, R. N. Patel, A. Borah, R. Vijay, and M. M. Deshmukh. Dynamical strong coupling and parametric amplification of mechanical modes of graphene drums. *Nature Nanotechnology*, 11(9):747–751, 2016.

[5] R. De Alba, F. Massel, I. R. Storch, T. S. Abhilash, A. Hui, P. L. McEuen, H. G. Craighead, and J. M. Parpia. Tunable phonon-cavity coupling in graphene membranes. *Nature Nanotechnology*, 11(9):741–746, 2016.

[6] K. S Novoselov, A. K Geim, S. V Morozov, D. Jiang, Y. Zhang, S. V Dubonos, I. V Grigorieva, and A. A Firsov. Electric field effect in atomically thin carbon films. *Science*, 306(5696):666–669, 2004.

[7] K. S. Novoselov, D Jiang, F. Schedin, T. J. Booth, V. V. Khotkevich, S. V. Morozov, and A. K. Geim. Two-dimensional atomic crystals. *Proceedings of the National Academy of Sciences*, 102(30):10451–10453, 2005.

[8] C. Lee, X. Wei, J. W Kysar, and J. Hone. Measurement of the elastic properties and intrinsic strength of monolayer graphene. *Science*, 321(5887):385–388, 2008.

[9] M. C Lemme, L. J. Li, T. Palacios, and F. Schwierz. Two-dimensional materials for electronic applications. *MRS Bulletin*, 39(8):711–718, 2014.

[10] K. A. N. Duerloo, M. T. Ong, and E. J. Reed. Intrinsic piezoelectricity in two-dimensional materials. *Journal of Physical Chemistry Letters*, 3(19):2871–2876, 2012.

[11] J. W. Jiang, H. S. Park, and T. Rabczuk. MoS_2 nanoresonators: intrinsically better than graphene? *Nanoscale*, 6(7):3618–25, 2014.

[12] L. Cai, N. Friedman, and X. S. Xie. Stochastic protein expression in individual cells at the single molecule level. *Nature*, 440(7082):358, 2006.

[13] N. Rosenfeld, J. W. Young, U. Alon, P. S. Swain, and M. B. Elowitz. Gene regulation at the single-cell level. *Science*, 307(5717):1962–1965, 2005.

[14] N. V. Fuchs, S. Loewer, G. Q. Daley, Z. Izsvák, J. Löwer, and R. Löwer. Human endogenous retrovirus K (HML-2) RNA and protein expression is a marker for human embryonic and induced pluripotent stem cells. *Retrovirology*, 10(1):115, 2013.

[15] N. M. Toriello, E. S. Douglas, N. Thaitrong, S. C. Hsiao, M. B. Francis, C. R. Bertozzi, and R. A Mathies. Integrated microfluidic bioprocessor for single-cell gene expression analysis. *Proceedings of the National Academy of Sciences*, 105(51):20173–20178, 2008.

[16] J. Yu, J. Zhou, A. Sutherland, W. Wei, Y. S. Shin, M. Xue, and J. R Heath. Microfluidics-based single-cell functional proteomics for fundamental and applied biomedical applications. *Annual Review of Analytical Chemistry*, 7:275–295, 2014.

[17] I. Singec, R. Knoth, R. P Meyer, J. Maciaczyk, B. Volk, G. Nikkhah, M. Frotscher, and E. Y. Snyder. Defining the actual sensitivity and specificity of the neurosphere assay in stem cell biology. *Nature Methods*, 3(10):801, 2006.

[18] J. R. Heath and M. E. Davis. Nanotechnology and cancer. *Annual Review of Medicine*, 59:251–265, 2008.

[19] K. Takahashi, K. Tanabe, M. Ohnuki, M. Narita, T. Ichisaka, K. Tomoda, and S. Yamanaka. Induction of pluripotent stem cells from adult human fibroblasts by defined factors. *Cell*, 131(5):861–872, 2007.

[20] S. M. Wu and K. Hochedlinger. Harnessing the potential of induced pluripotent stem cells for regenerative medicine. *Nature Cell Biology*, 13(5):497, 2011.

[21] M. Grskovic, A. Javaherian, B. Strulovici, and G. Q. Daley. Induced pluripotent stem cells—opportunities for disease modelling and drug discovery. *Nature Reviews*

Drug Discovery, 10(12):915, 2011.

[22] X. D. Wei, L. Mao, R. A. Soler-Crespo, J. T. Paci, J. X. Huang, S. T. Nguyen, and H. D. Espinosa. Plasticity and ductility in graphene oxide through a mechanochemically induced damage tolerance mechanism. *Nature Communications*, 6, 2015.

[23] A. Splendiani, L. Sun, Y. B. Zhang, T. S. Li, J. Kim, C. Y. Chim, G. Galli, and F. Wang. Emerging photoluminescence in monolayer MoS_2. *Nano Letters*, 10(4):1271–1275, 2010.

[24] E. S. Reich. Phosphorene excites materials scientists. *Nature*, 506(7486):19–19, 2014.

[25] A. J. Mannix, X. F. Zhou, B. Kiraly, J. D. Wood, D. Alducin, B. D. Myers, X. L. Liu, B. L. Fisher, U. Santiago, J. R. Guest, M. J. Yacaman, A. Ponce, A. R. Oganov, M. C. Hersam, and N. P. Guisinger. Synthesis of borophenes: Anisotropic, two-dimensional boron polymorphs. *Science*, 350(6267):1513–1516, 2015.

[26] O. Lopez-Sanchez, D. Lembke, M. Kayci, A. Radenovic, and A. Kis. Ultrasensitive photodetectors based on monolayer MoS_2. *Nature Nanotechnology*, 8(7):497–501, 2013.

[27] Y. Ye, Z. J. Wong, X. F. Lu, X. J. Ni, H. Y. Zhu, X. H. Chen, Y. Wang, and X. Zhang. Monolayer excitonic laser. *Nature Photonics*, 9(11):733–737, 2015.

[28] S. F. Wu, S. Buckley, J. R. Schaibley, L. F. Feng, J. Q. Yan, D. G. Mandrus, F. Hatami, W. Yao, J. Vuckovic, A. Majumdar, and X. D. Xu. Monolayer semiconductor nanocavity lasers with ultralow thresholds. *Nature*, 520(7545):69–U142, 2015.

[29] H. J. Conley, B. Wang, J. I. Ziegler, R. F. Haglund, S. T. Pantelides, and K. I. Bolotin. Bandgap engineering of strained monolayer and bilayer MoS_2. *Nano Letters*, 13(8):3626–3630, 2013.

[30] S. B. Desai, G. Seol, J. S. Kang, H. Fang, C. Battaglia, R. Kapadia, J. W. Ager, J. Guo, and A. Javey. Strain-induced indirect to direct bandgap transition in multi layer WSe_2. *Nano Letters*, 14(8):4592–4597, 2014.

[31] J. Feng, X. F. Qian, C. W. Huang, and J. Li. Strain-engineered artificial atom as a broad-spectrum solar energy funnel. *Nature Photonics*, 6(12):865–871, 2012.

[32] H. Y. Zhu, Y. Wang, J. Xiao, M. Liu, S. M. Xiong, Z. J. Wong, Z. L. Ye, Y. Ye, X. B. Yin, and X. Zhang. Observation of piezoelectricity in free-standing monolayer

MoS_2. *Nature Nanotechnology*, 10(2):151–155, 2015.

[33] J. J. 51, Y. W. Lan, A. Z. Stieg, J. H. Chen, Y. L. Zhong, L. J. Li, C. D. Chen, Y. Zhang, and K. L. Wang. Piezoelectric effect in chemical vapour deposition-grown atomic-monolayer triangular molybdenum disulfide piezotronics. *Nature Communications*, 6, 2015.

[34] K. F. Mak, K. L. McGill, J. Park, and P. L. McEuen. The valley hall effect in MoS_2 transistors. *Science*, 344(6191):1489–1492, 2014.

[35] Q. H. Wang, K. Kalantar-Zadeh, A. Kis, J. N. Coleman, and M. S. Strano. Electronics and optoelectronics of two-dimensional transition metal dichalcogenides. *Nature Nanotechnology*, 7(11):699–712, 2012.

[36] X. Yin, Z. Ye, D. A. Chenet, Y. Ye, K. O'Brien, J. C Hone, and X. Zhang. Edge nonlinear optics on a MoS_2 atomic monolayer. *Science*, 344(6183):488–490, 2014.

[37] N. Kumar, S. Najmaei, Q. Cui, F. Ceballos, P. M. Ajayan, J. Lou, and H. Zhao. Second harmonic microscopy of monolayer MoS_2. *Physical Review B*, 87(16):161403, 2013.

[38] Y. Wang, J. Xiao, H. Zhu, Y. Li, Y. Alsaid, K. Y. Fong, Y. Zhou, S. Wang, W. Shi, Y. Wang, et al. Structural phase transition in monolayer $MoTe_2$ driven by electrostatic doping. *Nature*, 550(7677):487, 2017.

[39] J. S. Bunch, A. M. van der Zande, S. S. Verbridge, I. W. Frank, D. M. Tanenbaum, J. M. Parpia, H. G. Craighead, and P. L. McEuen. Electromechanical resonators from graphene sheets. *Science*, 315(5811):490–493, 2007.

[40] J. T. Robinson, M. Zalalutdinov, J. W. Baldwin, E. S. Snow, Z. Q. Wei, P. Sheehan, and B. H. Houston. Wafer-scale reduced graphene oxide films for nanomechanical devices. *Nano Letters*, 8(10):3441–3445, 2008.

[41] A. Castellanos-Gomez, R. van Leeuwen, M. Buscema, H. S. J. van der Zant, G. A. Steele, and W. J. Venstra. Single-layer MoS_2 mechanical resonators. *Advanced Materials*, 25(46):6719–6723, 2013.

[42] J. Lee, Z. H. Wang, K. L. He, J. Shan, and P. X. L. Feng. High frequency MoS_2 nanomechanical resonators. *ACS Nano*, 7(7):6086–6091, 2013.

[43] A. M. van der Zande, P. Y. Huang, D. A. Chenet, T. C. Berkelbach, Y. M. You, G. H. Lee, T. F. Heinz, D. R. Reichman, D. A. Muller, and J. C. Hone. Grains and grain boundaries in highly crystalline monolayer molybdenum disulphide. *Nature*

Materials, 12(6):554–561, 2013.

[44] M. Kumar and H. Bhaskaran. Ultrasensitive room-temperature piezoresistive transduction in graphene-based nanoelectromechanical systems. *Nano Letters*, 15(4):2562–2567, 2015.

[45] Z. H. Wang, H. Jia, X. Q. Zheng, R. Yang, G. J. Ye, X. H. Chen, and P. X. L. Feng. Resolving and tuning mechanical anisotropy in black phosphorus via nanomechanical multimode resonance spectromicroscopy. *Nano Letters*, 16(9):5394–5400, 2016.

[46] Z. H. Wang and P. X. L. Feng. Design of black phosphorus 2D nanomechanical resonators by exploiting the intrinsic mechanical anisotropy. *2D Materials*, 2(2), 2015.

[47] R. A. Barton, I. R. Storch, V. P. Adiga, R. Sakakibara, B. R. Cipriany, B. Ilic, S. P. Wang, P. Ong, P. L. McEuen, J. M. Parpia, and H. G. Craighead. Photothermal self-oscillation and laser cooling of graphene optomechanical systems. *Nano Letters*, 12(9):4681–4686, 2012.

[48] M. Kumar, B. Choubey, and H. Bhaskaran. Nanomechanical resonators show higher order nonlinearity at room temperature. *arXiv preprint arXiv:1703.03094*, 2017.

[49] N. Morell, A. Reserbat-Plantey, I. Tsioutsios, K. G. Schadler, F. Dubin, F. H. L. Koppens, and A. Bachtold. High quality factor mechanical resonators based on WSe_2 monolayers. *Nano Letters*, 16(8):5102–5108, 2016.

[50] B. R. Matis, B. H. Houston, and J. W. Baldwin. Energy dissipation pathways in few-layer MoS_2 nanoelectromechanical systems. *Scientific Reports*, 7, 2017.

[51] H. Li, Q. Zhang, C. C. R. Yap, B. K. Tay, T. H. T. Edwin, A. Olivier, and D. Baillargeat. From bulk to monolayer MoS_2: Evolution of Raman scattering. *Advanced Functional Materials*, 22(7):1385–1390, 2012.

[52] K. L. Ekinci. Electromechanical transducers at the nanoscale: Actuation and sensing of motion in nanoelectromechanical systems (NEMS). *Small*, 1(8-9):786–797, 2005.

[53] K. S. Novoselov and A. H. Castro Neto. Two-dimensional crystals-based heterostructures: materials with tailored properties. *Physica Scripta*, T146, 2012.

[54] A. Castellanos-Gomez, M. Buscema, R. Molenaar, V. Singh, L. Janssen, H. S. J. van der Zant, and G. A. Steele. Deterministic transfer of two-dimensional materials by all-dry viscoelastic stamping. *2D Materials*, 1(1), 2014.

[55] P. Blake, E. W. Hill, A. H. Castro Neto, K. S. Novoselov, D. Jiang, R. Yang, T. J. Booth, and A. K. Geim. Making graphene visible. *Applied Physics Letters*, 91(6), 2007.

[56] A. Berkdemir, H. R. Gutierrez, A. R. Botello-Mendez, N. Perea-Lopez, A. L. Elias, C. I. Chia, B. Wang, V. H. Crespi, F. Lopez-Urias, J. C. Charlier, H. Terrones, and M. Terrones. Identification of individual and few layers of WS_2 using Raman spectroscopy. *Scientific Reports*, 3, 2013.

[57] B. R. Carvalho, Y. X. Wang, S. Mignuzzi, D. Roy, M. Terrones, C. Fantini, V. H. Crespi, L. M. Malard, and M. A. Pimenta. Intervalley scattering by acoustic phonons in two-dimensional MoS_2 revealed by double-resonance Raman spectroscopy. *Nature Communications*, 8, 2017.

[58] X. Wei, Z. Yu, F. Hu, Y. Cheng, L. Yu, X. Wang, M. Xiao, J. Wang, and Y. Wang, X.and Shi. Mo-o bond doping and related-defect assisted enhancement of photoluminescence in monolayer MoS_2. *AIP Advances*, 4(12):123004, 2014.

[59] G. B Warburton. The vibration of rectangular plates. *Proceedings of the Institution of Mechanical Engineers*, 168(1):371–384, 1954.

[60] S. Xiong and G. X. Cao. Molecular dynamics simulations of mechanical properties of monolayer MoS_2. *Nanotechnology*, 26(18), 2015.

[61] A. Reserbat-Plantey, L. Marty, O. Arcizet, N. Bendiab, and V. Bouchiat. A local optical probe for measuring motion and stress in a nanoelectromechanical system. *Nature Nanotechnology*, 7(3):151–155, 2012.

[62] H. Zeng, G. B. Liu, J. Dai, Y. Yan, B. Zhu, R. He, L. Xie, S. Xu, X. Chen, W. Yao, et al. Optical signature of symmetry variations and spin-valley coupling in atomically thin tungsten dichalcogenides. *Scientific Reports*.

[63] P. Tonndorf, R. Schmidt, P. Böttger, X. Zhang, J. Börner, A. Liebig, M. Albrecht, C. Kloc, O. Gordan, D. R. Zahn, et al. Photoluminescence emission and Raman response of monolayer MoS_2, $MoSe_2$, and WSe_2. *Optics Express*, 21(4):4908–4916, 2013.

[64] W. Zhao, Z. Ghorannevis, K. K. Amara, J. R. Pang, M. Toh, X. Zhang, C. Kloc, P. H. Tan, and G. Eda. Lattice dynamics in mono-and few-layer sheets of WS_2 and WSe_2. *Nanoscale*, 5(20):9677–9683, 2013.

[65] M. Yamamoto, S. T. Wang, M. Ni, Y. F. Lin, S. L. Li, S. Aikawa, W. B. Jian, K. Ueno, K. Wakabayashi, and K. Tsukagoshi. Strong enhancement of Raman

scattering from a bulk-inactive vibrational mode in few-layer $MoTe_2$. *ACS Nano*, 8(4):3895–3903, 2014.

[66] C. Ruppert, O. B. Aslan, and T. F. Heinz. Optical properties and band gap of single-and few-layer $MoTe_2$ crystals. *Nano letters*, 14(11):6231–6236, 2014.

[67] A. H. Nayfeh and D. T. Mook. *Nonlinear oscillations*. Pure and applied mathematics. Wiley, New York, 1979.

[68] A. H. Nayfeh. *Nonlinear interactions : analytical, computational and experimental methods*. Wiley, New York, 2000.

[69] A. I. Manevich and L. I. Manevitch. *The mechanics of nonlinear systems with internal resonances*. World Scientific, 2005.

[70] D. Antonio, D. H. Zanette, and D. Lopez. Frequency stabilization in nonlinear micromechanical oscillators. *Nature Communications*, 3:806, 2012.

[71] K. Asadi, J. Yu, and H. N. Cho. Nonlinear couplings and energy transfers in micro- and nano-mechanical resonators: intermodal coupling, internal resonance and synchronization. *Philosophical Transactions of the Royal Society A: Mathematical, Physical and Engineering Sciences*, 376(2127), 2018.

[72] C. Chen, D. H. Zanette, D. A. Czaplewski, S. Shaw, and D. Lopez. Direct observation of coherent energy transfer in nonlinear micromechanical oscillators. *Nature Communications*, 8:15523, 2017.

[73] J. Guttinger, A. Noury, P. Weber, A. M. Eriksson, C. Lagoin, J. MoSer, C. Eichler, A. Wallraff, A. Isacsson, and A. Bachtold. Energy-dependent path of dissipation in nanomechanical resonators. *Nature Nanotechnology*, 12(7):631–636, 2017.

[74] M. H. Matheny, L. G. Villanueva, R. B. Karabalin, J. E. Sader, and M. L. Roukes. Nonlinear mode-coupling in nanomechanical systems. *Nano Letters*, 13(4):1622–1626, 2013.

[75] R. Lifshitz and M. C. Cross. *Reviews of Nonlinear Dynamics and Complexity*. Wiley-VCH Verlag GmbH and Co. KGaA, 2009.

[76] H. J. R. Westra, M. Poot, H. S. J. van der Zant, and W. J. Venstra. Nonlinear modal interactions in clamped-clamped mechanical resonators. *Physical Review Letters*, 105(11), 2010.

[77] A. B. Ari, M. C. Karakan, C. Yanik, I. I. Kaya, and M. S. Hanay. Intermodal coupling as a probe for detecting nanomechanical modes. *Physical Review Applied*, 9(3), 2018.

[78] J. P. Mathew, A. Bhushan, and M. M. Deshmukh. Tension mediated nonlinear coupling between orthogonal mechanical modes of nanowire resonators. *Solid State Communications*, 282:17–20, 2018.

[79] A. Eichler, M. D. Ruiz, J. A. Plaza, and A. Bachtold. Strong coupling between mechanical modes in a nanotube resonator. *Physical Review Letters*, 109(2), 2012.

[80] C. Samanta, P. R. Y. Gangavarapu, and A. K. Naik. Nonlinear mode coupling and internal resonances in MoS_2 nanoelectromechanical system. *Applied Physics Letters*, 107(17), 2015.

[81] G. Luo, Z. Z. Zhang, G. W. Deng, H. O. Li, G. Cao, M. Xiao, G. C. Guo, L. Tian, and G. P. Guo. Strong indirect coupling between graphene-based mechanical resonators via a phonon cavity. *Nature Communications*, 9, 2018.

[82] S. S. P. Nathamgari, S. Dong, E. Hosseinian, L. J. Lauhon, and H. D. Espinosa. An experimental setup for combined in-vacuo Raman spectroscopy and cavity-interferometry measurements on TMDC nano-resonators. *Experimental Mechanics*, pages 1–11, 2018.

[83] N. Morell, A. Reserbat-Plantey, I. Tsioutsios, K. G. Schadler, F. Dubin, F. H. L. Koppens, and A. Bachtold. High quality factor mechanical resonators based on WSe_2 monolayers. *Nano Letters*, 16(8):5102–5108, 2016.

[84] R. A. Barton, I. R. Storch, V. P. Adiga, R. Sakakibara, B. R. Cipriany, B. Ilic, S. P. Wang, P. Ong, P. L. McEuen, J. M. Parpia, and H. G. Craighead. Photothermal self-oscillation and laser cooling of graphene optomechanical systems. *Nano Letters*, 12(9):4681–4686, 2012.

[85] A. Castellanos-Gomez, R. van Leeuwen, M. Buscema, H. S. J. van der Zant, G. A. Steele, and W. J. Venstra. Single-layer MoS_2 mechanical resonators. *Advanced Materials*, 25(46):6719–6723, 2013.

[86] B. R. Matis, B. H. Houston, and J. W. Baldwin. Energy dissipation pathways in few-layer MoS_2 nanoelectromechanical systems. *Scientific Reports*, 7(1):5656, 2017.

[87] S. Xiong and G. Cao. Molecular dynamics simulations of mechanical properties of monolayer MoS_2. *Nanotechnology*, 26(18):185705, 2015.

[88] K. Lai, W. B. Zhang, F. Zhou, F. Zeng, and B. Y. Tang. Bending rigidity of transition metal dichalcogenide monolayers from first-principles. *Journal of Physics D-Applied Physics*, 49(18), 2016.

[89] E. L. Gao and Z. P. Xu. Thin-shell thickness of two-dimensional materials. *Journal of Applied Mechanics-Transactions of the ASME*, 82(12), 2015.

[90] J. Lee, Z. Wang, K. He, J. Shan, and P. X. L Feng. High frequency MoS_2 nanomechanical resonators. *ACS Nano*, 7(7):6086–91, 2013.

[91] S. Bertolazzi, J. Brivio, and A. Kis. Stretching and breaking of ultrathin MoS_2. *ACS Nano*, 5(12):9703–9, 2011.

[92] M. Kumar and H. Bhaskaran. Ultrasensitive room-temperature piezoresistive transduction in graphene-based nanoelectromechanical systems. *Nano Letters*, 15(4):2562–7, 2015.

[93] D. Davidovikj, J. J. Slim, S. J. Cartamil-Bueno, H. S. van der Zant, P. G. Steeneken, and W. J. Venstra. Visualizing the motion of graphene nanodrums. *Nano Letters*, 16(4):2768–73, 2016.

[94] D. Garcia-Sanchez, A. M. van der Zande, A. S. Paulo, B. Lassagne, P. L. McEuen, and A. Bachtold. Imaging mechanical vibrations in suspended graphene sheets. *Nano Letters*, 8(5):1399–403, 2008.

[95] S. Y. Kim and H. S. Park. The importance of edge effects on the intrinsic loss mechanisms of graphene nanoresonators. *Nano Letters*, 9(3):969–974, 2009.

[96] A. Eichler, J. MoSer, J. Chaste, M. Zdrojek, I. Wilson-Rae, and A. Bachtold. Nonlinear damping in mechanical resonators made from carbon nanotubes and graphene. *Nature Nanotechnology*, 6(6):339–342, 2011.

[97] C. Samanta, N. Arora, and A. K. Naik. Tuning of geometric nonlinearity in ultrathin nanoelectromechanical systems. *Applied Physics Letters*, 113(11), 2018.

[98] J. M. Johnson and A. K. Bajaj. Amplitude modulated and chaotic dynamics in resonant motion of strings. *Journal of Sound and Vibration*, 128(1):87–107, 1989.

[99] R. De Alba, F. Massel, I. R. Storch, T. S. Abhilash, A. Hui, P. L. McEuen, H. G. Craighead, and J. M. Parpia. Tunable phonon-cavity coupling in graphene membranes. *Nat. Nanotechnol.*, 11(9):741–746, 2016.

[100] A. M. Eriksson, D. Midtvedt, A. Croy, and A. Isacsson. Frequency tuning, nonlinearities and mode coupling in circular mechanical graphene resonators. *Nanotechnology*, 24(39):395702, 2013.

[101] X. Wei, L. Ruihong, and L. Shuang. Resonance and bifurcation in a nonlinear duffing system with cubic coupled terms. *Nonlinear Dynamics*, 46(1-2):211–221, 2006.

[102] F. Mangussi and D. H. Zanette. Internal resonance in a vibrating beam: A zoo of nonlinear resonance peaks. *Plos One*, 11(9), 2016.

[103] A. Dhooge, W. Govaerts, Y. A. Kuznetsov, H. G. E. Meijer, and B. Sautois. New features of the software MatCont for bifurcation analysis of dynamical systems. *Mathematical and Computer Modelling of Dynamical Systems*, 14(2):147–175, 2008.

[104] D. Rugar and P. Grutter. Mechanical parametric amplification and thermomechanical noise squeezing. *Physical Review Letters*, 67(6):699–702, 1991.

[105] L. Papariello, O. Zilberberg, A. Eichler, and R. Chitra. Ultrasensitive hysteretic force sensing with parametric nonlinear oscillators. *Physical Review E*, 94(2-1):022201, 2016.

[106] P. Prasad, N. Arora, and A. K. Naik. Parametric amplification in MoS_2 drum resonator. *Nanoscale*, 9(46):18299–18304, 2017.

[107] P. Weber, J. Guttinger, A. Noury, J. Vergara-Cruz, and A. Bachtold. Force sensitivity of multilayer graphene optomechanical devices. *Nature Communications*, 7, 2016.

[108] S. L. de Bonis, C. Urgell, W. Yang, C. Samanta, A. Noury, J. Vergara-Cruz, Q. Dong, Y. Jin, and A. Bachtold. Ultrasensitive displacement noise measurement of carbon nanotube mechanical resonators. *Nano Letters*, 18(8):5324–5328, 2018.

[109] C. Touze, S. Bilbao, and O. Cadot. Transition scenario to turbulence in thin vibrating plates. *Journal of Sound and Vibration*, 331(2):412–433, 2012.

[110] M. J. Biercuk, H. Uys, J. W. Britton, A. P. VanDevender, and J. J. Bollinger. Ultrasensitive detection of force and displacement using trapped ions. *Nature Nanotechnology*, 5(9):646–650, 2010.

[111] J. Moser, J. Guttinger, A. Eichler, M. J. Esplandiu, D. E. Liu, M. I. Dykman, and A. Bachtold. Ultrasensitive force detection with a nanotube mechanical resonator. *Nature Nanotechnology*, 8(7):493–496, 2013.

[112] H. J. Mamin and D. Rugar. Sub-attonewton force detection at millikelvin temperatures. *Applied Physics Letters*, 79(20):3358–3360, 2001.

[113] J. M. Nichol, E. R. Hemesath, L. J. Lauhon, and R. Budakian. Nanomechanical detection of nuclear magnetic resonance using a silicon nanowire oscillator. *Physical Review B*, 85(5), 2012.

[114] E. Gavartin, P. Verlot, and T. J. Kippenberg. A hybrid on-chip optomechanical transducer for ultrasensitive force measurements. *Nature Nanotechnology*, 7(8):509–514, 2012.

[115] M. C. Cross. Improving the frequency precision of oscillators by synchronization. *Physical Review E*, 85(4), 2012.

[116] R. Van Leeuwen, A. Castellanos-Gomez, G. A. Steele, H. S. J. van der Zant, and W. J. Venstra. Time-domain response of atomically thin MoS_2 nanomechanical resonators. *Applied Physics Letters*, 105(4):041911, 2014.

[117] S. M. Brooker, A. M. Bond, C. Y. Peng, and J. A. Kessler. β1-integrin restricts astrocytic differentiation of adult hippocampal neural stem cells. *Glia*, 64(7):1235–1251, 2016.

[118] S. G. Higgins and M. M. Stevens. Extracting the contents of living cells. *Science*, 356(6336):379–380, 2017.

[119] G. Gintant, P. T. Sager, and N. Stockbridge. Evolution of strategies to improve preclinical cardiac safety testing. *Nature Reviews Drug Discovery*, 15(7):457–471, 2016.

[120] L. Duan, B. J. Bhattacharyya, A. Belmadani, L. Pan, R. J. Miller, and J. A. Kessler. Stem cell derived basal forebrain cholinergic neurons from Alzheimer's disease patients are more susceptible to cell death. *Molecular Neurodegeneration*, 9(1):3, 2014.

[121] S. M. Prakadan, A. K. Shalek, and D. A. Weitz. Scaling by shrinking: empowering single-cell 'omics' with microfluidic devices. *Nature Reviews Genetics*, 18:345, 2017.

[122] J. R. Heath, A. Ribas, and P. S. Mischel. Single cell analytic tools for drug discovery and development. *Nature Reviews Drug Discovery*, 15(3):204–216, 2016.

[123] A. J. Hughes, D. P. Spelke, Z. Xu, C. C. Kang, D. V. Schaffer, and A. E. Herr. Single-cell western blotting. *Nature Methods*, 11:749, 2014.

[124] Q. Shi, L. Qin, W. Wei, F. Geng, R. Fan, Y. S. Shin, D. Guo, L. Hood, P. S. Mischel, and J. R. Heath. Single-cell proteomic chip for profiling intracellular signaling pathways in single tumor cells. *Proceedings of the National Academy of Sciences*, 109(2):419–424, 2012.

[125] A. O. Ogunniyi, C. M. Story, E. Papa, E. Guillen, and J. C. Love. Screening individual hybridomas by microengraving to discover monoclonal antibodies. *Nature Protocols*, 4(5):767–82, 2009.

[126] T. M. Gierahn, M. H. Wadsworth Ii, T. K. Hughes, B. D. Bryson, A. Butler, R. Satija, S. Fortune, J. C. Love, and A. K. Shalek. Seq-well: portable, low-cost RNA sequencing of single cells at high throughput. *Nature Methods*, 14:395, 2017.

[127] E. Z. Macosko, A. Basu, R. Satija, J. Nemesh, K. Shekhar, M. Goldman, I. Tirosh, A. R. Bialas, N. Kamitaki, E. M. Martersteck, J. J. Trombetta, D. A. Weitz, J. R. Sanes, A. K. Shalek, A. Regev, and S. A. McCarroll. Highly parallel genome-wide expression profiling of individual cells using nanoliter droplets. *Cell*, 161(5):1202–1214, 2015.

[128] B. Treutlein, Q. Y. Lee, J. G. Camp, M. Mall, W. Koh, S. A. M. Shariati, S. Sim, N. F. Neff, J. M. Skotheim, M. Wernig, and S. R. Quake. Dissecting direct reprogramming from fibroblast to neuron using single-cell RNA-seq. *Nature*, 534(7607):391–395, 2016.

[129] K. Lee, Y. Cui, L. P. Lee, and J. Irudayaraj. Quantitative imaging of single mRNA splice variants in living cells. *Nature Nanotechnology*, 9(6):474–480, 2014.

[130] J. P. Giraldo-Vela, W. Kang, R. L. McNaughton, X. M. Zhang, B. M. Wile, A. Tsourkas, G. Bao, and H. D. Espinosa. Single-cell detection of mRNA expression using nanofountain-probe electroporated molecular beacons. *Small*, 11(20):2386–2391, 2015.

[131] W. B. Frommer, M. W. Davidson, and R. E. Campbell. Genetically encoded biosensors based on engineered fluorescent proteins. *Chemical Society Reviews*, 38(10):2833–2841, 2009.

[132] D. Jimenez de Aberasturi, A. B. Serrano-Montes, J. Langer, M. Henriksen-Lacey, W. J. Parak, and L. M. Liz-Marzán. Surface enhanced Raman scattering encoded gold nanostars for multiplexed cell discrimination. *Chemistry of Materials*, 28(18):6779–6790, 2016.

[133] K. H. Chen, A. N. Boettiger, J. R. Moffitt, S. Wang, and X. Zhuang. Spatially resolved, highly multiplexed RNA profiling in single cells. *Science*, 348(6233), 2015.

[134] Q. Han, N. Bagheri, E. M. Bradshaw, D. A. Hafler, D. A. Lauffenburger, and J. C. Love. Polyfunctional responses by human T cells result from sequential release of cytokines. *Proceedings of the National Academy of Sciences of the United States of America*, 109(5):1607–1612, 2012.

[135] J. J. Niu, M. G. Schrlau, G. Friedman, and Y. Gogotsi. Carbon nanotube-tipped endoscope for in situ intracellular surface-enhanced Raman spectroscopy. *Small*, 7(4):540–545, 2011.

[136] O. Guillaume-Gentil, R. V. Grindberg, R. Kooger, L. Dorwling-Carter, V. Martinez, D. Ossola, M. Pilhofer, T. Zambelli, and J. A. Vorholt. Tunable single-cell extraction for molecular analyses. *Cell*, 166(2):506–516, 2016.

[137] P. Actis, M. M. Maalouf, H. J. Kim, A. Lohith, B. Vilozny, R. A. Seger, and N. Pourmand. Compartmental genomics in living cells revealed by single-cell nanobiopsy. *ACS Nano*, 8(1):546–553, 2014.

[138] T. Geng and C. Lu. Microfluidic electroporation for cellular analysis and delivery. *Lab on a Chip*, 13(19):3803–3821, 2013.

[139] L. Chang, L.and Li, J. Shi, Y. Sheng, W. Lu, D. Gallego-Perez, and L. J. Lee. Micro-/nanoscale electroporation. *Lab on a Chip*, 16(21):4047–4062, 2016.

[140] W. Kang, F. Yavari, M. Minary-Jolandan, J. P. Giraldo-Vela, A. Safi, R. L. McNaughton, V. Parpoil, and H. D. Espinosa. Nanofountain probe electroporation (NFP-E) of single cells. *Nano Letters*, 13(6):2448–2457, 2013.

[141] R. Yang, V. Lemaître, C. Huang, A. Haddadi, R. L. McNaughton, and H. D. Espinosa. Monoclonal cell line generation and CRISPR/Cas9 manipulation via single-cell electroporation. *Small*, 14(12):1702495, 2018.

[142] Y. Zhan, C. Sun, Z. Cao, N. Bao, J. Xing, and C. Lu. Release of intracellular proteins by electroporation with preserved cell viability. *Analytical chemistry*, 84(19):8102–5, 2012.

[143] Y. Cao, M. Hjort, H. Chen, F. Birey, S. A. Leal-Ortiz, C. M. Han, J. G. Santiago, S. P. Paşca, J. C. Wu, and N. A. Melosh. Nondestructive nanostraw intracellular sampling for longitudinal cell monitoring. *Proceedings of the National Academy of Sciences*, 114(10):E1866–E1874, 2017.

[144] W. Kang, J. P. Giraldo-Vela, S. S. P. Nathamgari, T. McGuire, R. L. McNaughton, J. A. Kessler, and H. D. Espinosa. Microfluidic device for stem cell differentiation and localized electroporation of postmitotic neurons. *Lab on a Chip*, 14(23):4486–4495, 2014.

[145] M. P. Rols and J. Teissie. Electropermeabilization of mammalian cells. quantitative analysis of the phenomenon. *Biophysical journal*, 58(5):1089–1098, 1990.

[146] M. P. Rols and J. Teissie. Electropermeabilization of mammalian cells to macromolecules: control by pulse duration. *Biophysical journal*, 75(3):1415–1423, 1998.

[147] M. Golzio, J. Teissié, and M. P. Rols. Direct visualization at the single-cell level of electrically mediated gene delivery. *Proceedings of the National Academy of Sciences*, 99(3):1292–1297, 2002.

[148] J. C. Weaver and Y. A. Chizmadzhev. Theory of electroporation: A review. *Bioelectrochemistry and Bioenergetics*, 41(2):135–160, 1996.

[149] W. K. Neu and J. C. Neu. *Theory of Electroporation*, pages 133–161. Springer US, Boston, MA, 2009.

[150] K. T. Powell and J. C. Weaver. Transient aqueous pores in bilayer membranes: a statistical theory. *Bioelectrochemistry and Bioenergetics*, 15(2):211–227, 1986.

[151] R. S. Son, T. R. Gowrishankar, K. C. Smith, and J. C. Weaver. Modeling a conventional electroporation pulse train: Decreased pore number, cumulative calcium transport and an example of electrosensitization. *IEEE Transactions on Biomedical Engineering*, 63(3):571–580, 2016.

[152] J. M. Escoffre, T. Portet, L. Wasungu, J. Teissié, D. Dean, and M. P. Rols. What is (still not) known of the mechanism by which electroporation mediates gene transfer and expression in cells and tissues. *Molecular Biotechnology*, 41(3):286–295, 2009.

[153] A. Azan, F. Gailliègue, L. M. Mir, and M. Breton. *Cell Membrane Electropulsation: Chemical Analysis of Cell Membrane Modifications and Associated Transport Mechanisms*, pages 59–71. Springer International Publishing, Cham, 2017.

[154] D. C. Chang and T. S. Reese. Changes in membrane structure induced by electroporation as revealed by rapid-freezing electron microscopy. *Biophysical Journal*, 58(1):1–12, 1990.

[155] J. T. Sengel and M. I. Wallace. Imaging the dynamics of individual electropores. *Proceedings of the National Academy of Sciences*, 113(19):5281–5286, 2016.

[156] Mounir Tarek. *Atomistic Simulations of Electroporation of Model Cell Membranes*, pages 1–15. Springer International Publishing, Cham, 2017.

[157] M. Hibino, H. Itoh, and K. Kinosita Jr. Time courses of cell electroporation as revealed by submicrosecond imaging of transmembrane potential. *Biophysical journal*, 64(6):1789–1800, 1993.

[158] K. Kinosita Jr, I. Ashikawa, N. Saita, H. Yoshimura, H. Itoh, K. Nagayama, and A. Ikegami. Electroporation of cell membrane visualized under a pulsed-laser fluorescence microscope. *Biophysical journal*, 53(6):1015–1019, 1988.

[159] M. Wang, O. Orwar, J. Olofsson, and S. G. Weber. Single-cell electroporation. *Analytical and bioanalytical chemistry*, 397(8):3235–48, 2010.

[160] C. Barrau, J. Teissie, and B. Gabriel. Osmotically induced membrane tension facilitates the triggering of living cell electropermeabilization. *Bioelectrochemistry*, 63(1-2):327–332, 2004.

[161] D. Needham and R. M. Hochmuth. Electro-mechanical permeabilization of lipid vesicles. role of membrane tension and compressibility. *Biophysical journal*, 55(5):1001–1009, 1989.

[162] X. Han, Z. Liu, M. chan Jo, K. Zhang, Y. Li, Z. Zeng, N. Li, Y. Zu, and L. Qin. CRISPR-Cas9 delivery to hard-to-transfect cells via membrane deformation. *Science Advances*, 1(7):e1500454, 2015.

[163] X. Ding, M. P. Stewart, A. Sharei, J. C. Weaver, R. S. Langer, and K. F. Jensen. High-throughput nuclear delivery and rapid expression of DNA via mechanical and electrical cell-membrane disruption. *Nature Biomedical Engineering*, 1(3):0039, 2017.

[164] S. Pierre and P. Julie. Membrane tension and cytoskeleton organization in cell motility. *Journal of Physics: Condensed Matter*, 27(27):273103, 2015.

[165] Y. Huang and B. Rubinsky. Microfabricated electroporation chip for single cell membrane permeabilization. *Sensors and Actuators A: Physical*, 89(3):242–249, 2001.

[166] X. Xie, A. M. Xu, S. Leal-Ortiz, C. C. Cao, Y.and Garner, and N. A. Melosh. Nanostraw-electroporation system for highly efficient intracellular delivery and transfection. *ACS nano*, 7(5):4351–8, 2013.

[167] H. Wolf, M. P. Rols, E. Boldt, E. Neumann, and J. Teissié. Control by pulse parameters of electric field-mediated gene transfer in mammalian cells. *Biophysical Journal*, 66(2):524–531, 1994.

[168] M. Golzio, M. P. Mora, C. Raynaud, C. Delteil, J. Teissié, and M. P. Rols. Control by osmotic pressure of voltage-induced permeabilization and gene transfer in mammalian cells. *Biophysical Journal*, 74(6):3015–3022, 1998.

[169] Z. Jiang, W. Li, D. W. Apley, and W. Chen. A spatial-random-process based multidisciplinary system uncertainty propagation approach with model uncertainty. *Journal of Mechanical Design*, 137(10):101402–101402–13, 2015.

[170] A. Tanay and A. Regev. Scaling single-cell genomics from phenomenology to mechanism. *Nature*, 541:331, 2017.

[171] C. Weinreb, S. Wolock, B. K. Tusi, M. Socolovsky, and A. M. Klein. Fundamental limits on dynamic inference from single-cell snapshots. *Proceedings of the National Academy of Sciences*, 115(10):E2467–E2476, 2018.

[172] A. McKenna, G. M. Findlay, J. A. Gagnon, M. S. Horwitz, A. F. Schier, and J. Shendure. Whole-organism lineage tracing by combinatorial and cumulative genome editing. *Science*, 353(6298), 2016.

[173] D. E. Wagner, C. Weinreb, Z. M. Collins, J. A. Briggs, S. G. Megason, and A. M. Klein. Single-cell mapping of gene expression landscapes and lineage in the zebrafish embryo. *Science*, 2018.

[174] R. P. Joshi and K. H. Schoenbach. Electroporation dynamics in biological cells subjected to ultrafast electrical pulses: A numerical simulation study. *Physical Review E*, 62(1):1025–1033, 2000.

[175] K. A. DeBruin and W. Krassowska. Modeling electroporation in a single cell. I. effects of field strength and rest potential. *Biophysical Journal*, 77(3):1213–1224, 1999.

[176] A. M. Xu, A. Aalipour, S. Leal-Ortiz, A. H. Mekhdjian, X. Xie, A. R. Dunn, C. C. Garner, and N. A. Melosh. Quantification of nanowire penetration into living cells. *Nature Communications*, 5:3613, 2014.

[177] K. Liu, Q. Yan, M. Chen, W. Fan, Y. Sun, J. Suh, D. Fu, S. Lee, J. Zhou, S. Tongay, et al. Elastic properties of chemical-vapor-deposited monolayer MoS_2, WS_2, and their bilayer heterostructures. *Nano Letters*, 14(9):5097–5103, 2014.

[178] J. C. Neu and W. Krassowska. Asymptotic model of electroporation. *Physical Review E*, 59(3):3471–3482, 1999.

[179] V. F. Pastushenko, Y. A Chizmadzhev, and V. B. Arakelyan. Electric breakdown of bilayer lipid membranes: II. Calculation of the membrane lifetime in the steady-state diffusion approximation. *Journal of Electroanalytical Chemistry and Interfacial Electrochemistry*, 104:53–62, 1979.

[180] J. C. Neu, K. C. Smith, and W. Krassowska. Electrical energy required to form large conducting pores. *Bioelectrochemistry*, 60(1):107–114, 2003.

[181] Z. Vasilkoski, A. T. Esser, T. R. Gowrishankar, and J. C. Weaver. Membrane electroporation: The absolute rate equation and nanosecond time scale pore creation. *Physical Review E*, 74(2):021904, 2006.

[182] E. M. Renkin. Filtration, diffusion, and molecular sieving through porous cellulose membranes. *The Journal of General Physiology*, 38(2):225–243, 1954.

[183] P. M. Bungay and H. Brenner. The motion of a closely-fitting sphere in a fluid-filled tube. *International Journal of Multiphase Flow*, 1(1):25–56, 1973.

[184] A. Parsegian. Energy of an ion crossing a low dielectric membrane: Solutions to four relevant electrostatic problems. *Nature*, 221:844, 1969.

[185] L. V. Chernomordik, S. I. Sukharev, S. V. Popov, V. F. Pastushenko, A. V. Sokirko, I. G. Abidor, and Y. A. Chizmadzhev. The electrical breakdown of cell and lipid membranes: the similarity of phenomenologies. *Biochimica et Biophysica Acta (BBA) - Biomembranes*, 902(3):360–373, 1987.

[186] O. Sten-Knudsen. *Biological Membranes: Theory of Transport, Potentials and Electric Impulses*. Cambridge University Press, 2002.

APPENDIX A

Supporting Information for Chapter 2

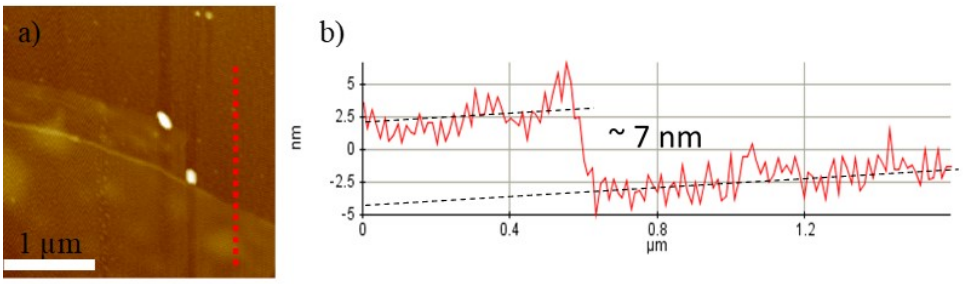

Figure A.1. a) AFM topography image of the 9-layered WS_2 resonator. b) Height profile along the dotted line shown in the topography image a).

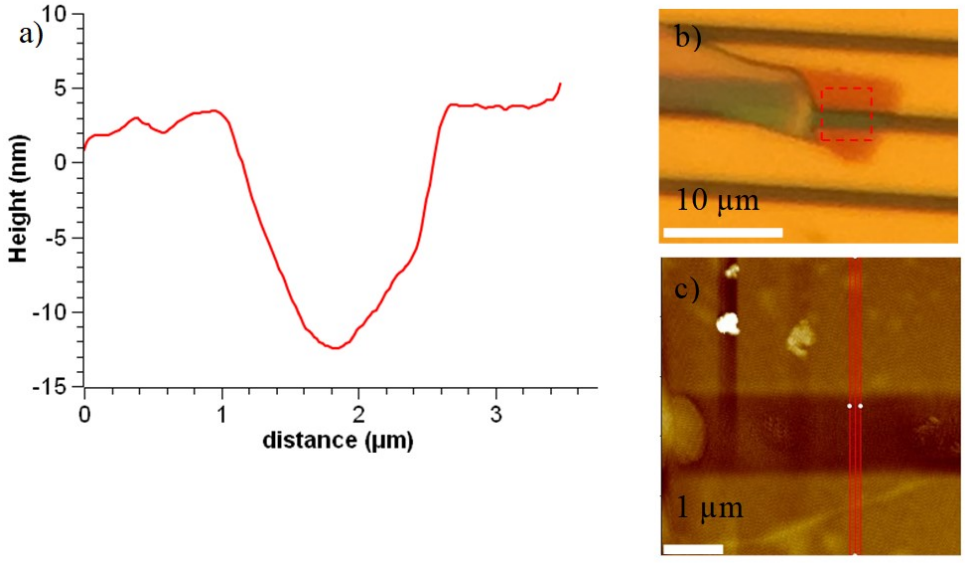

Figure A.2. a) Height profile of the suspended region of the resonator highlighted in the topography image shown in c). The AFM topography image was obtained on the dotted region shown in the optical micrograph in b).

APPENDIX B

Supporting Information for Chapter 3

B.1. Device Fabrication

A schematic of the fabrication methodology is shown in Figure B.1. Atomically thin WS_2 flakes were first mechanically exfoliated onto a Si/SiO_2 substrate from a bulk-crystal (2D Semiconductors) using the widely reported scotch-tape method. A thin layer of polymethyl methacrylate (PMMA) was then spin-coated onto the flakes. The flake/PMMA stack was released using KOH wet-etching and transferred to a hydrogen silsesquioxane (HSQ) coated Si/SiO_2 wafer. The HSQ/PMMA bilayer was patterned using e-beam lithography to define the clamping electrodes, followed by Au-deposition using e-beam evaporation and lift-off. The unexposed HSQ underneath the flake was removed using a developer, followed by critical point drying to release the flake.

B.2. Responsivity of the interferometer

In our fabrication methodology, the thickness of the spin-coated HSQ layer determines the cavity depth. Based on the thin-film interference model discussed in Chapter 2.2.4, we chose a value of 375 nm that yielded a responsivity of $3\text{x}10^{-3}$/nm (data point shown as a circle in Figure B.2).

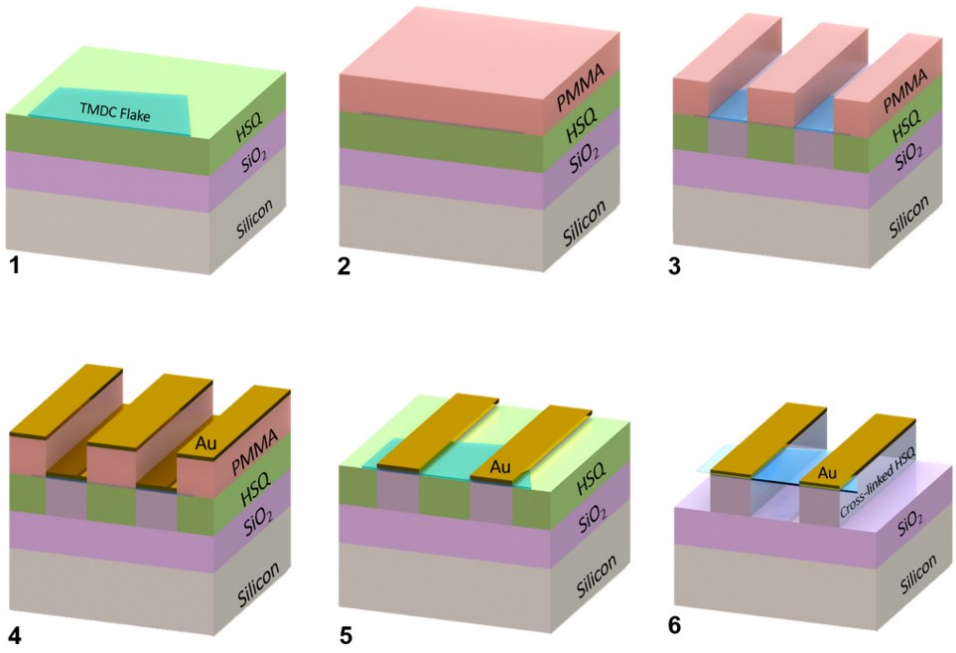

Figure B.1. Schematic of the fabrication methodology. Mechanically exfoliated flakes from a bulk-crystal were transferred to a Si substrate coated with HSQ using KOH wet-etching (step 1) and PMMA transfer (step 2). The PMMA, HSQ stack was then patterned using e-beam lithography to define the clamping regions (step 3), followed by Au-deposition (step 4), lift-off (step 5) and critical point drying (step 6).

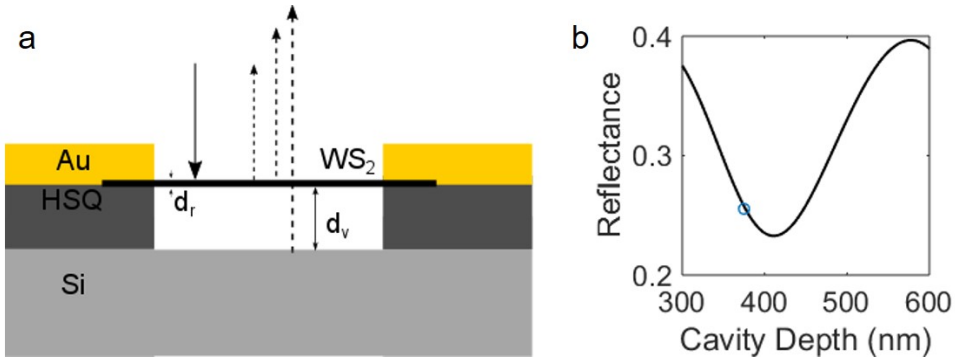

Figure B.2. A) Schematic of the thin-film interference model used to calculate the cavity's reflectance. Solid arrows indicate incident beam, dotted lines indicate reflected beams. B) Plot showing the reflectance of the cavity for various depth values. A cavity depth of 375 nm yields a responsivity of (-) $3\text{x}10^{-3}$/nm.

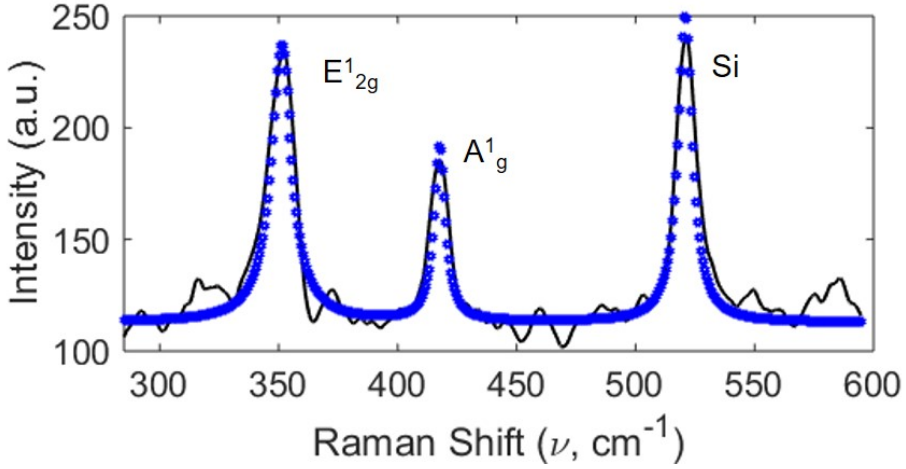

Figure B.3. Raman spectroscopy measurements confirm the nanoresonator to be monolayer thick. The measured data points (black, solid line) were fit to a multi-peak, Lorentzian line-shape to extract the peak locations of the E^1_{2g}, A^1_g and Si phonon modes

B.3. Raman Spectroscopy

A He-Ne laser (632.8 nm peak wavelength) was used as the excitation source. The laser power was kept to < 450 μW to minimize sample heating. The laser was focused on the sample to a spot size of < 2 μm. The reflected light from the nanoresonator was filtered using a Rayleigh filter (efficient to <150 cm^{-1}), dispersed using a spectrograph (1800 grooves/mm) and measured on a Peltier-cooled detector, with a spectral resolution of < 1 cm^{-1}. The peak locations were identified by fitting the measured data to a multi-peak, Lorentzian line-shape, as shown in Figure B.3. The peak location of Si (520.7 cm^{-1}) was used to account for any drift in the spectrograph. The peak locations of the E^1_{2g}, A^1_g phonon modes were 351 cm^{-1}and 417.5 cm^{-1} respectively. A spacing of 66.5 cm^{-1} between the two modes confirmed that it was monolayer thick [62].

B.4. Mode-shapes obtained using modal analysis and estimation of critical buckling load

We used ABAQUS to perform modal analysis, both with and without the inclusion of prestress. For the former case, the plate was prestressed by inducing an in-plane displacement (of different magnitudes) along one of the fixed boundaries, while the value of the membrane load was extracted from the opposite boundary as reaction forces. The nodal forces were averaged against the boundary length to determine the membrane load. Shell elements (S4R) were employed to model the nanoresonator as a thin, flat plate. The exact geometry as obtained from an SEM image was used in the calculations. 200 elements were used in the analysis after performing a convergence study. The different material parameters used in the analysis are listed in Table B.1.

Table B.1. List of material parameters used in modal analysis

Parameter	Value used
Young's modulus (E_Y [177])	270 GPa
Poisson's Ratio (ν)	0.3
Density (ρ)	7500 kg m^{-3}
Thickness [89]	0.34 nm

We evaluated the critical buckling load in the following manner. The buckling eigenmodes were first extracted using linear analysis in ABAQUS (Abaqus 6.14 Online Documentation). Nonlinear buckling analysis was then performed by adding an imperfection to the plate in the form of the first buckling eigenmode. By varying the peak amplitude of the imperfection from -0.1 to 0.1 nm, the load (N_{xx}) vs out of plane displacement w_m curve was computed (see Figure B.5a). Here, (w_m) refers to the out of plane displacement of the plate's centroid. As the imperfection was made asymptotically smaller, the

equilibrium curve approached the bifurcation point, which allowed the estimation of the critical buckling load. By imposing a prestress of $\sigma_0 = 45$ μN/m, the predicted frequency for the fundamental mode matched the measured value of 1.04 MHz. In Figure B.5b, the measured resonance spectrum (driving voltage 1.5V_{p-p} for modes 1-6 and 2.0V_{p-p} for modes 7-8) is presented along with the predicted values for modes 1-4 (shown as vertical dashed lines). The discrepancy between the predicted and observed frequencies may be due to an inhomogeneous strain, imperfections and floppy/edge modes due to free-edge boundary conditions [94, 95, 100].

B.5. Accounting for spurious resonances from PZT disc

In order to eliminate spurious resonances that originate from the PZT disc, we measured the reflectance from the gold electrodes (blue dot in the SEM image in Figure B.6's inset) as the driving frequency was varied. Unlike cavity-interferometric measurements on the sample, here, changes in the power of the reflected light due to the motion of the gold electrodes were measured. If r is the the reflectance coefficient of Au and m is the modulation coefficient of the incident beam with power P_i, then the photodetector measures a time-averaged power given by $P_{det} = P_i r^2 m^2$. The modulation coefficient has a frequency dependence and has local maxima at the resonance frequencies of the PZT disc. In Figure B.6, the red curve displays the resonance spectrum from the WS_2 resonator for an actuation drive of 3V_{p-p} measured using cavity-interferometry; whereas the blue curve is the reflectance measurement on the gold electrode. Spurious resonances due to the motion of the PZT appear as common peaks in both spectra and are indicated by arrows. The reflectance measurement has additional peaks (circled in Figure B.6), which do not

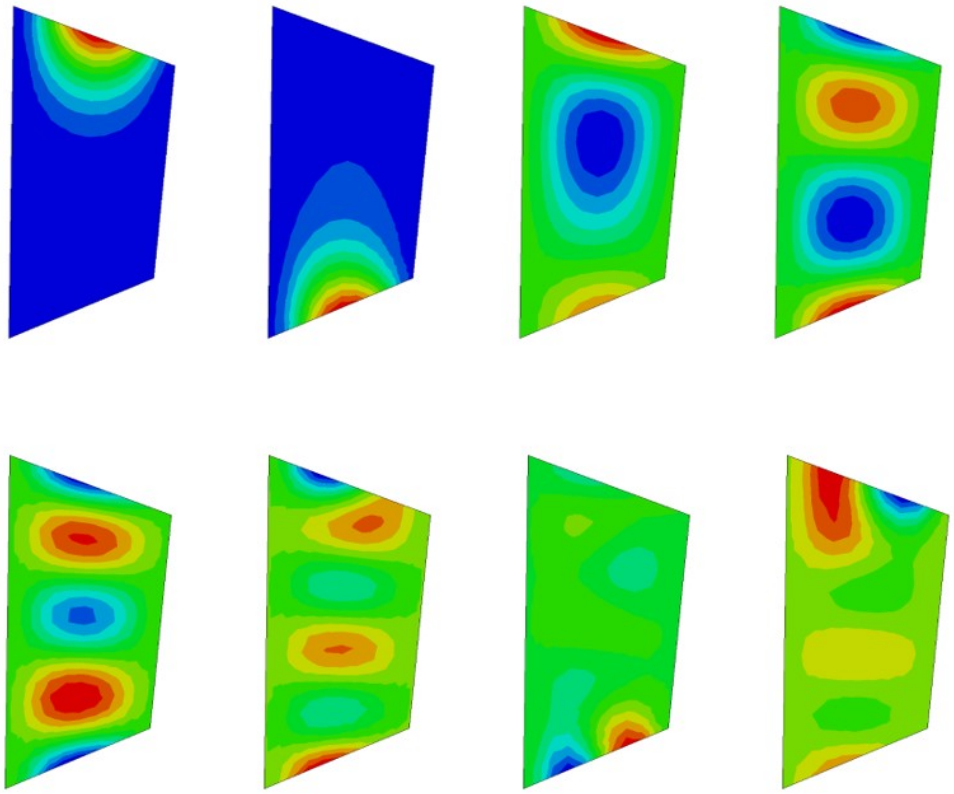

Figure B.4. Mode-shapes of the WS_2 nanoresonator obtained from the modal analysis. The top row shows modes 1-4 (from left to right), whereas the bottom row shows modes 5-8 (from left to right). In the color bar, red and blue correspond to opposite directions of motion in the out of plane direction.

appear in the interferometric measurements, presumably because both the PZT and the nanoresonator are in phase and get displaced by approximately the same distance.

B.6. Weakly nonlinear behavior in modes 1, 2

The measured frequency response data for mode 1 are fit to a Duffing model with additional higher order nonlinear terms to account for the mixed behavior as given in 3.1. The nonlinear terms effectively modify the resonance frequency ω_e and damping γ_e. As shown in ref. [99], the fits are performed by expressing ω_e, γ_e as polynomial functions

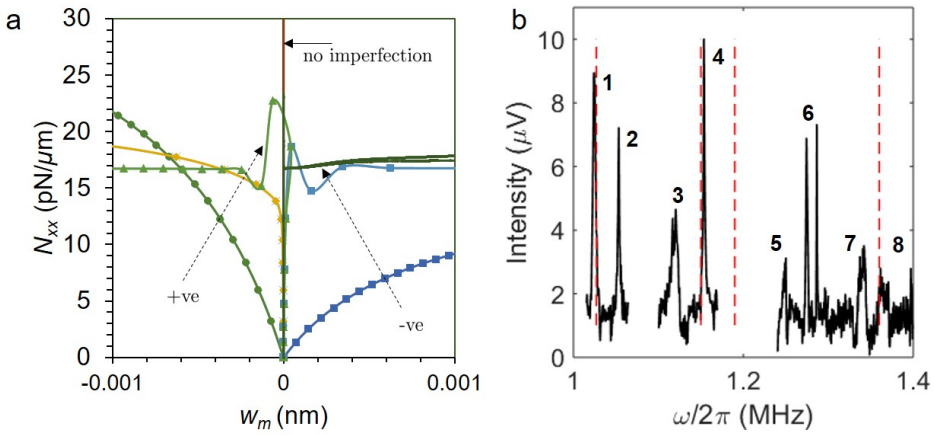

Figure B.5. Membrane load N_{xx} as a function of the out of plane displacement of the plate's centroid w_m for various positive (+ve) and negative (-ve) imperfection amplitudes. The value of N_{xx} corresponding to the smallest, non-zero imperfection is taken as the buckling load. The arrows point in the direction of decreasing imperfection amplitude. The ideal (no imperfection) curve is shown in red. b) The measured resonance spectrum of the WS_2 nanoresonator is compared with the predicted frequencies (vertical dashed lines) from modal analysis using a prestress value $\sigma_0 = 45$ μN/m. Modes 1-6 were acquired with a driving voltage of $1.5V_{p-p}$ whereas modes 7-8 were acquired with $2V_{p-p}$ actuation voltage for a better signal to noise ratio.

of the peak-amplitude x_0, i.e. $\omega_e = \omega_0^2 + A_1 x_0^2 + A_2 x_0^3 + A_3 x_0^4$ and $\gamma_e = \gamma + B_1 x_0^2$. The measured frequency response data for mode 2 is fit to a standard Lorentzian line-shape.

B.7. Bifurcation analysis on mode 7

We employed units of μV for the displacement to directly compare with the experimental data. The units of the linearized frequencies ω_i and damping μ_i remain unchanged; the units for the nonlinear coefficients k_i and Λ_i were adjusted accordingly (see Table B.2). The value of the cubic nonlinear coefficient k_2 was estimated from the data corresponding to the softening portion of mode 8 (Figure B.8a). The same value was used for k_1. The value of Λ was iteratively varied until the predicted frequency response matched with the

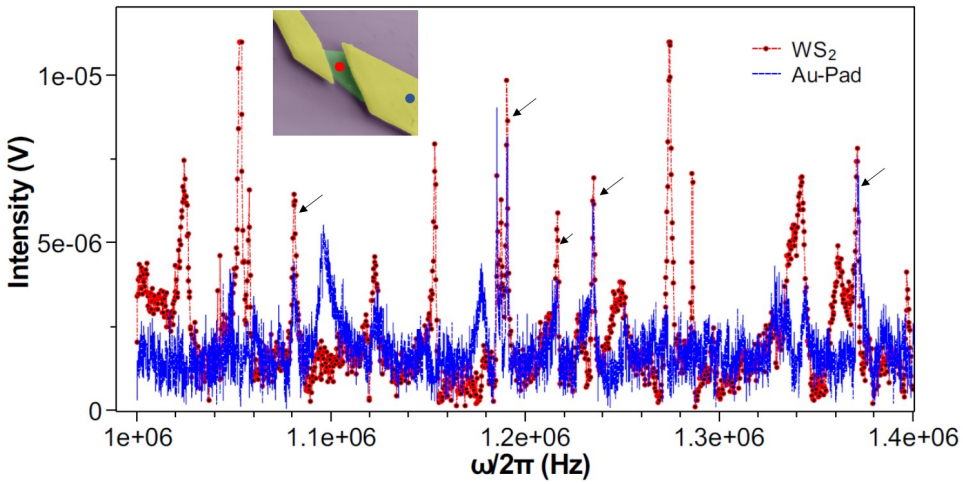

Figure B.6. Measurements are made both on the WS_2 nanoresonator (red curve) and the PZT disc (blue curve) to eliminate any parasitic resonances from the latter. Such resonances appear as common peaks in both measurements and are indicated here by arrows. Inset shows an SEM image in which the red dot is the region where the WS_2 resonance spectrum was recorded, while the blue dot corresponds to the region where PZT motion was measured

measured data for an actuation voltage of $3V_{p-p}$. Then, the value of Λ was fixed at -1e^{-1} s^{-2}/ μV^2 and the force term F was varied to match with the measured data for different applied voltages. The actuation force on the nanoresonator results from inertial coupling with the motion of the PZT disc. For a harmonic base excitation $d = d_0 \sin \omega t$ of the PZT, the inertial force acting on the resonator is given by $F = T m_r \omega^2 d_0$, where m_r is the mass of the nanoresonator and T is the transmission coefficient. The peak displacement d_0 varies linearly with the applied voltage and hence, $F \propto V$. Figure B.8b shows a scatter plot with those values of F that resulted in the best fit for the measured data at different actuation voltages used in the experiments. The expected linear relation between F, V is reproduced. The bifurcation set for the two Hopf points shown in Figure 3.5d in the main text predicts that for force values < 5 s^{-2}/ μV, the Hopf points disappear. This

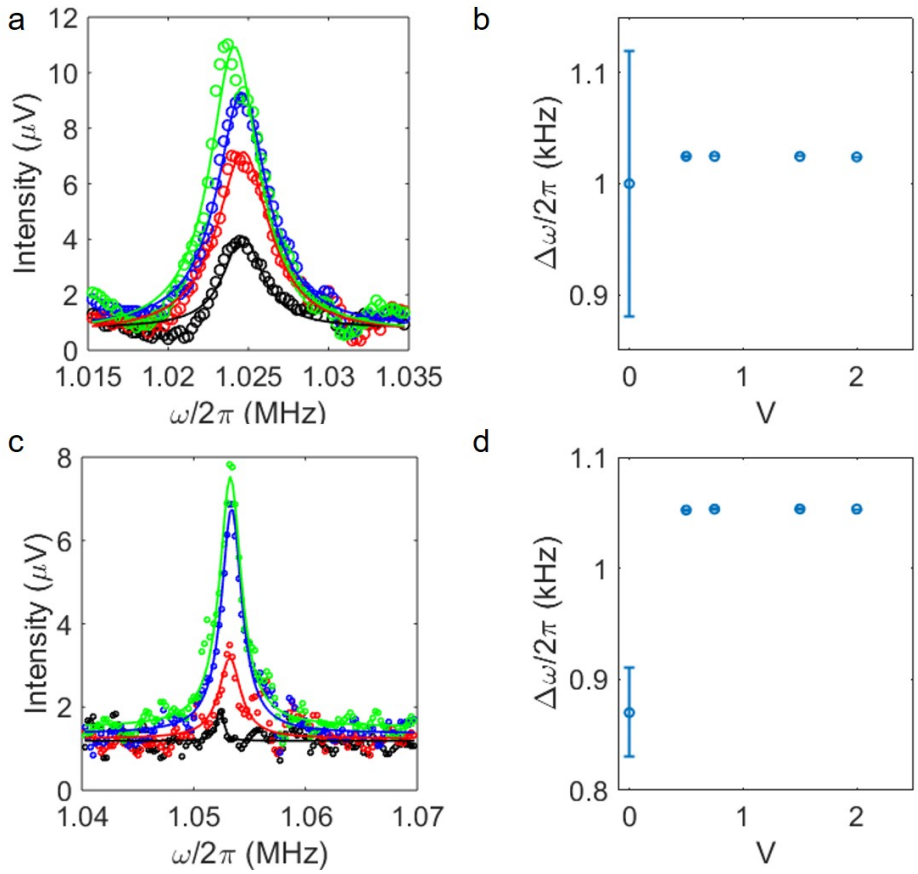

Figure B.7. The measured data for modes 1, 2 (shown as circles in a, c) are fit to the line-shapes described in the text. The fits are shown using solid lines. From bottom to top, the drive voltages are 0.5, 0.75, 1.5 and $2V_{p-p}$. The extracted linewidth for different actuation voltages are plotted in subfigure b for mode 1 and d for mode 2. The case corresponding to zero voltage is the thermo-mechanical resonance. The error bars for the driven resonances are within the data points.

corresponds to an actuation voltage of $1.5V_{p-p}$, as estimated from the linear fit in Figure B.8b.

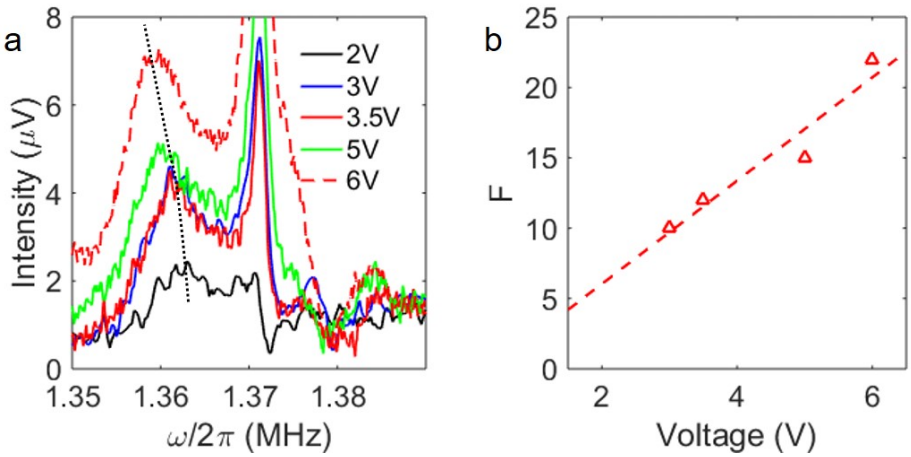

Figure B.8. a) The softening portion in the measured data of mode 8 (indicated by the dotted lines) was used to estimate the cubic nonlinear term k_2. b) Drive force F values that reproduced the measured frequency response curves for mode 7 at various actuation voltages are shown along with a linear fit (dashed line).

Table B.2. Values of different parameters used in the bifurcation analysis

Parameter	Value used, units
ω_1, ω_2	2π × (1.34, 1.36) MHz
$\mu_1 = \mu_2 = \mu$	0.32 MHz
k_1, k_2	-2e^{-3} s^{-2}/ μV^2
Λ	-1e^{-1} s^{-2}/ μV^2
F	(10, 12, 15, 22) s^{-2}/ μV

APPENDIX C

Supporting Information for Chapter 4

C.1. Coupling between Electric Field and Pore Evolution Equations

The formation of electro-pores leads to a change in the conductivity of the cell membrane. This is incorporated in the model by modifying the cell membrane resistances R_t and R_b at every time step based on the distribution of electro-pores obtained from the Smoluchowski equation. The total cell membrane resistance is given by C.1 where, R is the total membrane resistance ($d_m/\kappa A$) where d_m is the thickness of the cell membrane, κ is the effective cell membrane conductivity and A is the total area of the cell membrane. In our case R is R_t or R_b. R_m is the resistance of the cell membrane and R_p is the resistance of one electro-pore. The summation is over all the electro-pores present at a particular time.

$$\frac{1}{R} = \frac{1}{R_m} + \sum \frac{1}{R_p} \tag{C.1}$$

We have $R_m = R_m^{'}/((1-A_f))$; where $R_m^{'}$ is the resistance of the intact cell membrane without electro-pores and A_f is the area fraction of the membrane covered by electro-pores present at a particular time step. For our model $R_m^{'} = d_m/\kappa^{'} A$ and $A_f = \int_{r_{min}}^{r_{max}} n\pi r_p^2 dr_p$ where $\kappa^{'}$ is the conductivity of the intact cell membrane. The overall resistance of an

electro-pore is given by $R_p = d_m/(2\kappa_p A_p H_p K_p) + 1/(2\kappa_p r_p)$ where κ_p is the pore conductivity, A_p is the area of the pore and H_p and K_p are the hindrance and partition factors respectively [151].

Table C.1. Different parameters used in the lumped model given by equations 4.1-4.3

W	$R_g/R_g + R_{cy}$
X	$WR_{cy} + R_{cp} + R_{op}$
Y	$R_s + R_{op}\,(1 - R_{op}/Y)$
Z	$1 - R_{cy}/(R_g + R_{cy})$
n_1	$1/(YC_c)$
n_2	$-C_c^{-1}\,(1/R_c + 1/Z)$
n_3	$-WR_{op}/(XYC_c)$
n_4	$ZR_{op}/(XYC_t)$
n_5	$C_t^{-1}\left(1/R_t + (ZWR_{op}^2/X^2Y) + WZ/X + 1/(R_g + R_{cy})\right)$
n_6	$C_t^{-1}\left((ZWR_{op}^2/X^2Y) + WZ/X + 1/(R_g + R_{cy})\right)$
n_7	$ZR_{op}/(XYC_b)$
n_8	$C_b^{-1}\left((ZWR_{op}^2/X^2Y) + WZ/X + 1/(R_g + R_{cy})\right)$
n_9	$C_b^{-1}\left(1/R_b + (ZWR_{op}^2/X^2Y) + WZ/X + 1/(R_g + R_{cy})\right)$

C.2. Hydrophilic Pore Energy and Tension Coupled Pores

The energy difference (E) between an intact lipid bilayer membrane and one with a hydrophilic electro-pore as a function of the radius of the pore (r_p) is given by equation C.2, where the first term arises due to the steric repulsion between lipid heads with representing the steric repulsion energy [178]. The second term is due to the line tension along the pore perimeter where γ is the edge energy [179]. The third term accounts for the reduction of membrane tension and consequently the energy due to the formed pore with σ_e being the effective membrane tension [149]. The final term which takes the form of work done by an electric field on a dielectric body is the contribution of the TMP (V_m) in reducing the energy [180]. The non-linear form of the effective membrane tension

(σ_e) which couples the electro-pores is given by equation C.3 (ref. [149]), where $\sigma^{'}$ is the energy of the hydrocarbon-water interface, σ is the surface tension of the membrane without pores and A_f is the area fraction of pores as discussed before. The function $F(r, V_m)$, which represents the electric force is given by C.4(see ref. [180])

$$E(r_p) = \beta \left(\frac{r_{min}}{r_p}\right)^4 + 2\pi\gamma r_p - \sigma_e \pi r_p^2 - \int_{r_{min}}^{r_{max}} F(r^{'}, V_m) dr^{'} \tag{C.2}$$

$$\sigma_e = 2\sigma^{'} - \frac{2\sigma^{'} - \sigma}{(1 - A_f)^2} \tag{C.3}$$

$$F(r, V_m) = \frac{F_{max}}{1 + r_h/(r + r_t)} V_m^2 \tag{C.4}$$

C.3. Pore Creation and Destruction Rates

The Smoluchowski equation is solved in the pore radius space to obtain the pore distribution at every time step. At the minimum radius (r_m), an Arrhenius-type expression (see equation C.5) is used as the boundary condition to account for the nucleation and destruction of electro-pores [181], where A is the pore creation rate density, B is the pore creation constant and ν is the pore destruction constant derived by assuming an absorption condition slightly below r_{min} [1]. At the maximum radius (r_{max}), a no flux boundary condition given by equation C.6 is used.

$$-\left(D_p\frac{\partial n}{\partial r_p}+\frac{D_p}{kT}n\frac{\partial E}{\partial r_p}\right) = Ae^{BV_m^2/kT}-\nu n \tag{C.5}$$

$$D_p\frac{\partial n}{\partial r_p}+\frac{D_p}{kT}n\frac{\partial E}{\partial r_p} = 0 \tag{C.6}$$

C.4. Hindrance and Partition

Due to the finite size and charge of a molecule, their transport through a pore in a dielectric media is impeded as compared to the bulk electrolyte. The hindrance and partition factors are introduced to account for the impeded transport. A spherical molecule of finite size is obstructed due to the decreased effective area of pore available for transport and drag from the pore walls [182, 183]. The hindrance factor $H_p = f_A f_D$ is a continuum approximation that accounts for these effects, where f_A, f_D are the area and drag factors respectively. These factors are given in equations C.7-C.8, where $\lambda = r_s/r_p$ and the constants a_1 to a_7 are tabulated in Table

$$f_A = \left(1-\frac{r_s}{r_p}\right)^2 \tag{C.7}$$

$$f_D = 6\pi/f_t \tag{C.8}$$

$$f_t = \frac{9}{4}\pi^2\sqrt{2}(1-\lambda)^{-5/2}\left(1+a_1(1-\lambda)+a_2(1-\lambda)^2\right)+ a_3+a_4\lambda+a_5\lambda^2+a_6\lambda^3+a_7\lambda^4 \tag{C.9}$$

The partition factor accounts for the non-ohmic behavior of a pore formed in a membrane that affects the transport of charged specie across it. The electrostatic interaction

of a charged molecule with the pore wall leads to higher energy of the molecule inside the low dielectric membrane pore as compared to the bulk electrolyte, as shown by Parsegian [184]. Thus, there is an energy barrier hindering the transport of charged molecules into the membrane pores, which increases with decreasing pore size. Assuming a trapezoidal energy profile inside a membrane pore, Chernomordik et. al [185] developed the following expression for the partition function (K_p)

$$K_p = \frac{e^{\Delta\psi_m} - 1}{\frac{w_0 e^{w_0 - n_r\Delta\psi_m - n_r\Delta\psi_m}}{w_0 - n_r\Delta\psi_m} e^{\Delta\psi_m} - \frac{w_0 e^{w_0 + n_r\Delta\psi_m + n_r\Delta\psi_m}}{w_0 + n_r\Delta\psi_m}} \tag{C.10}$$

In equation C.10, n_r is the relative entrance length of the pore and $\Delta\psi_m = (ez/kT)V_m$ is the normalized TMP (e is the electronic charge, z is the valency of the molecule of interest and V_m is the transmembrane potential). Further, w_0 is the Born Energy [181, 184] which in this context is the energy required to place a unit charge from the bulk medium into the dielectric membrane pore, i.e. $w_0 = 5.3643\frac{(ez)^2}{kT} r_p^{-1.803}$.

C.5. Verification of Multiphysics Model

The Boltzmann distribution satisfies the steady state Smoluchowski equation [186]. In order to verify the model, the normalized pore distribution $n/\sum n$ at steady state, obtained from the numerical simulation, was compared to the analytical Boltzmann distribution $e^{(-E/kT)}\Big/\sum e^{(-E/kT)}$ where, E is the hydrophilic pore energy calculated using equation C.2. We found close agreement between the two solutions (Supplementary Figure C.1). The pore distribution (n) obtained from the numerical simulation was also plotted for different mesh sizes and the solutions were found to converge (Supplementary

Table C.2. Parameters used in Pore Evolution Equation

$\kappa^{'}$, Membrane conductivity	5×10^{-7} S/m
κ_p, Pore conductivity	1 S/m
d_m, cell membrane thickness	5 nm
r_{min}, Minimum electro-pore radius	0.65 nm
r_{max}, Maximum electro-pore radius	15 nm
β, Steric repulsion energy	1.4×10^{-19} J
γ, Edge energy	2×10^{-11} J/m
σ, Initial membrane tension	0.1 to 8×10^{-4} N/m
$\sigma^{'}$, Hydrocarbon-water interface tension	2×10^{-2} J/m
F_{max}, Maximum electric force	6.9×10^{-10} N/V^2
r_h, Electric force constant	0.95 nm
r_t, Electric force constant	0.23 nm
D_p, Pore diffusion coefficient	2×10^{-13} m^2/s
A, Pore creation rate density	1×10^{9} m^2/s
B , Pore creation constant	20 kT/V^2
T, Temperature	310 K
D, Diffusion coefficient of molecule	3×10^{-11} m^2/s

Table C.3. Parameters used in Transport Equation

PARAMETER	VALUE
r_s, Radius of molecule	3 nm
a_1	-1.2167
a_2	1.5336
a_3	-22.5083
a_4	-5.6117
a_5	-0.3363
a_6	-1.216
a_7	1.647
n_r, Relative entrance length	0.25

Figure C.1). The mesh element size was fixed at 0.05 nm, which ensured that the Peclet Number is <1 and no numerical instability is encountered while solving the Smoluchowski equation.

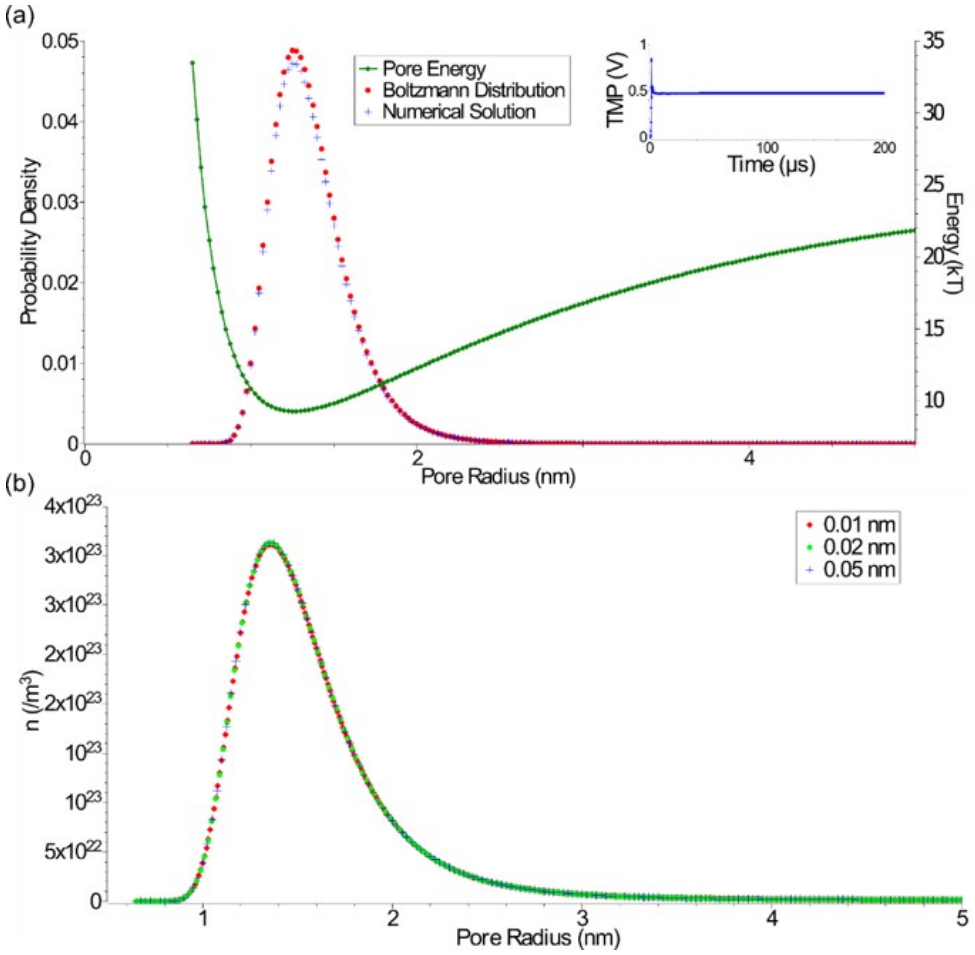

Figure C.1. Model Verification (a) The normalized steady state pore distribution $n/\sum n$ obtained from the numerical simulation (200 μs into the pulse) is plotted as a function of pore radius and compared to the analytical Boltzmann distribution ($e^{(-E/kT)}/\sum e^{(-E/kT)}$) where, E is the hydrophilic pore energy (Eq. C.2). Inset shows that the TMP has reached a steady state at 200 μs. The steady state solution of the Smoluchowski equation is the Boltzmann distribution, and the analysis serves as a verification for the model, (b) The pore distribution (n) at 50 μs is plotted as a function of pore radius for different mesh sizes. The solution does not change with mesh size. The applied far-field voltage is 15 V for both the cases

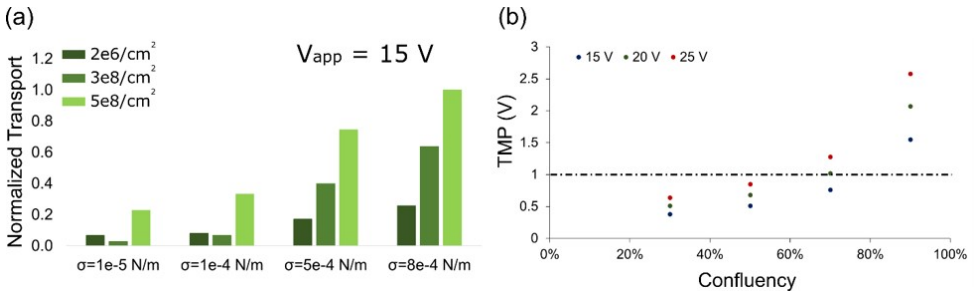

Figure C.2. Effect of nanochannel density and cell confluency (a) The normalized transport is plotted for polycarbonate substrates with different nanochannel densities for varying membrane tensions. The transport is found to increase with increasing nanochannel density. The applied voltage is 15 V, (b) The TMP obtained from the equivalent circuit model without pore evolution is plotted as a function of cell confluency for different applied voltages. It is found that the confluency should be above 80% for the TMP to exceed the critical value of 1 V. The nanochannel density used in these calculations is 5e8/cm^2

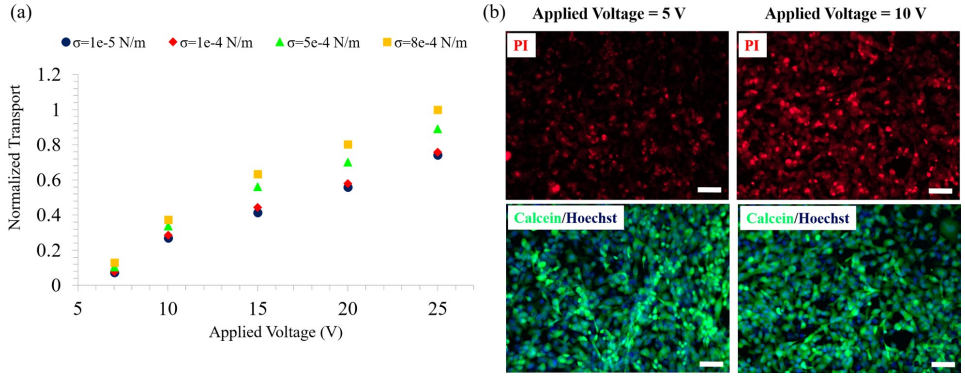

Figure C.3. Transport of Small Molecules (a) The normalized transport obtained from the simulations is plotted against the applied far-field voltage (V_app) for different values of membrane tension (σ). The transport of small molecules increases linearly with V_app and shows lower sensitivity with increasing σas compared to that of large molecules, (b) PI is delivered into HT 1080 cells under iso-osmolar conditions. Top fluorescence images show the delivery of PI at two different applied voltages (5 V and 10 V). The fluorescence intensity is enhanced with an increase in V_app from 5 V to 10 V indicating increased transport. Bottom fluorescence images indicates the corresponding cell viability (>95%) after 6 hours using live dead staining.

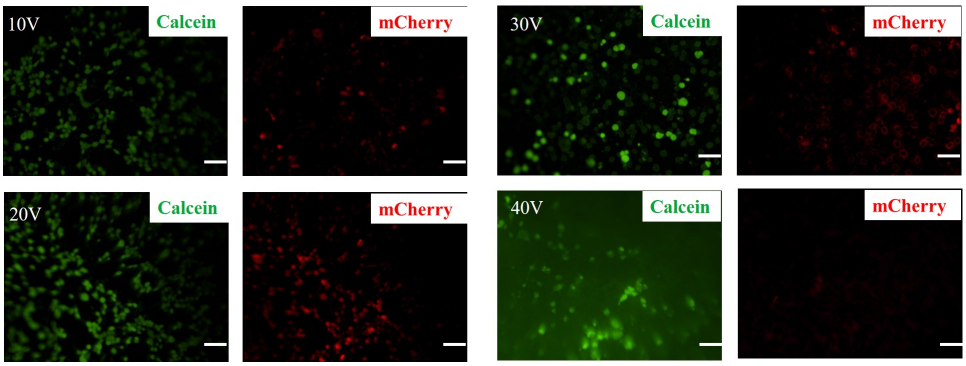

Figure C.4. The transfection efficiency of mCherry plasmid (1 day after electroporation) and cell-viability in HT 1080 cells were investigated under various voltage amplitudes. The cell-viability and transfection efficiency were optimal for 30 V. Scale bars = 50 μm in all images.

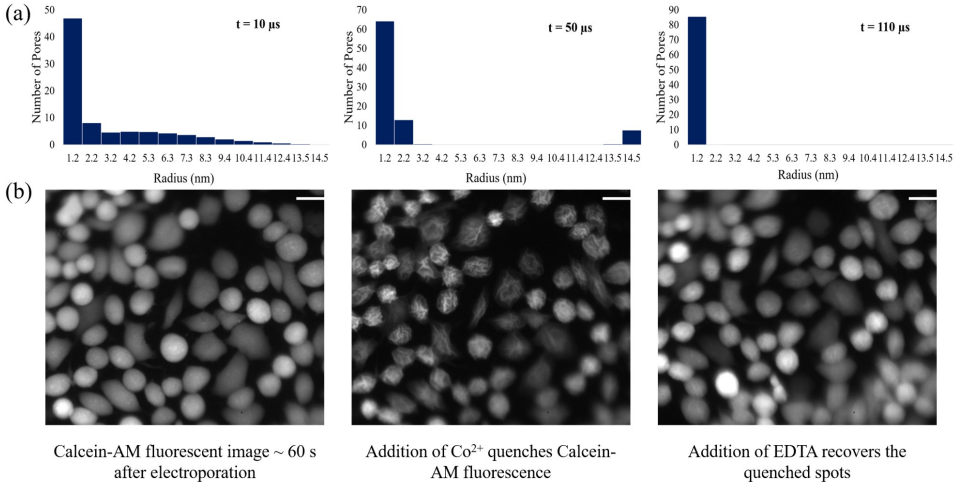

Figure C.5. Existence of small pores post pulsation (a) Histogram of pore sizes for a 10 V pulse of 100 μs duration at 1e-5 N/m membrane tension. Large pore ($>$ 3 nm) populations exist during the pulse (Left and Middle). Only a population of small pores ($<$ 1.5 nm) remain after the pulse (Right), (b) Co^{2+} is introduced into electroporated CHO cells approximately 1 minute after the pulse ends. The addition of Co^{2+} results in a quenching of the green fluorescence signal, which is later recovered ($\approx$ 3 mins) by introducing a chelating buffer (EDTA). The quenching and subsequent recovery indicate that small pores remain open even after the pulse has ended. Scale bars = 30 μm

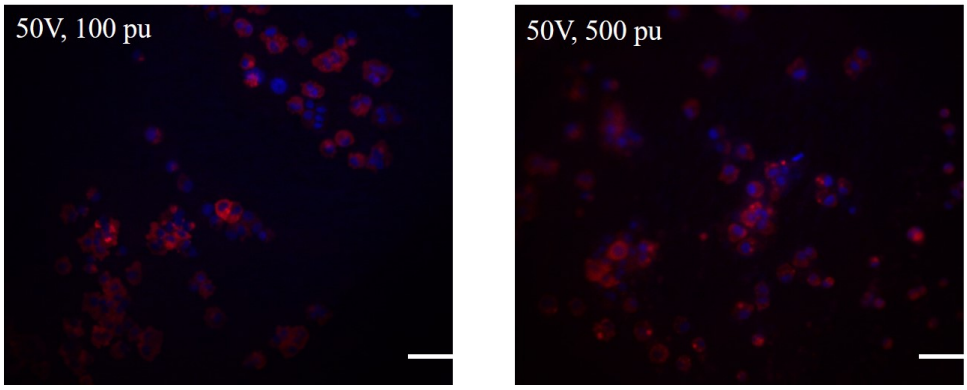

Figure C.6. At higher voltage amplitudes (50 V for the images shown here), most cells lifted on day 1. Further, the cell morphology looked abnormal. The composite images show tdTomato expression (red) and cell-nuclei (blue). Scale bars = 100 μm.

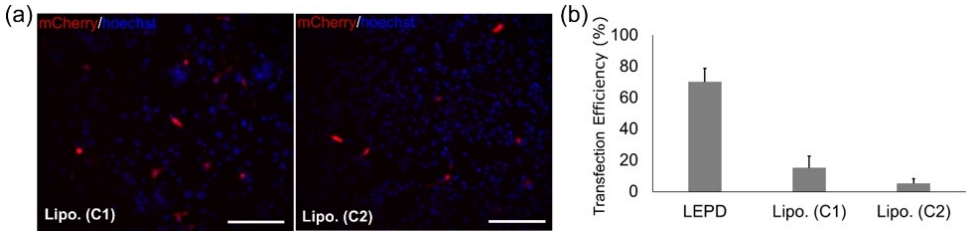

Figure C.7. Comparison of LEPD with Lipofectamine Transfection (a) Transfection of mCherry plasmid in MDA-MB 231 cells using lipofectamine under two conditions. Left: Transfection using 0.3 μl of lipofectamine per 100 ng of DNA (C1). Right: Transfection using 0.15 μl of lipofectamine per 100 ng of DNA (C2). Scale Bars = 400 μm, (b) Comparison of transfection efficiencies for the LEPD (using 30 V pulse and hypo-osmolar buffer) and lipofectamine. $N = 3$ for all cases

Vita

Samba Shiva Prasad, Nathamgari was born and raised in southern India. He received a Bachelor of Technology degree in Civil Engineering from the Indian Institute of Technology (IIT), Guwahati in 2010. As an undergraduate student, he worked on research projects in the fields of Applied Mathematics (adaptive grids in singular perturbation problems), Inverse Problems in Engineering (leakage detection in pipe networks using inverse transient analysis), and Computational Mechanics (comparative study of locking-free shear-flexible beam in mesh-free methods). During 2010-12, he worked as Project Engineer with Indian Oil Corporation Ltd. in a 1000 km pipeline project. At Indian Oil, he designed and executed quality control (QC) plans related to construction of civil health monitoring units, pipe milling and coating. He joined Prof. Espinosa's group at Northwestern University in Fall 2012 to pursue a Ph.D. in Theoretical and Applied Mechanics. His research contributions have resulted in the following publications[1]:

(1) S. Shiva P. Nathamgari, Siyan Dong, Lior Medina, Nicolaie Moldovan, Daniel Rosenmann, Ralu Divan, Daniel Lopez, Lincoln J. Lauhon, and Horacio D. Espinosa. "*A Force Sensor Based on Nonlinear Mode Coupling in a Monolayer WS_2 Nanoresonator*." Submitted to PNAS.

[1] * denotes equal contribution

(2) Siyan Dong*, S. Shiva P. Nathamgari*, Nicolaie Moldovan, Daniel Rosenmann, Ralu Divan, and Horacio D. Espinosa. "*Non-contact Measurement of Piezoelectricity in Free-standing, Transition Metal Dichalcogenides*." Manuscript in preparation.

(3) S. Shiva P. Nathamgari, Vincent Lemaitre, Nibir Pathak, Chian-Yu Peng, Tammy McGuire, John A. Kessler and Horacio D. Espinosa. "*Nanofountain Probe Electroporation (NFP-E): A versatile localized electroporation system for intracellular delivery and sampling in a variety of adherent cell lines*." Manuscript in preparation.

(4) Prithvijit Mukherjee*, S. Shiva P. Nathamgari*, John A. Kessler, and Horacio D. Espinosa. "*Combined Numerical and Experimental Investigation of Localized Electroporation-Based Cell Transfection and Sampling*." ACS Nano 12, no. 12 (2018): 12118-12128.

(5) S. Shiva P. Nathamgari*, Siyan Dong*, Ehsan Hosseinian, Lincoln J. Lauhon, and Horacio D. Espinosa. "*An Experimental Setup for Combined In-Vacuo Raman Spectroscopy and Cavity-Interferometry Measurements on TMDC Nanoresonators*." Experimental Mechanics (2018): 1-11.

(6) S. Shiva P. Nathamgari, Biqin Dong, Fan Zhou, Wonmo Kang, Juan P. Giraldo-Vela, Tammy McGuire, Rebecca L. McNaughton, Cheng Sun, John A. Kessler, and Horacio D. Espinosa. "*Isolating single cells in a neurosphere assay using inertial microfluidics*." Lab on a chip 15, no. 24 (2015): 4591-4597.

(7) Broussard, Joshua A., Ruiguo Yang, Changjin Huang, S. Shiva P. Nathamgari, Allison M. Beese, Lisa M. Godsel, Marihan H. Hegazy et al. "*The desmoplakin–intermediate filament linkage regulates cell mechanics*." Molecular biology of the cell 28, no. 23 (2017): 3156-3164.

(8) Kang, Wonmo, Juan P. Giraldo-Vela, S. Shiva P. Nathamgari, Tammy McGuire, Rebecca L. McNaughton, John A. Kessler, and Horacio D. Espinosa. "*Microfluidic device for stem cell differentiation and localized electroporation of postmitotic neurons*." Lab on a Chip 14, no. 23 (2014): 4486-4495.

(9) Beese, Allison M., Zhi An, Sourangsu Sarkar, S. Shiva P. Nathamgari, Horacio D. Espinosa, and SonBinh T. Nguyen. "*Defect-Tolerant Nanocomposites through Bio-Inspired Stiffness Modulation*." Advanced Functional Materials 24, no. 19 (2014): 2883-2891.